



UNIVERSITY OF LEEDS

This is a repository copy of *A review on selective laser sintering/melting (SLS/SLM) of aluminium alloy powders: Processing, microstructure, and properties*.

White Rose Research Online URL for this paper:  
<http://eprints.whiterose.ac.uk/90338/>

Version: Accepted Version

---

**Article:**

Olakanmi, EO, Cochrane, RF and Dalgarno, KW (2015) A review on selective laser sintering/melting (SLS/SLM) of aluminium alloy powders: Processing, microstructure, and properties. *Progress in Materials Science*, 74. 401 - 477. ISSN 0079-6425

<https://doi.org/10.1016/j.pmatsci.2015.03.002>

---

© 2015, Elsevier. Licensed under the Creative Commons Attribution-NonCommercial-NoDerivatives 4.0 International  
<http://creativecommons.org/licenses/by-nc-nd/4.0/>

**Reuse**

Unless indicated otherwise, fulltext items are protected by copyright with all rights reserved. The copyright exception in section 29 of the Copyright, Designs and Patents Act 1988 allows the making of a single copy solely for the purpose of non-commercial research or private study within the limits of fair dealing. The publisher or other rights-holder may allow further reproduction and re-use of this version - refer to the White Rose Research Online record for this item. Where records identify the publisher as the copyright holder, users can verify any specific terms of use on the publisher's website.

**Takedown**

If you consider content in White Rose Research Online to be in breach of UK law, please notify us by emailing [eprints@whiterose.ac.uk](mailto:eprints@whiterose.ac.uk) including the URL of the record and the reason for the withdrawal request.



[eprints@whiterose.ac.uk](mailto:eprints@whiterose.ac.uk)  
<https://eprints.whiterose.ac.uk/>

**Number of manuscript folios: One hundred and ninety-two (192) pages.**

**Number of figures: Sixty-two (62).**

**Number of tables: Ten (10).**

**Short running title: A review on selective laser sintering/melting (SLS/SLM) of aluminium alloy powders: Processing, microstructure, and properties.**

**Name of the corresponding author: Dr. Eyitayo Olatunde Olakanmi**

**Full mailing address: 58A, Second Avenue, Westdene, Johannesburg 2092, South Africa.**

**(e.o.olakanmi@gmail.com) (+27(0)710389307).**

**A review on selective laser sintering/melting (SLS/SLM) of aluminium alloy powders:  
Processing, microstructure, and properties**

**E. O. Olakanmi<sup>a, b</sup>; R. F. Cochrane<sup>a</sup>; K. W. Dalgarno<sup>c</sup>**

**<sup>a</sup>Institute for Materials Research, University of Leeds, United Kingdom.**

**<sup>b</sup>Department of Mechanical Engineering, Federal University of Technology, Minna. Niger  
State. Nigeria.**

**<sup>c</sup>School of Mechanical and Systems Engineering, Newcastle University, Newcastle upon  
Tyne, United Kingdom.**

**A review on selective laser sintering/melting (SLS/SLM) of aluminium alloy powders:  
Processing, microstructure, and properties**

**Abstract**

Manufacturing businesses aiming to deliver their new customised products more quickly and gain more consumer markets for their products will increasingly employ selective laser sintering/melting (SLS/SLM) for fabricating high quality, low cost, repeatable, and reliable aluminium alloy powdered parts for automotive, aerospace, and aircraft applications. However, aluminium powder is known to be uniquely bedevilled with the tenacious surface oxide film which is difficult to avoid during SLS/SLM processing. The tenacity of the surface oxide film inhibits metallurgical bonding across the layers during SLS/SLM processing and this consequently leads to initiation of spheroidisation by Marangoni convection. Due to the paucity of publications on SLS/SLM processing of aluminium alloy powders, we review the current state of research and progress from different perspectives of the SLS/SLM, powder metallurgy (P/M) sintering, and pulsed electric current sintering (PECS) of ferrous, non-ferrous alloys, and composite powders as well as laser welding of aluminium alloys in order to provide a basis for follow-on- research that leads to the development of high productivity, SLS/SLM processing of aluminium alloy powders. Moreover, both P/M sintering and PECS of aluminium alloys are evaluated and related to the SLS process with a view to gaining useful insights especially in the aspects of liquid phase sintering (LPS) of aluminium alloys; application of LPS to SLS process; alloying effect in disrupting the surface oxide film of aluminium alloys; and designing of aluminium alloy suitable for the SLS/SLM process. Thereafter, SLS/SLM parameters, powder

properties, and different types of lasers with their effects on the processing and densification of aluminium alloys are considered. The microstructure and metallurgical defects associated with SLS/SLM processed parts are also elucidated by highlighting the mechanism of their formation, the main influencing factors, and the remedial measures. Mechanical properties such as hardness, tensile, and fatigue strength of SLS/SLM processed parts are reported. The final part of this paper summarises findings from this review and outlines the trend for future research in the SLS/SLM processing of aluminium alloy powders.

**Keywords:** Selective laser sintering/melting (SLS/SLM); Liquid phase sintering (LPS); Spheroidisation; Powder Metallurgy (P/M); Microstructural evolution, Mechanical properties.

## **Outline**

1. Introduction
2. Variants of SLS/SLM Processing of Aluminium Alloys
3. Relevance of Powder Metallurgy, and Pulsed Electric Current Sintering (PECS) to SLS Process of Aluminium Alloys
  - 3.1 Powder Metallurgy (P/M) Liquid Phase Sintering (LPS)
  - 3.2 Application of Liquid Phase Sintering (LPS) to SLS Process
  - 3.3 Oxide Disruption in Pulsed Electric Current Sintering (PECS) Processed Aluminium Alloy Powders

### 3.4 Alloy Design for SLS Process

## 4. Effects of Processing Parameters and Powder Properties on the SLS/SLM Processing and Densification of Powders

### ➤ 4.1 SLS/SLM Processing Windows of Aluminium Alloy Powders

### ➤ 4.2 Effects of SLS/SLM and Powder Parameters on the Densification Mechanism

#### 4.2.1 Scan Line Spacing, Scanning Speed, Laser Power, Layer Thickness, and Energy Density on Densification

#### 4.2.2 Effects of Scanning Strategy on the Densification Mechanism

#### 4.2.3 Effects of SLS/SLM Atmospheres on the Densification Mechanism

### 4.3 Effects of Powder Properties on the Densification of Mechanism

#### 4.3.1 Effect of Particle Size and Distribution on the Densification Mechanism

#### 4.3.2 Effect of Particle Shape on the Densification Mechanism

#### 4.2.3 Effect of Alloying Addition and Oxidic Constitution on the Densification Mechanism

### 4.4 Effects of Laser Types on the Processing and Densification of Metal Powders

## 5. Microstructure and Metallurgical Defects in SLS/SLM Fabricated Parts

### 5.1 Microstructure of SLS/SLM Fabricated Parts

#### 5.1.1 Epitaxial Solidification and SLM

5.1.2 Effects of Processing Conditions on the Microstructure of SLS/SLM Fabricated Parts

5.1.3 Effects of Powder Properties on the Microstructure of SLS/SLM Processed Components

5.1.3.1 Effect of Particle Size on the Microstructure of SLS Processed Components

5.1.3.2 Effect of Alloying on the Microstructure of SLS Fabricated Components

5.2 Metallurgical Defects in SLS/SLM Processed Aluminium Alloy Parts

5.2.1 Porosity

5.2.2 Cracking

5.2.3 Oxide Inclusions

5.2.4 Loss of Alloying Elements

6. Mechanical Properties of SLS/SLM Fabricated Parts

6.1 Hardness and Wear Resistance

6.2 Tensile Strength

6.3 Fatigue Strength

7. Perspectives on SLS/SLM Processing of Aluminium Alloy Powders

8. Future Research Interests

9. Conclusions

Acknowledgements

## References

## **1. Introduction**

Aluminium (Al) alloys; the second most used metal surpassed only by steel; are categorised into heat treatable, non-heat treatable and casting alloys [1-4]. Commercial heat treatable Al alloys are 2000 (Al-Cu or Al-Cu-Mg), 6000 (Al-Mg-Si), and 7000 (Al-Zn-Mg) series alloys whose strength and other properties are enhanced by various heat treatment processes whereas non-heat-treatable Al alloys include 1000, 3000, 4000 containing only Si, and 5000 series alloys which are strengthened by mechanical deformation processes [1-4]. They are increasingly employed in automotive, aerospace, and aircraft applications because of their recyclability, excellent strength-to-weight ratio, thermal and electrical conductivity, corrosion resistance, formability, and attractive appearance.

Engineering parts made in aluminium alloys have been fabricated by traditional manufacturing processes such as casting, forging, extrusion, and powder metallurgy (P/M). However, these traditional manufacturing processes have resulted in parts having coarse grain structures with the attendant poor mechanical properties as a consequence of low cooling rates associated with these processes [5, 6]. Moreover, the adoption of tooling for making Al alloy parts through these traditional manufacturing routes increases the cost of production and the lead time. Therefore, for manufacturing businesses engaging in the fabrication of aluminium parts and aiming to deliver their new customised products more quickly and gain more consumer markets for their products, selective laser sintering/melting (SLS/SLM) has become a promising manufacturing route for such businesses. This is because SLS/SLM, a layer manufacturing (LM) technique, allows parts to be fabricated without any part-specific tools being required; shortens

the design and production cycle; and promises to revolutionise the traditional manufacturing processes by engendering significant time and cost savings [7, 8].

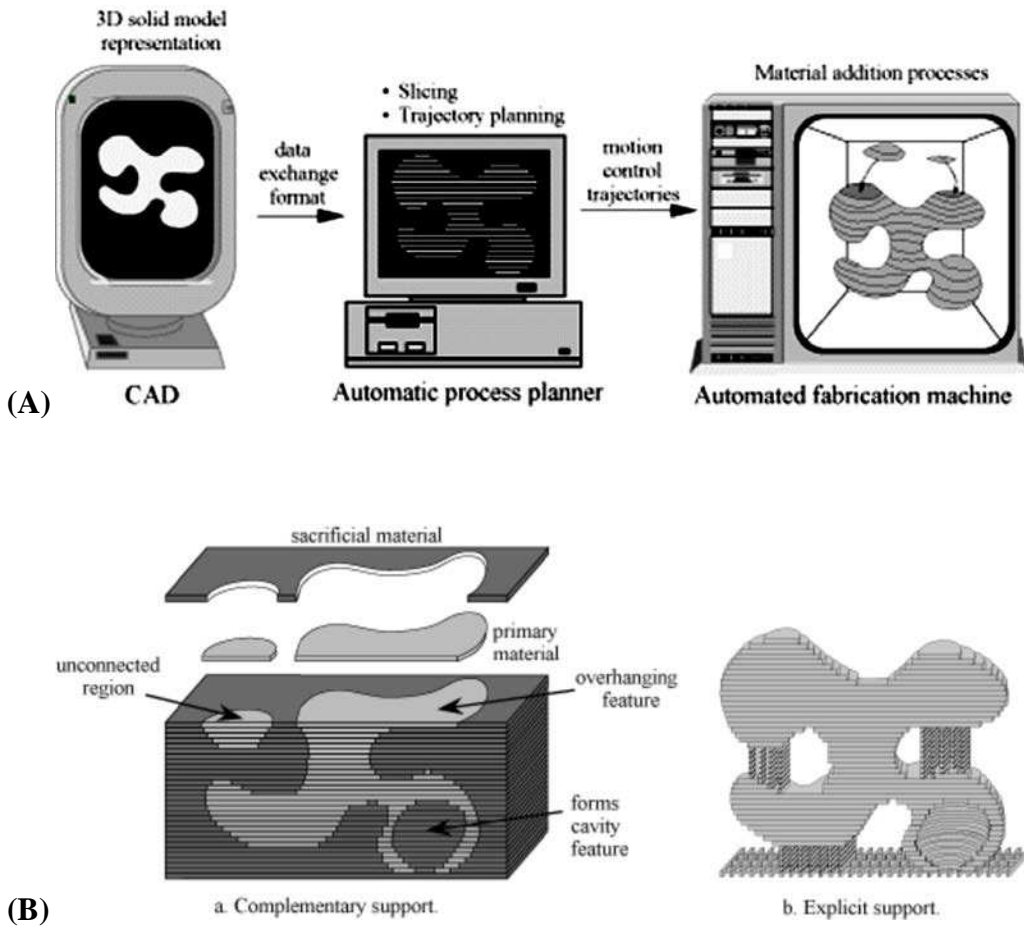


**Fig. 1.** (A) A layered manufacturing (LM) paradigm (B) Generic fixturing [9].

SLS/SLM creates 3-D parts through the application of laser energy to powder beds via the 3-D CAD description of the part geometry from which it derives a 2-D stack of layers which represent the part (Fig. 1A). Each layer is then created by scanning a laser spot over the required cross-sectional area, and using the laser to melt, sinter and bond particles together in a thin

lamina. By spreading a further layer of powder on top of the previously processed layer and repeating the scanning process; subsequent layers are created and simultaneously bonded to already existing layers until such time as the entire stack of 2-D layers has been created and bonded together to form the geometry described by the original 3-D CAD solid model (Fig. 1B). Functional graded materials [10], rapid tooling [6, 11] and satellite technology [12] have been identified as promising areas for the application of SLS/SLM; Calignano et al. [13] fabricated mechanisms for machine and robotic designs via SLS; Das and co-investigators [14, 15] demonstrated the feasibility of fabricating components for defence applications by the selective laser sintering/hot isostatic pressing (SLS/HIP) technique; Stoodley et al. [11], Hayashi et al. [17], Hollander et al. [18], Kanazawa et al. [19] and Wauthle et al. [20] employed SLS/SLM to process implants for medical purposes while Vasquez et al. [21] recently developed new SLS materials for snowboarding applications. Ardila et al. [22] and Seyda et al. [23] also highlighted another important advantage of SLS/SLM in that it allows an efficient use of the material, due to the possibility to recycle and reuse un-melted metal powder. They established that after recycling powders between 12 to 14 times, there were no significant changes in powder and test parts properties (Fig. 2), hence, validating powder recycling methodology for its use in SLS/SLM manufacturing. Other outstanding ecological performing indicators of SLS/SLM process include reduction in emissions because fewer raw materials need to be produced, design for light-weight structuring with a weight reduction and design for performance and indirect usage of toxic chemicals like lubricant or coolant in any measurable amount [24, 25].

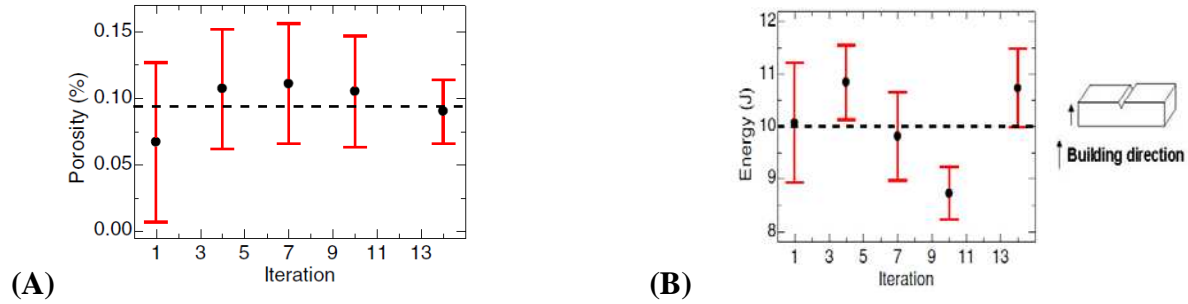


**Fig. 2.** Results from (A) porosity and (B) Charpy impact measurements performed over manufactured samples. Each point represents the average % porosity or impact energy determined for six samples fabricated in five particular iterations. Red bars indicate standard deviation from the average values of porosity and impact energy. The dashed line represents an average porosity or impact energy obtained from these five values [22].

With the expected rapid development and improvement in process capabilities of SLS/SLM in the next decade, these examples buttress the fact that SLS/SLM remains the technology of the future as human lives continue to depend upon the quality and ease of use of its products in the manufacturing, transportation, medicine, sports and electronics sectors.

However, the main drawbacks of SLS/SLM techniques are poor surface quality, and dimensional accuracy, as well as material properties (microstructure and mechanical strength) that do not meet the pre-requisite for industrial applications. To address these demerits, post-processing treatments like polishing, painting, heat-treatment, and furnace-infiltration e.t.c. have been employed [26]. Again, these post-processing treatments also introduce the burden of elongating the production cycle and increasing the cost of production. Meanwhile, investigation of appropriate process and material parameters required for obtaining improved surface finish,

dimensional accuracy, and mechanical strength of SLS/SLM fabricated parts is also being undertaken with a view to eliminating these post-processing steps in order to shorten the lead time and reduce production costs.

Recently, SLS/SLM processing of aluminium alloy powders and their composites [24, 27-43, 45] has been undertaken with a view to gaining an understanding of laser processability. Furthermore, in similarity to laser welding of aluminium alloys, the effectiveness of SLS/SLM processing had been found to be a function of physical properties (Table 1) such as low absorptivity to the laser beam, tenacious oxide films, low boiling point elements, high thermal conductivity, high co-efficient of thermal expansion, relatively wide solidification temperature ranges, high solidification shrinkage, a tendency to form low melting constituents, low viscosity, and high solubility of hydrogen in liquid state [4, 30, 31, 32, 44, 45]. Meanwhile, in similarity to other metallic powders, SLS/SLM of aluminium alloy powders can be bedevilled with complications such as balling, porosity, layer distortion, cracking, poor dimensional accuracy and surface roughness, and loss of alloying elements [45]. These complications occur because of the oxide contamination; development of non-uniform thermal gradients across the processed parts; Marangoni convection which inhibits successful melt pool to substrate bonding in SLM or inter-particulate bonding in SLS across the layers; and high power density employed for SLS/SLM processing [8, 45-47]. It had also been established that these difficulties result in components with undesirable microstructures giving rise to poor physical and mechanical properties.

**Table 1**

Properties of pure and alloyed aluminium at its melting point [44]

Properties (Unit)	Pure Al
Ionisation energy (Ev)	6
Specific heat (J/kg/K)	1080
Specific heat of fusion (J/kg)	$4 \times 10^5$
Melting point (K)	933
Boiling point (K)	2603
Viscosity (kg/m/s)	0.0013
Surface tension (N/m)	0.84
Thermal conductivity (W/m/K)	94.03
Thermal diffusivity ( $M^2/s$ )	$3.65 \times 10^{-5}$
Expansion co-efficient (1/K)	$24 \times 10^{-6}$
Density ( $kg/m^3$ )	2385
Elastic modulus ( $N/m^3$ )	$7.1 \times 10^{10}$

The focus of this review is to understand the variants of SLS/SLM process, as applicable to aluminium alloys, in order to establish the science base of SLS/SLM process for their reliable fabrication of parts. Available literature on conventional powder metallurgy (P/M) sintering, and pulsed electric current sintering (PECS) of aluminium and its alloys are also evaluated and related to the SLS process with a view to gaining useful insights especially in the aspects of liquid phase sintering (LPS) of aluminium alloys; application of LPS to the SLS process;

alloying effect in disrupting the surface oxide film of aluminium alloys; and designing of aluminium alloy suitable for the SLS/SLM process. Moreover, SLS/SLM processing parameters, including the process and the laser type; as well as the material-related variables; and their effects on the processing and densification of SLS/SLM fabricated parts are presented with a view to gaining an understanding of how to mitigate the deleterious effect of oxidation and ensuring good wetting and successful layer-by-layer consolidation of SLS/SLM processing of aluminium alloys.

Due to the paucity of publications on SLS/SLM processing of aluminium alloy powders, we review the current state of research and progress mainly from the perspectives of the SLS/SLM of ferrous (e.g. alloyed steels), non-ferrous alloys (e.g. titanium alloys), and composite powders. Meanwhile, ferrous, non-ferrous, and aluminium alloy powders are being considered together in this review because they are very reactive and form very stable oxides. Therefore, they all require the use of high vacuum or high-purity inert gas atmosphere for their processing. It is expected that insights to be gained from how SLS/SLM processing and material parameters promote mechanism of oxide disruption for achieving good microstructural and mechanical properties in ferrous, and non-ferrous powders could be helpful in understanding the disruption mechanism of aluminium oxides as well as the effect of processing and material parameters during laser processing. Thereafter, metallurgical microstructures, and processing defects found in SLS/SLM fabricated parts are discussed. The mechanical properties of SLS/SLM processed powders are also reported in this article. The final part of this paper explores the developments in

the field of SLS/SLM processing of metallic and composite powders as related to aluminium alloy powders, and outlines the trend for future research.

## **2 Variants of SLS/SLM Processing of Aluminium Alloys**

It was initially thought that the ease of manufacture by low cost conventional techniques such as casting and machining had made the application of SLS/SLM to aluminium alloys unattractive [48]. However, other reasons why there had not been much progress reported in the SLS/SLM of aluminium alloy powders include:

- the problem of the oxide film present on the surface of the metal powder, the thermodynamic stability of aluminium sesquioxide making it difficult to remove or avoid, and
- the relatively low melting point of aluminium which makes it difficult to find a suitable lower melting point binder material that belongs to the group of light metals in order to generate sufficient amount of liquid phase for binary liquid phase SLS processing.

In order to gain the basic understanding of SLS/SLM of aluminium alloy powders with a view to overcoming these challenges, the variants of SLS/SLM processing of aluminium alloy powders are hereby described as found in the available literature.

According to Kruth et al. [49], variants of SLS/SLM are *indirect* SLS which incorporates polymeric binding and debinding stages followed by infiltration; binary liquid phase SLS or *direct* SLS which combines a structural material remaining solid throughout the process and a binder material being liquefied with the structural and binder materials occurring in the form of coated grains, composite grains, and separate grains; partial melting SLS which occurs in a mixture of different powders (multiple phases) having no distinct binder and structural materials, bimodal powders, or single phase material; SLM which is able to achieve full melting in single component, single material powder; single component, alloyed powder particles; and fusing powder mixture; and laser initiated chemically binding mechanisms. It is pertinent to note that each SLS/SLM binding or consolidation mechanism culminates in the formation of final parts having significantly different microstructure upon comparison with the starting material via the manipulation of the SLS/SLM process parameters and the original powder properties presented in Table 2.

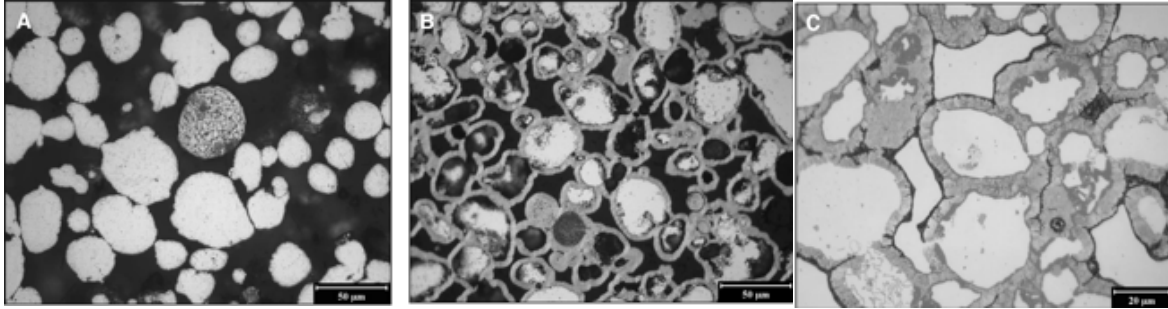
An extensive search through the available literature reveals the reservation associated with use of terminologies for describing SLS/SLM among researchers. For example, Uzunsoy & Chang [51] agreed with Simchi et al. [52] in regarding *indirect* SLS as sintering the base metal powder mixed with a polymeric binder with a low energy laser beam to produce a green part. After the sintering stage, the polymer is debinded and post-processed via infiltration in a furnace with a low-melting point alloy in order to enable the component produced attain full density.

**Table 2**

SLS/SLM process parameters and material variables influencing the processing and densification mechanism of fabricated parts [50].

SLS/SLM Processing Parameters	Material properties
Laser power	Viscosity
Scan rates	Surface tension
Atmospheric control	Particle size and distribution
Gas flow	Particle shape
Heaters (bed temperature)	Absorptivity/reflectivity
Laser type	Thermal conductivity
Scan radius	Specific heat
Scan vector length	Emissivity
Scan spacing	Melting temperature.
Thickness of layers	Component ratio
Machine (specific type)	Chemical composition.

Sercombe & Schaffer [53] also demonstrated *indirect* SLS of aluminium alloys (Fig. 3) involving the formation of an unconstrained, resin-bonded aluminium powder part, covering the part in a magnesium/alumina blanket, burnout of the resin, partial transformation of the aluminium into a rigid aluminium nitride skeleton by reaction with nitrogen atmosphere and the subsequent infiltration with a second aluminium alloy. Prior to post-processing, the parts obtained were characterised with low tensile strength as a consequence of the absence of any strengthening mechanism for the pure Al matrix.



(A)

(B)

(C)

**Fig. 3.** The microstructural development in *indirect* SLS of aluminium alloys. (A) green part (nylon binder in black, not visible); (B) aluminium nitride skeleton surrounding the aluminium grains; (C) infiltrated part [53].

As noted earlier on, coated grain, composite grain, and separate grain variants have been described as *binary* liquid phase SLS or *direct* SLS (Fig. 4). This involves the use of a powder blend consisting of two or more immiscible alloys of different melting point. In coated grains, a structural material is coated with the low melting point binder phase such that the binder material is preferentially melted by the impinging laser beam and eventually binds the structural particles together (Fig. 4A). Composite grains [39] are obtained via mechanically alloying consisting of the binder and the structural material within each individual powder grain with powder particles repeatedly milled, fractured and welded together (Fig. 4B).

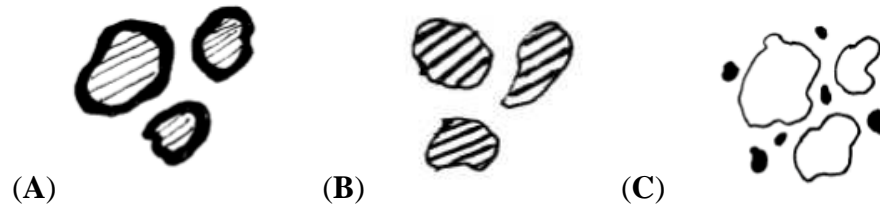


**Fig. 4.** Variants of *binary* liquid phase SLS or *direct* SLS (A) coated grains, (B) composite grains, and (C) separate grains [54].

The separate grain variant of the binary liquid phase SLS or *direct* SLS consists of blends of the larger particle sized structural material of higher melting point and the smaller particle sized lower melting point binder material (Fig. 4C). The binder particles are preferentially melted in order to bind the high melting point structural particles together. The preferential binder melting may be counteracted by higher reflectivity or lower laser absorption of the metallic binder material as compared to the structural material) with the combination of small binder particles and larger structural particles providing the benefit of better packing with small pores thereby favouring fast spreading of the molten binder via capillary forces and fast rearrangement of the particles [47]. Laoui et al. [55] employed a separate grain variant of the *binary* liquid phase SLS in which a mixture of ceramic particles (WC) remained solid throughout the production cycle and the metal particles (Co) were melted by the laser beam. Parts obtained via binary liquid phase SLS could not attain full density because adequate quantity of liquid phase for filling up the inter-particulate pores could not be formed (Fig. 5A). Consequently, post-infiltration of porous green parts with a low melting point material was incorporated into the process in order to enhance the dimensional stability, densification, and mechanical properties of parts (Fig. 5B).

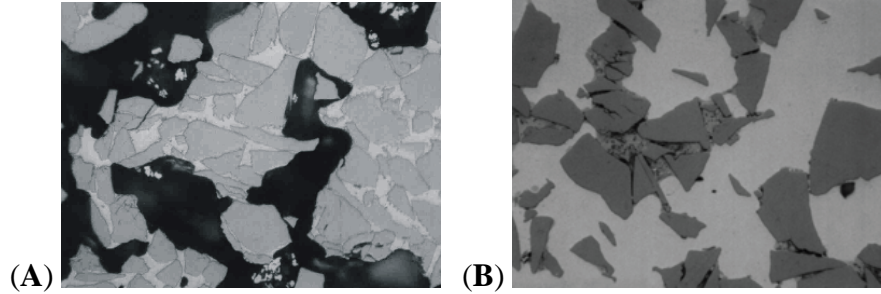


**Fig. 5.** LPS of WC-Co powder mixture; **(A)** before infiltration (grey portion: non-molten WC particle, white portion: molten Co, dark portion: porosity); **(B)** after infiltration with low melting point material (copper) [55].

Furthermore, partial melting variant of SLS also occurs in a mixture of different powders (multiple phases) having no distinct binder and structural materials; bimodal or multimodal powders; and single phase material [28, 29]. The partial melting variant of SLS was established in bimodal hypoeutectic Al-Si powders by blending the low melting point binder +45-75  $\mu\text{m}$  AlSi12 powder with higher melting point structural pure aluminium powders with varying particle size distribution, component ratio, and chemical composition [29]. Partial melting SLS occurred with the melting of the large sized binder AlSi12 particles which bound together the smaller sized particles of the structural components. The low melting point AlSi12 powders improved the energy efficiency of the partial melting SLS process when added to pure aluminium powder because it lowers the melting point of pure aluminium, thus requiring lower laser energy density. Furthermore, the addition of 9wt%Si is thought to have reduced the surface tension of the melt, thereby resulting in improved wetting behaviour. Because all the SLS processed blended hypoeutectic Al-Si powdered particles did not melt, therefore, the process

could not be described as “full melting” or SLM; hence, the name “LPS or partial melting” or SLS is preferred.

Dewidar et al. [56], while agreeing with Simchi and co-investigators [52] as well as Uzunsoy & Chang [51] on the definition of *indirect* SLS, approached SLM by directly heating a base-metal powder particles with the laser beam and thereafter infiltrated it with a lower melting point alloy in order to enhance the mechanical properties of the components. In assessing the work of Dewidar et al. [56], it may be argued that full melting was not achieved since infiltration of the porous SLS processed part with with a lower melting point alloy was carried out to achieve full densification. Rather, the study of Dewidar et al. [56] could only be described as *direct* SLS since partial melting must have been attained due to the choice of low laser power and low scanning speeds used during processing. Analysis of the cited literature on the SLS variants confirms that the amount of available liquid phase in the sintering pool controls the densification mechanism and the resultant microstructure of the SLS processed parts by altering the thermo-kinetic and thermocapillary properties such as viscosity, wettability, and rheological properties.

However, in agreement with Tang et al. [57]; Kruth et al. [49] described SLM as sintering the metal powder directly by the high-energy laser beam to achieve 100% density in a single step as opposed to *direct* or *indirect* SLS. A study of various SLM literature shows that it requires careful process control in order to avoid difficulties such as part distortion, balling and dross

formation in the melt pool that cause poor surface quality [47]. Meanwhile, apart from the properties of a material system, the choice of process parameters and the types of lasers used for consolidation could also determine whether SLS or SLM would be obtained for a typical material system. This could be attributed to the duration of the laser-material interaction which controls the degree of consolidation that may be obtained in a material system. High laser powers combined with low scanning rates would generate SLM whereas; high or low laser powers coupled with higher scanning rates would result in SLS. For instance, Olakanmi [40, 45] scanned single layers of Al, Al–Mg and Al–Si powders with a CO<sub>2</sub> laser (600µm beam diameter) by using combinations of laser powers and scanning speeds. The outcome of the study revealed that energy densities in the range of 12 to 16J/mm<sup>2</sup> were found to be the threshold below which SLS (at 100 – 240 mm/s and 50 – 150 W) was predominant and above which SLM (at 50 – 150 mm/s and 100 – 240 W) occurred. In contrast, Louvis et al. [27] obtained SLM for aluminium alloys by reducing the laser power required and increasing the laser scanning rates, while still producing components with a high relative density when they employed MCP realiser fibre laser. Furthermore, Burchibender et al. [24] achieved increased high build rate application of selective laser melting (SLM) of aluminium by using a new prototype machine tool including a 1 kW fibre laser and a multi-beam system.

Laser-induced *in-situ* chemical reactions have also been employed to fabricate Al/Fe<sub>2</sub>O<sub>3</sub> and Al/TiO<sub>2</sub>/B<sub>4</sub>C metal matrix composites (MMCs) [31, 32, 43]. In this process, the laser ignites and provides sufficient thermal energy to overcome the activation energy barrier of the reactants (Al/Fe<sub>2</sub>O<sub>3</sub> or Al/TiO<sub>2</sub>/B<sub>4</sub>C) thereby yielding adequate thermal energy to form chemical

compounds. In addition, this technique is preferred to the two-component powder method as a result of its inherent benefits in giving rise to fine and uniform distribution of compounds, improved consolidation and the release of exothermic energy that promotes the SLS/SLM response of the reactants [31, 32, 43]. *In-situ* chemical reaction synthesis combined with SLM opens a new door of opportunity to extend the capabilities of binary liquid phase SLS to process high melting point ceramic and intermetallic materials. There exists an optimal blending ratio of constituent materials in the newly developed MMCs and an optimal set of processing parameters for which the release of large amount of thermal energy and the *in-situ* chemical reaction are controllable with the attendant benefits of reducing the price and running expenditure of an SLM machine, thereby widening its versatility. Composite fabrication via SLS/SLM combined with *in-situ* chemical reaction processing is gaining wide acceptance because the processing speed is fast, the technology is simple, the time and energy of the preparation are saved and manufacturing cost is low.

Although, SLM employs a laser beam to consolidate metallic powders in an attempt to achieve 100% density (SLM) in one step, its demerit include the occurrence of balling which inhibits inter-particulate melting as a consequence of the presence of the surface oxide film on the surface of powder particles which prevent wettability of the liquid metal with its solid form due to the initiation of Marangoni convection [47, 49]. Another setback to SLM is the occurrence of part distortion or layer delamination due to high temperature gradients [47, 49]. In assessing the different approaches of SLS/SLM elucidated earlier on in this section, it is clear that some approaches have been developed from a desire to produce a specific material system. According

to Dalgarno & Wright [58], the desire to process materials using *direct* SLS/SLM approach is because such materials may be difficult and expensive to process conventionally. Moreover, the feasibility of fabricating aluminium alloy parts in *direct* SLS/SLM will make realisable the benefits of time saving, and cost reduction over the *indirect* SLS with a polymer binder by not requiring de-binding and post-processing steps. Although, the possibility of fabricating parts in SLS/SLM depends on fundamental material issues, the processing conditions which allow direct SLS/SLM, and the size of the component which is to be fabricated; however, *indirect* SLS with a polymer binder is likely to continue to offer the processing of widest range of materials, because it concentrates on only using laser scanning to generate shape, with a wide range of subsequent processes available to generate strength and consolidate the part [58]. Moreover, *binary phase* SLS appears promising for the processing of composites being one of the methods to build near net shape parts of 3D complexity. From the point of view of the quality of part produced, the main drawback of the technique resides in the inherent high level of residual porosity which requires a post treatment such as re-sintering or infiltration. Additionally, the surface finish obtained is rougher compared to parts obtained by powder compaction. Future work needs to concentrate on developing a better understanding of processes such as SLS/SLM-induced *in-situ* chemical reactions in producing nanocrystalline aluminium alloy-ceramic composites with a view to improving the density and mechanical properties of parts.

### **3 Relevance of Powder Metallurgy, and Pulsed Electric Current Sintering (PECS) to SLS Process of Aluminium Alloys**

At present, very little work has been reported on the SLS/SLM of aluminium alloy parts. This section will only relate conventional powder metallurgy (P/M) and pulsed electric-current sintering (PECS) of aluminium alloy powders to the SLS process, with a view to gaining relevant insights into liquid phase sintering (LPS) of aluminium alloys; application of LPS to the SLS process; alloying effects in disrupting the surface oxide film of aluminium alloys; and designing of aluminium alloys suitable for the SLS/SLM process.

#### *3.1 Powder Metallurgy (P/M) Liquid Phase Sintering (LPS)*

The adoption of liquid phase sintering (LPS) in the SLS processing has the benefits of low sintering temperature, fast densification, homogenisation, high final densities, and microstructures that often possess improved mechanical and physical properties. With regards to SLS, an essential requirement for the effective liquid phase sintering is the transient wetting liquid (formation of sufficient liquid phase within short durations varying between 0.5 to 5ms) which promotes metallurgical bonding or inter-particulate melting across the layers of sintered components. German [59] considered the schematic binary phase diagram shown in Fig. 6 and suggested the key features of an ideal liquid phase sintering system to be:

- (1) The additive A should have a lower melting point than the base B. The alternative is a low melting point eutectic which does not form liquid phase on spontaneous heating.
- (2) The solubility of the additive A in the base B should be low for the additive to remain segregated to particle boundaries. This increases the liquid + solid range and the volume of liquid for a given amount of the second added component.
- (3) The base should be soluble in the liquid and it should also have a high diffusivity in the liquid in order to ensure high rates of mass transport and therefore rapid sintering.

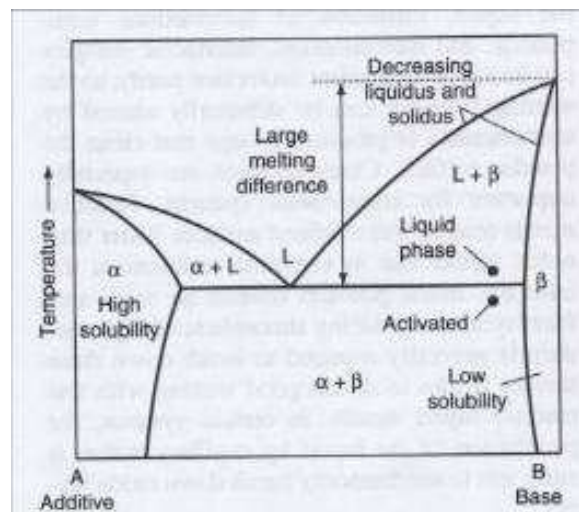


**Fig. 6.** Phase diagram of an ideal system for LPS [60].

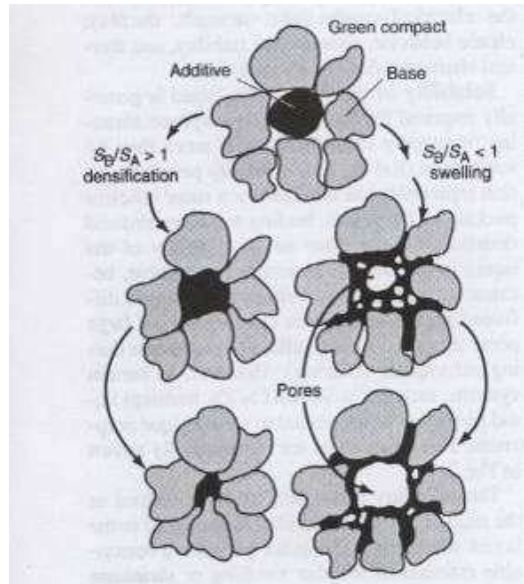


**Fig 7.** A schematic diagram contrasting the effects of solubility on densification or swelling during LPS [60].

Solubility of the solid in the liquid is a necessary pre-requisite for successful LPS with regard to systems having more than 65vol% solid [60]. Solubility promotes re-precipitation and increased efficiency in particle arrangement thereby leading to increased sintered density. As noted earlier on, solubility of the liquid in the solid is not preferred due to swelling as the liquid which diffuses into the solid grains leads to formation of porosity which is difficult to remove upon subsequent sintering. Fig. 7 suggests that transient liquid phase can be controlled to produce desirable properties as exemplified in Cu-Sn and Cu-Zn systems. The solubility parameter ( $S$ ), which determines whether swelling or shrinkage occurs during LPS, is the ratio of the solid solubility ( $S_B$ ) in the liquid to the liquid solubility in the solid ( $S_A$ ). Table 3 presents the solubility effects on densification in LPS for various material systems.

**Table 3**

Solubility effects on densification in LPS [60].

Base	Additive	Solubility (at.%)	ratio,	Behaviour
Al	Zn	0.004		Swell
Cu	Al	0.1		Swell
Cu	Ti	4		Shrink
Fe	B	7		shrink
Fe	Cu	0.07		Swell
W	Fe	5		Shrink

In regards to SLS processing, the actual amount of dimensional change is a function of the processing conditions. Phase diagrams are useful in identifying solubility parameters and other features that promotes LPS [60]. A study of an ideal phase diagram for LPS (Fig. 6) reveals that a deep eutectic is preferred due to significant reduction in sintering temperature with the formation of liquid phase. The formation of intermediate compound is generally unfavourable. High-temperature phases can reduce diffusion rates, while brittle intermetallic phases that form during cooling can degrade mechanical properties.

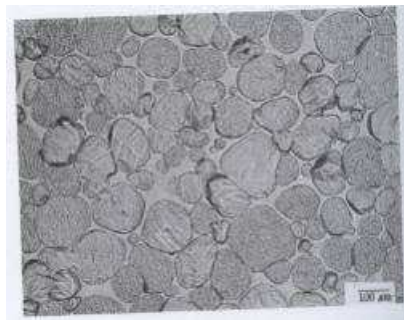


**Fig. 8.** Typical microstructure of a LPS system with the phase diagram characteristics shown in Fig. 6 [60].

Furthermore, a phase diagram reveals the tendency of alloying elements and impurities to segregate to the interfaces with a downward sloping liquidus and solidus indicating a propensity for solute segregation and lower surface energies [60]. Therefore, a sintering temperature just above the eutectic temperature is optimal for a composition in the  $L + \beta$  region. A typical LPS microstructure is shown in Fig. 8 which consists of relatively large, rounded grains suspended in a liquid matrix, with the degree of grain contact governed by the dihedral angle. In a system that lacks solubility of the solid in the liquid phase, a rigid skeletal structure is expected with densification controlled by solid state diffusion. Use of extremely fine starting powders or segregating activators that promote solid-state sintering in the presence of the liquid ensures high sintered densities are obtained.

Schaffer and co-workers [61] examined the behaviour of a number of likely candidate alloys and discovered that Al-Sn, which follows very closely the ideal characteristics described in Fig. 6, had a much more desirable sintering response than either Al-Cu or Al-Zn, both of which have at least one ideal characteristic. On this premise, they designed the Al-Sn-Mg system for uncompacted sintering and were able to achieve near full theoretical density. However, the tensile strength of the Al-Sn system was poor because tin could not provide much strengthening whereas Mg addition in the Al-Sn-Mg system improved tensile strength. This confirms the potency of Mg in disrupting the surface oxide film of aluminium, thus, promoting metal/metal bonding. Meanwhile, it is hereby speculated that the addition of tin could have reduced the strengthening effect of magnesium in the Al-Sn-Mg powder.

P/M aluminium alloys can be improved without recourse to hot working or master alloy powders if their design is based on an understanding of the underlying sintering processes and the characteristics of an ideal liquid phase sintering system [61]. However, this idea can be applied to the design of suitable aluminium alloys for the fabrication of parts in SLS process with a view to ensuring that the oxide phase of the aluminium powders is disrupted in order to make allowance for effective inter-particle bonding/melting across the layers so as to achieve the production of full density parts. This entails the determination of the appropriate chemical composition of aluminium alloys that make allowance in their thermal cycle for the transient nature of the adequate liquid phase during SLS in addition to the alloying elements contained in them effectively disrupting the surface oxide of the aluminium powder. Furthermore, designing such SLS processable aluminium alloys necessitates that the mechanism of disruption of their surface oxide film need to be understood. Therefore, an investigation is necessary to ascertain if alloys of the same composition as those employed in the press and sinter technique could give equivalent or a better sintering response during SLS without the application of hot working processes. If this is not the case, alloys that would give desirable response to SLS need to be designed.

### *3.2 The Application of Liquid Phase Sintering (LPS) to SLS Process*

According to Agarwala et al. [50], the most applicable of all the binding mechanisms to SLS is the liquid phase sintering/partial melting (LPS) which incorporates the melting of the binder material of lower melting point thereby binding together the particles of the structural

components of the system. Moreover, the improvement obtained in the mechanical and microstructural properties of SLS processed components depends on the success or otherwise of the LPS with regard to the amount of liquid phase present. Powder properties such as the size distribution and shape of the powder particles, as well as particle arrangement play an important role in determining the ideal SLS liquid phase condition. If the processing and powder parameters are poorly controlled, difficulties such as balling, microstructural agglomeration, layer delamination and porosity are bound to be encountered during the SLS of metals due to the initiation of Marangoni convection, and uneven thermal gradient on the powder bed. These problems may also arise as a result of improper arrangement of the powder particles on the sintering bed. While the role of component ratio of binder material in the SLS of metals will be presented in this section, the roles of processing parameters as well as powder properties will be discussed in Section 4.2.1.

An appropriate choice of the amount (measured in weight percentage) of binder materials (which represents the amount of liquid phase formed if complete melting of the binder is assumed) has been shown to overcome some of the SLS challenges highlighted in the preceding paragraph. Gu & Shen [62-65] demonstrated that there exist optimal component ratios; for each of WC-Co particulate reinforcing Cu matrix composites; multi-component Cu-based metal powder; and sub-micron W-Cu / micron Cu powder mixture systems. At the binder's optimal component weight ratio, high densification and homogeneous sintered microstructure are obtainable as a consequence of favourable viscosity of liquid-solid mixture and the sufficient re-arrangement of binder and structural particles. However, they noted that when binder content

falls below its optimal component weight ratio for each of these systems, severe particulate aggregation occurs due to limited liquid formation and the resulting high liquid viscosity due to high solid fraction and reduced Marangoni effect.

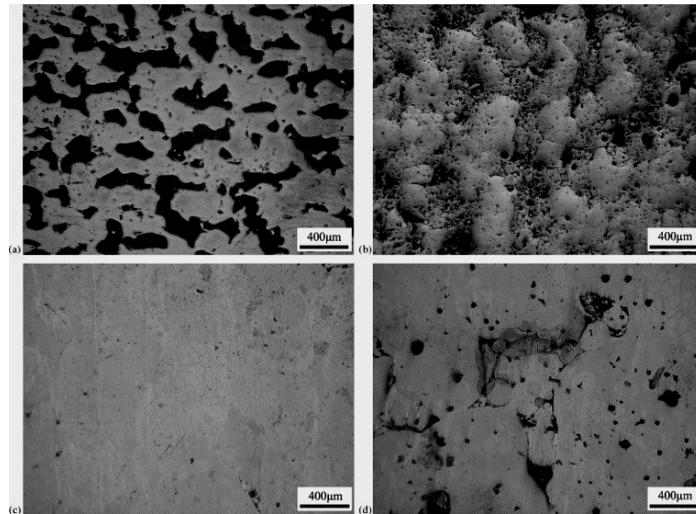


**Fig. 9.** Optical images of the polished sections of the laser sintered multi-component Cu-based metal powder with varying contents (wt%) of binder CuSn in the samples (a) 20 (b) 35 (c) 50 and (d) 65 [63].

With the binder content increasing beyond its optimal component ratio, the laser sintered densities of the parts made in each of these powder systems deteriorates because of the initiation of the balling phenomenon and uneven thermal gradient. Experimental evidence has revealed that the fractional amount of liquid phase yielding optimal densification and homogeneous microstructure (Fig. 9) for the SLS of various powder systems are as shown in Table 4. In conclusion, all these studies attest to the fact that the determination of the optimal liquid phase

amount for SLS, for which a pore-free microstructure is obtainable, is complex and significantly influenced by chemical composition and component ratio which in turn is affected by the packing density of the blended powder bed as well as the viscosity of the laser sintered powders powder systems.

**Table 4**

Fractional amount of liquid phase generated in various SLS processed metal systems.

Material	Binder material	Fractional liquid phase.	Ref. No.
Multi-component based metal powder	Cu- CuSn	0.5	[63]
Sub-micron WC-Cop / Cu bulk metal matrix composites	Cu	0.7	[64]
Sub-micron W-Cu / micron Cu powder mixture	Micron Cu powder	0.6	[65]
Fe-Cu system	Cu	0.3	[66]

It is now evident that the fraction of liquid phase available in the sintering pool of SLS of metals determines the densification and microstructure of the laser processed parts by influencing the thermo-kinetic and thermocapillary properties such as viscosity, wettability and rheological characteristics [50]. Table 4 suggests that provided appropriate SLS processing parameters are used, the optimal liquid fraction existing at the binder's optimum component ratio is dependent on the energy gain of the powder and is partly controlled by the weight fraction of the binder in the powder mixture.

### *3.3 Oxide Disruption in Pulsed Electric Current Sintering (PECS) Processed Aluminium Alloy Powders*

Xie et al. [67] studied the behaviour of oxide films at the interface between pure Al powdered particles in pulse electric-current sintering (PECS) and its effect on the properties of the sintered specimens. It was shown that the occurrence of direct metal/metal bonding interfaces increases the mechanical properties of the sintered aluminium powder whereas the metal oxide film layer/metal bonding interfaces produced contrary effect on its mechanical properties. This finding established that by increasing the loading pressure at high sintering temperatures, or increasing the sintering temperature under loading pressure, the breakdown of the oxide film was promoted. Moreover, Xie et al. [68] investigated the reduction mechanism of the surface oxide film and microstructure of interfaces between powder particles in Al-Mg alloy specimens sintered by pulse electric-current (PECS) process. They established that nano-sized crystalline precipitates, which may be  $\text{MgAl}_2\text{O}_4$ ,  $\text{MgO}$ , or both, were formed by the reduction reaction by magnesium and were observed in all of the Al-Mg alloy specimens which they studied. They attributed the type of crystalline precipitates formed to the variation in the Mg content in the alloy powder and the sintering temperature.

Furthermore, Liu et al. [69] showed that particle shape seems to be a significant factor controlling the P/M sintering response of uncompact aluminium powder. In addition, they suggested that the differential thermal expansion between the aluminium particle and its oxide film may cause the oxide skin to fracture and that the fracture characteristics differ as a

consequence of powder morphology. It was elucidated that the oxide shell in irregularly shaped particles tend to crack and heal more frequently than in smooth, spherical shaped particles because of the tendency of the irregular particles to scavenge more oxygen during heating than spherical particles. It was also posited that this eventually resulted in greater weight gain observed in the sintered irregular powder particles than the spherical particles due to outer layers made from irregular particles providing a more effective autogenous gettering zone than outer layers made up of spherical particles. Therefore, it can be inferred that the sintering mechanism of aluminium powders can differ on the basis of the sintering technique adopted, chemical composition, and particle surface morphology. Moreover, it is evident from the cited literature that oxide cleanliness is important in order to achieve inter-particulate bonding if parts having structural integrity will be fabricated via SLS/SLM. Therefore, a mechanism elucidating the reduction of the surface oxide film during SLS/SLM processing of aluminium powders need to be proposed as well as the associated factors that aid or inhibit its occurrence in practice.

### *3.4 Alloying Design for the SLS Process*

To fabricate components using the binary liquid phase SLS process, sintering from a low green density to a high final density is required. To achieve this aim, the use of additives that promote the formation of liquid phase and improve wettability is a simple and inexpensive technique that is feasible. Many researchers have expended significant efforts in attempting to increase densification by improving the wettability in SLS. Among numerous approaches adopted by various research groups are the use of *in-situ* deoxidiser or fluxing agent, and

alloying additions. This section is devoted to a review of the literature on the use of fluxing agents and alloying additions to enhance the densification mechanism in SLS processed powders.

Fluxing agents which are used in brazing and soldering can improve wetting effectively during sintering due to their ability to de-oxidise and reduce the surface tension of the solid-liquid-vapour interface [70]. Agarwala et al. [50] examined the role of phosphorus in SLS of bronze (Cu-10wt%Sn)-nickel powder. They were able to determine an optimum processing window for which a density of around 70% was obtained without any significant balling or spheroidisation. Zhu et al. [71] found the formation of  $\text{Cu}_2\text{O}$  in a copper-based powder (Cu-40%wtSCuP) to be sensitive to the scan spacing as a consequence of a lack of  $\text{Cu}_3\text{P}$  protection under the re-heating condition if a small scan spacing was used. Moreover, they discovered that atomic diffusion was the densification mechanism at fast scan speed and high scan spacing whereas solute-precipitation was noted to be the predominant mechanism for densification at low scan rates and small scan spacings. Although, Zhu and co-workers [71] did not elaborate on the role of  $\text{Cu}_3\text{P}$  in improving wetting between sintered layers and enhancement of densification, Zhu et al. [70] investigated the influence of varying contents of brazing flux on the wettability and densification in the direct laser sintering of Cu-based metallic powder (Cu-40%wt.SCuP). Their findings revealed that small amount of flux increased the densification and sinterability. A large amount of flux additive had a negative effect, however, with balling taking place and a residual covering of flux on the surface leading to a deterioration of adhesion between the sintered layers [70].

On the basis of the characteristics of phase diagrams of ideal sintering systems, alloying elements have been used to enhance the sintering behaviour of metallic systems (see Fig. 6 in Section 3.1). In these systems, the mechanism of enhancement is the formation of eutectic liquid phase and, since the solubility of the additive in the structural metallic component is low, the liquid remains segregated to particle boundaries. Sercombe [72] added boron to maraging steels with the aim of producing high hardness rapid tooling. His findings showed that the reaction of 0.4% boron with the alloying elements in the maraging steel resulted in the formation of Mo- and Ti- rich borides, thereby providing a liquid phase for enhanced sintering to produce a near full density component. Chen et al. [73] also found that the inclusion of titanium in steel samples improved the bonding of the sample to the substrate and reduced the extreme hardness of the material. A search of the literature on the effect of alloying elements on the densification mechanisms of SLS processed aluminium powders has yielded no result. Hence, in order to gain an understanding of the role that alloying additions play in the sintering/melting of aluminium powders, results from conventional powder metallurgy must be considered.

It is an established fact that trace elements facilitate the sintering of aluminium and its alloys by the formation of liquid phase. This initiates a change from the solid state to liquid phase sintering with corresponding increase in sintering rates. Sercombe & Schaffer [74, 75] had observed that trace additions (0.1 wt%) of Sn, Pb, Bi, and Sb enhanced densification during sintering of aluminium alloys and dramatically improved their tensile properties. This observation could be attributed to the high vacancy binding energy of the trace elements used as well as their insolubility. Schaffer et al. [76] proposed a mechanism by which as little as

0.07wt% lead, tin, or indium promotes sintering in an Al-Zn-Mg-Cu alloy. They stated that the sintering enhancement was as a result of the segregation of the micro-alloying additions to the liquid-vapour interface thereby lowering the effective surface tension of the oxides. McPhee et al. [77] discovered that the segregation of iron into the inter-granular liquid pools retards the liquid film migration rate in aluminium alloys while alloys with low iron levels develop few intergranular pools and have higher sintered densities. Delgado et al. [78] examined the effect of the second liquid phase coming from the addition of eutectic Al-Si on the super solidus liquid phase sintering (pre-alloyed powder) and liquid phase sintering (pre-mixed powders) of Al-Cu 2XXX series. Their result showed an improvement in AA2014 (Al-4.4wt%Cu-0.7wt%.Si-0.4wt%Mg) densification and mechanical properties but the product was noted to have been bedevilled with porous microstructure while Alumix 123 (Al-4.4%wt.Cu-0.6%wt.Si-0.5%wt.Mg) densification and microstructure improved by having lower amount of porosity but had lower bending strength. MacAskill et al. [79] studied the effects of magnesium and tin on the sintering response of air atomized aluminum powder by considering nature of the raw powders and their concentrations. MacAskill and co-investigators [79] established that magnesium additions improved the sintering response of the aluminum powder and increased the propensity for reaction with gaseous nitrogen while tin dampened this effect. They concluded that the most desirable sintering response was obtained for Al-1.5Sn-1.5Mg alloy. Moreover, Gökçe et al. [80] reported on the sintering kinetics of aluminum powder pre-mixed with copper and magnesium powders at both macro- and micro-level respectively with a view to producing light and strong Al-based powder metallurgy alloys. They discovered that high strength Al-based powder metallurgy alloys were developed with good microstructure from the pre-mixed

elemental Al5Cu and Al5Cu0.5Mg compositions with the transverse rupture strength value after sintering of the base Al powder increasing five times from 84 MPa to 466 MPa.

The foregoing discussion shows that the sintering mechanism of various aluminium alloys differ depending on specific micro-alloying elements and, sometimes, the bulk alloy composition. The insight gained from the powder metallurgy (P/M) studies on the effect of trace elements on the densification of aluminium alloys could be useful in the SLS/SLM processing of aluminium alloys. This could be applied by investigating the effect of alloying elements on the sintering mechanisms of various aluminium alloys under the SLS/SLM processing conditions. This investigation is very important because the SLS/SLM processing technique differs significantly from the conventional sintering process. Furthermore, from the available literature, no in-situ-deoxidiser or fluxing agents has been developed for aluminium alloys such that it could promote wettability between the various layers thus improving densification. The requirement for such an in-situ-deoxidiser or fluxing agent should be such that it would not leave any residue on the layers which could impair the coherence of the layers of the components being formed.

## **4 Effects of Processing Parameters and Powder Properties on the SLS/SLM Processing and Densification of Powders**

Metallic powders have a higher degree of contamination by moisture, organics, adsorbed gases, oxide and nitride films on particle surfaces due to their much higher surface area per unit volume when compared to cast or wrought components [46]. These contaminants not only inhibit successful wetting, which promotes interlayer bonding and densification of the melted powder, but also degrade the mechanical properties and part geometry of the consolidated component during SLM [46]. SLM of metals is considered to be far more difficult than the laser sintering of polymers, direct or indirect SLS of metals because of the oxidation, balling and uneven thermal gradients across the layers which may cause poor interlayer bonding, low density, weak strength and rough surface of the SLM processed part [8, 46, 57, 81]. For this reason, findings from several studies have described SLS/SLM as a very complicated process, and suggested that several parameters influence the densification mechanism and the attendant microstructural features of materials processed by SLS/SLM. The main process parameters that determine the processing as well as the quality characteristics of a component fabricated by SLS/SLM technique are as listed in the first column of Table 2 whereas the characteristics of powder material which are of special concern are listed in its second column.

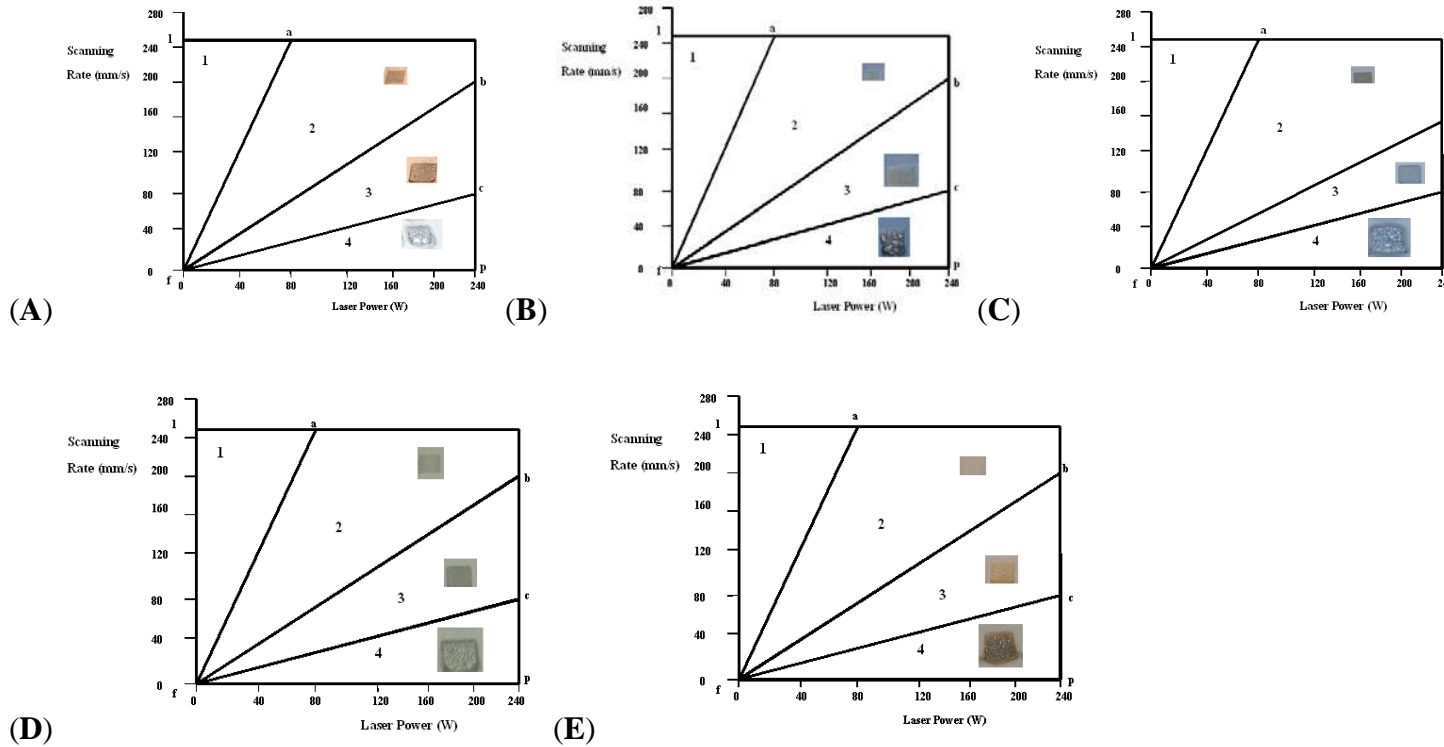
In an attempt to mitigate the deleterious effect of oxidation as well as ensuring good wetting and successful layer- by-layer consolidation in direct laser sintering of metals, various approaches have been adopted by SLM investigators: sintering in an inert atmosphere like argon,

neon, and nitrogen which renders the oxidation process inactive or slows it down; disruption of the surface oxide film by alloying addition; determining the optimal processing parameters that allows minimal balling; re-melting of the underlying substrate in order to break down the surface contaminants to ensure a clean surface at the atomic level between the solid and the liquid; and incorporation of fluxing additives [5, 45, 46, 61, 71, 76, 81-85]. The objective of this section is to determine from the available literature, the possible effects of the SLS/SLM parameters and powder properties on the processing and densification phenomena of components produced from aluminium alloys. Where literature on SLS/SLM processing of aluminium alloy powders are not readily available to elucidate their SLS/SLM response, studies on ferrous (e.g. steel, iron) and non-ferrous (e.g. titanium e.t.c.) powders have been employed to achieve the aim of this section. As noted earlier on, these alloyed powders are being considered together in this section because they are very reactive and form very stable oxides. Therefore, they all require the use of high vacuum or high-purity inert gas atmosphere for their processing. It is expected that insights to be gained from how processing and material parameters promote mechanism of oxide disruption for achieving good microstructural and mechanical properties in these powders could be helpful in understanding the disruption mechanisms of aluminium oxides as well as how processing and materials parameters favour this during laser processing.

#### *4.1 SLS/SLM Processing Windows of Aluminium Alloy Powders*

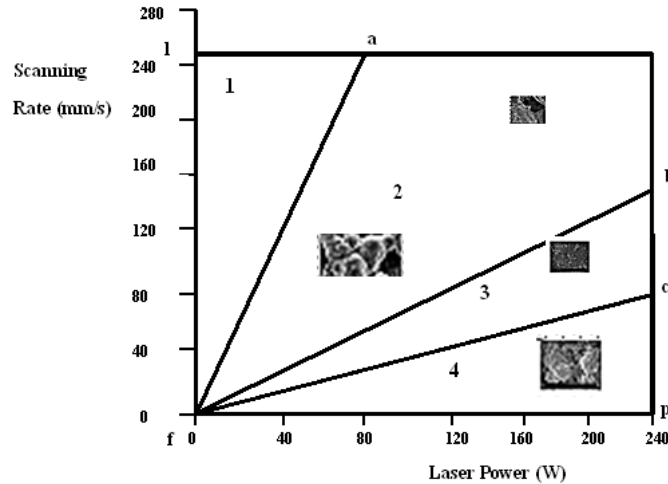
In order to gain an in-depth understanding of the consolidation behaviour of SLS/SLM processed aluminium alloys, it is important that the processing windows which allow for the

construction of continuous surfaces devoid of balling phenomenon in order to build multiple layers must be established. The processing windows for pure- Al, pre- alloyed Al-Mg, and AlSi12 powders were investigated by employing laser power and scanning speeds in the range of 20-240W and 20-250mms<sup>-1</sup> respectively at a constant scan spacing of 0.1mm [40, 45]. Four regions of behaviour identified for all powders were: no marking, partial marking, good consolidation, and excessive balling (Fig. 10). The processing windows (Fig. 10A to E) show similar trends for all powders investigated, although, there were differences in the location of boundaries of the different regions between powders. The region of partial marking, even though coherently bonded, was characterised by the occurrence of very low strength single layer samples which could not be held by hand without fracture occurring; whereas the region of good consolidation consists of coherently bonded layers having high strength which enables the samples to be held by hand. The area of good consolidation should be a favourable region for the construction of multiple layers in SLS/SLM while the region of excessive balling which is undesirable is characterised by the formation of large size melt pools which hinder the construction of subsequent layers.



1: No marking; 2: Partial Marking; 3: Good Consolidation 4: Excessive Balling

**Fig. 10.** Processing window for single layer parts made in (A) air atomised pure aluminium (AL-1) (B) gas atomised pure aluminium (AL-2) (C) water atomised Al-5.6Mg (AL-3) (D) water atomised Al- 6Mg (AL-4) and (E) gas atomised Al-12Si AL-5 powders (AL-5) (Note: Reciprocals of slopes f-a, f-b, and f-c, were computed and multiplied by the reciprocal of scan spacing (0.1 mm) in order to obtain the applied energy density). Processing conditions are laser powers (20-240W), scan rates (20-250mms<sup>-1</sup>), and scan spacing 0.1mm [40].



1: No marking; 2: Partial Marking; 3: Good Consolidation 4: Excessive Balling

**Fig. 11.** Relationship between the various regions of processing map and the surface morphology of SLS/SLM processed aluminium powder at a laser power of 150 W, scan spacing of 0.1 mm, and varying scanning rates [40].

Fig. 11 depicts the relationship between the various regions of processing map and the surface morphology at a laser power of 150 W, scan spacing of 0.1 mm, and varying scanning rates for aluminium alloy powders when its single layer coupons were produced on the powder bed substrate. At scanning rates below 80mm/s, the pores appeared to be large in size and the inter-agglomerates were fully dense as the laser increases. This corresponds to the excessive balling region of the processing map. Further increment in the range of scanning rates between 80mm/s to 150 mm/s when laser power varies between 120 W to 240 W, resulted in formation of fairly dense structures consisting of small closed pores (region of minimal balling). As the laser power varies from 50 W to 240 W at high scanning rates (150 to 240 mm/s), surface morphology

appeared smooth, but less dense while it was characterised with lateral pores (region of partial marking). These observations conform to the discoveries made by Niu & Chang [5] in their studies on the SLS of M2 high speed steels. An observation of the surface morphology of SLS/SLM processed samples revealed that the agglomerates were no longer seen in samples AL-1, AL-2, AL-3, and AL-4 powders, but were replaced by a continuous skeleton structure. However, a fairly dense structure with closed pores whereas a relatively smooth and almost fully dense sintered surface was obtained for AL-5. This indicates that pre-alloyed elements in the aluminium powders influence the evolution of the nature of its surface morphology during SLS/SLM processing.

Moreover, the existence of the observed regions in the processing windows with the associated surface morphologies could be attributed to the following reasons:

- The existence of the region of “no marking” (Fig. 10) is affected by the extremely short duration of laser-material interaction/lowest energy density (less than  $3.2 \text{ J/mm}^2$ ) which permits no inter-particulate bonding to take place due to the adoption of scanning velocities above  $50 \text{ mm/s}$  at laser powers less than  $80 \text{ W}$  during SLS process.
- The formation of the “partial marking” region (Fig. 10) in which the morphology of laser sintered surfaces is characterised by a network of agglomerates with a large amount of small, open, and deep pores (Fig. 11) could be explained by the generation of lower energy density ( $3.3$  to  $10 \text{ J/mm}^2$ ) resulting from the adoption of laser powers ranging from above  $80$  to  $240 \text{ W}$  at scan rates varying between  $80$  to  $250 \text{ mm/s}$ . This condition

leads to the generation of inadequate liquid phase that consequently produce low inter-particulate bonding evident in Fig. 11.

- The attainment of the region designated “good consolidation” (Fig. 10) which is characterised by almost or fairly (i.e. 60 to 80%) dense structures consisting of closed pores (Fig. 11) could be ascribed to the adoption of higher energy densities in the range of 12 to less than 30 J/mm<sup>2</sup> which leads to the formation of adequate amount of liquid phase that promotes full melting. This outcome is in agreement with findings from Khan & Dickens [86]. The energy densities resulting in the formation of “good consolidation region” are derivable from laser power ranging between 100 to 240 W and scan rates varying between 80 mm/s to 200 mm/s. It is believed that energy densities in the range of 12 to less than 30 J/mm<sup>2</sup> increase the powder bed temperature, while reducing the viscosity of molten pool of the SLM processed powders, thereby facilitating more efficient densification with the solid powdered particles as elucidated by Khan & Dickens [86].
- Furthermore, the occurrence of rough and 100% dense structures (Fig. 11) associated with the region of “excessive balling” (Fig. 10) could be ascribed to the highest range of energy densities resulting from the combined effect of higher laser powers at the lower scan rates (80 mm/s or less). Similar to findings from Zhang et al. [87], energy densities from 30 J/mm<sup>2</sup> or more generated at this instance is believed to have led to the formation of excess amount of liquid phase that resulted in the formation of balling (Fig. 11).

From the foregoing discussion, an energy density in the range of 12 to 16 J/mm<sup>2</sup> was found to be the threshold below which SLS was predominant and above which SLM of aluminium powders occurred. This implies that the occurrence of various regions (Fig. 10) in the SLS/SLM processing window as well as the attendant microstructure is dependent on the laser energy density (see Eq. (1)) that generates a varying amount of liquid phase for inter-particulate bonding/melting, rather than laser power or scanning rate in isolation.

$$\psi = P/uh \quad (1)$$

where  $\psi$  is the specific laser energy input,  $P$  is the laser power (W),  $u$  is the scan rate (mm/s); and  $h$  is the scan spacing (mm).

Finally, the four regions identified in Olakanmi's [40] study are similar to the regions reported for direct SLS/SLM processing maps studies on gold, and Mg-9Al powders by Khan and Dickens [86]; and Zhang et al. [87] respectively.

Further comparison of the SLS/SLM processing windows for AL1, AL-2, AL-4 and AL-5 (Fig. 10A, B, D, and E) reveals that they are all identical as exemplified by the occurrence of the region of good consolidation for all the powders when scanning rates were varied between 80 mm/s to 200 mm/s when laser power in the range of 100 to 240 W were applied. This behaviour could be attributed to the powders' tapping densities (Fig. 12) which are similar to one another and influence their thermal conductivities. Although, oxide content (Table 5) in AL-1 (15.9wt %) is higher than that of AL-2 (6.5wt %), AL-4 (4.6wt%), and AL-5 (2.8wt%) while the powder densities (Fig. 12) for all the powders are similar. This implies that predominant differences in

the oxide contents of pure aluminium powders AL-1, AL-2, AL-4, and AL-5 appear to have little or no effect on the nature of processing maps obtained for them. The processing map for AL-3 (Fig. 10C) reveals significant differences in its features when compared with other powdered samples as illustrated in the processing condition for the region of good consolidation: scan rates varying between 80 mm/s to 150 mm/s for AL-3 at the instance when the applied laser power was between 120 to 240W. A cursory look through the powder properties shows substantial differences in the powder densities, but similar oxide and magnesium contents (Table 5) for AL-3 and AL-4 powders (Fig. 12). Since the differences in oxide contents of the powders have little or no influence on the processing maps of powders, it may be suggested that the similarity in the oxide and magnesium contents of AL-3 and AL-4 has little or no influence of their processing maps.

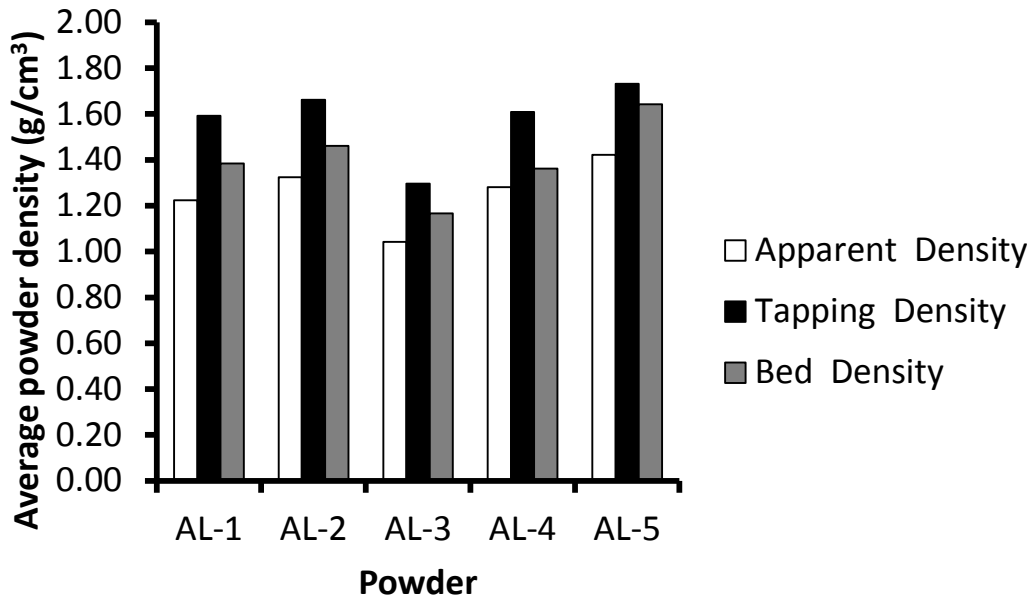


**Fig. 12.** Apparent, Tapping, and Bed densities of the aluminium powders [40].

**Table 5**

Elemental Composition of the Powdered Samples by Semi-quantitative EDS Analysis (weight %) [40, 45].

Powdered Samples	Aluminium	Magnesium	Silicon	Oxygen
AL-1	84.1	-	-	15.9
AL-2	93.5	-	-	6.5
AL-3	89.3	5.7	-	5.0
AL-4	89.4	6.0	-	4.6
AL-5	85.1	-	12.1	2.8

Therefore, significant differences noted in the processing maps of AL-3 when compared with other powders could be attributed to the variations encountered in their tapping densities. As such, the degree of sphericity of AL-3 particles is significantly lower than that of other powders (Fig. 12). In line with German's [89] observation that irregularly shaped particles characterised by high surface area per unit volume have the tendency to absorb more thermal energy during P/M sintering. Therefore, it is evident that higher content of irregular particles in AL-3, than is found in other powders is responsible for the occurrence of the good consolidation region at lower boundary of the scan rates (80mm/s to 150 mm/s) as the nature of its particle morphology requires more laser energy density for its melting. Moreover, the similarities existing in the processing maps of AL-1, AL-2, AL-4 and AL-5 as a consequence of similarities in their tapping densities suggest that alloying additions of magnesium and silicon to aluminium powders have no predominant effect on the processing map boundaries of these powders. Rather,

alloying addition has a significant effect on the nature of the evolved surface morphology of SLS/SLM processed aluminium powders in their processing windows.

Dadbakhsh et al. [33] also examined the role of  $\text{Fe}_2\text{O}_3$  additives in the development of the SLM processing window of pure aluminium powder. They reported that *in-situ* material reaction between Al and  $\text{Fe}_2\text{O}_3$  powder released extra heat and energy which promoted the formation of a molten pool and improved the SLM processability over a wide range of SLM parameters. The released energy (which is proportional to  $\text{Fe}_2\text{O}_3$  content) is capable of manipulating the visual surface profile and roughness. Higher amounts of  $\text{Fe}_2\text{O}_3$  additive were found not to have provided a positive effect on the part density as inclusions suppress fluidity, which presumably is more effective than that of extra heat to increase fluidity. However, irrespective of the negative influence of increasing content of  $\text{Fe}_2\text{O}_3$  on density, hardness significantly increases with higher  $\text{Fe}_2\text{O}_3$  content because of the superior microstructural features of a particle reinforced matrix.

The processing windows (Fig. 13) plotted on the basis of surface roughness, density, and hardness confirm that different ranges of laser powers and scanning speeds are required for fabricating composite samples, as  $\text{Fe}_2\text{O}_3$  content varies in the aluminium matrix. The study carried out by Dadbakhsh et al. [33] establishes the important role of  $\text{Fe}_2\text{O}_3$  additive in expanding the processing windows and stabilising SLM processing of pure aluminium powders to scanning rates greater than 500 m/s in comparison to the outcome of Olakanmi [40] in which the highest scanning rates for good consolidation of aluminium alloy powders was 200 mm/s.

This is beneficial in the sense that higher production rates and reduced energy consumption for SLM production are achieved.

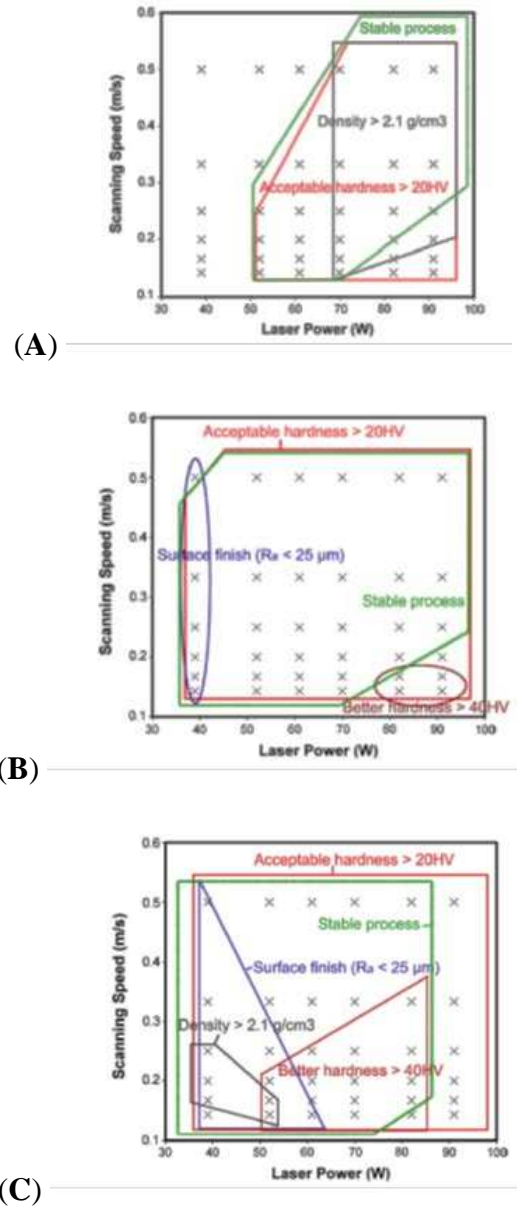


**Fig. 13.** SLM processing windows for the SLM parts fabricated from (A) Al/5wt.% Fe<sub>2</sub>O<sub>3</sub>, (B) Al/10wt.% Fe<sub>2</sub>O<sub>3</sub> and (C) Al/15wt.% Fe<sub>2</sub>O<sub>3</sub> powder mixture [33].

When developing processing maps for aluminium alloy powders with a view to fabricating multi-layer parts, there are many factors (especially powder thermal properties) that play significant roles in the determination of resultant properties of fabricated parts (see Table 2). Some of these factors will be discussed in the remaining part of this section; however these are not exhaustive, and it is expected that further issues will be uncovered as development in SLS/SLM processing of aluminium alloy powders advances. To date, only two papers cited earlier in this section addressed the development of processing maps for aluminium alloys. It is unclear at this stage, as a result of the paucity of publications concerning SLS/SLM processing maps of aluminium alloy powders if the processing issues will be applicable to other aluminium powders which have not been investigated. However, this is unlikely to occur going by the findings from Olakanmi [40] and Dadbakhsh et al. [33] where variation in the processing maps of investigated powders had been reported.

#### *4.2: Effects of SLS/SLM and Powder Properties Parameters on the Densification Mechanism*

##### *4.2.1: Effects of Laser Power, Scanning Speed, Scan Spacing, Layer Thickness, and Energy Density on Densification*

Ghosh et al. [43] investigated an in-situ multi-component reinforced aluminum based metal matrix composite, consisting of different mixtures of Al, TiO<sub>2</sub> and B<sub>4</sub>C powders, fabricated by the combination of self-propagating high-temperature synthesis and SLS processes as layer thickness, laser power, scanning speed, hatching distance or scan spacing and powder

composition were varied in an attempt to optimise for higher density, lower porosity via Taguchi design of experiments (DOE). Their results, reproduced in Fig. 14, established that the density of the specimen mainly depends upon the scan spacing, composition and layer thickness; whereas; scan spacing, layer thickness and laser power are the significant parameters which influence the porosity. Nevertheless, this outcome is contrary to Read et al. [41] who reported that laser power, scan speed, and the interaction between the scan speed and scan spacing have major influence on the porosity development in the SLM processed AlSi10Mg alloy builds. The variation in how the processing parameters influence the densification behaviour of the materials may possibly be attributed to different mechanisms of SLS/SLM arising from the chemical composition of the primary alloys and the additives. Fig. 15 shows the effect of SLS laser processing parameters on the sintered density of multiple layer parts made in AlSi12 powder as investigated by Olakanmi and co-investigators [28]. At constant laser power ( $P=240$  W), an increase in scan line spacing decreased the part's density (Fig. 15A). When scan line spacing was held constant ( $h=0.3$ mm), the sintered density reduced with increasing scan velocity or decreasing laser power (Fig. 15B). Using increasing layer thickness resulted in a lower attainable density (Fig. 15C). It was inferred that intensifying the laser energy input (increasing laser power, decreasing scan velocity, a thinner layer thickness, and overlapping of scan lines) leads to higher densification with a scan velocity of 120mm/s found to be a critical speed, above which a sound part was not obtained. Analysis of the findings by Ghosh et al. [43] and Read et al. [41] shows that the use of Taguchi design of experiments (DOE) allows a systematic planning of experiments which provides a more detailed understanding of the factors which control the SLS/SLM process in addition to

highlighting the relevant contribution of each factor to the successful consolidation of SLS/SLM processed specimens in comparison to one-by-one variable test adopted by Olakanmi et al. [28].

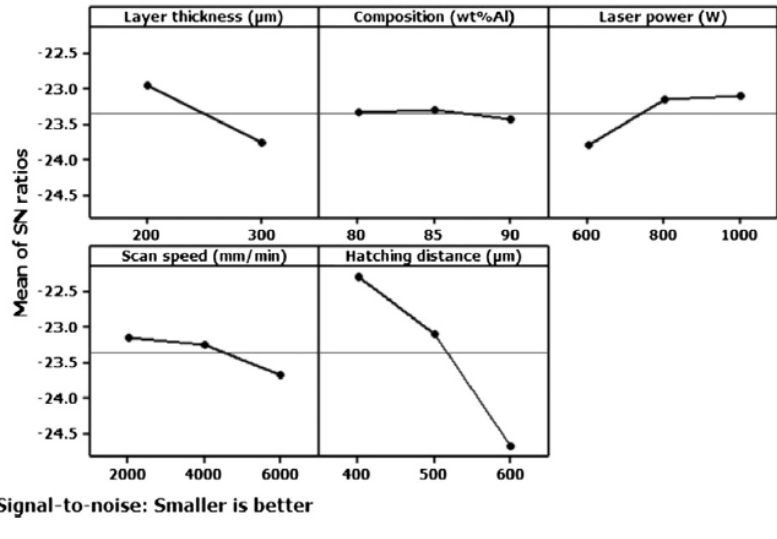
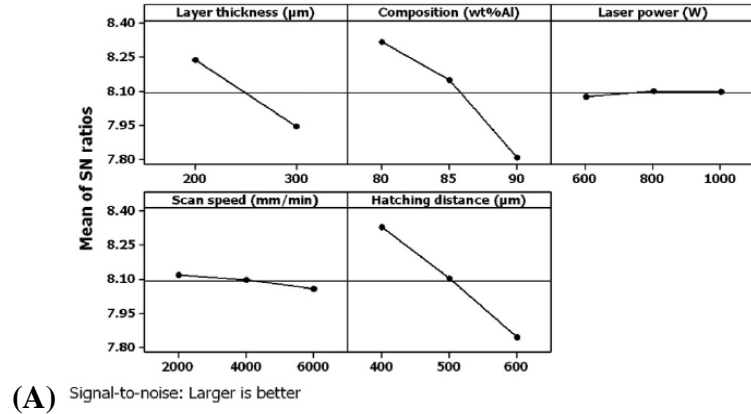


**Fig. 14.** Effect of SLS processing conditions on the density of an in-situ multi-component reinforced aluminum based metal matrix composite: (A) Main plots for density and (B) Main plots for porosity [43].

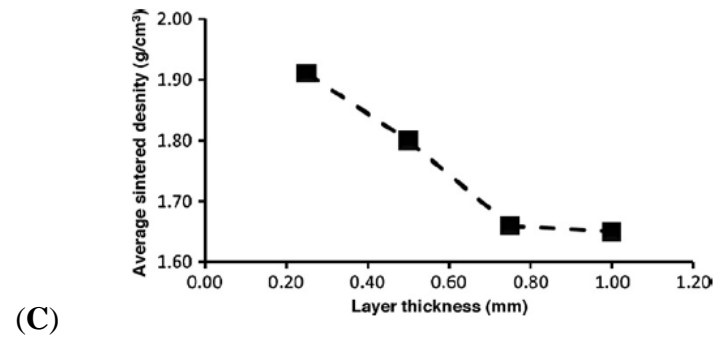
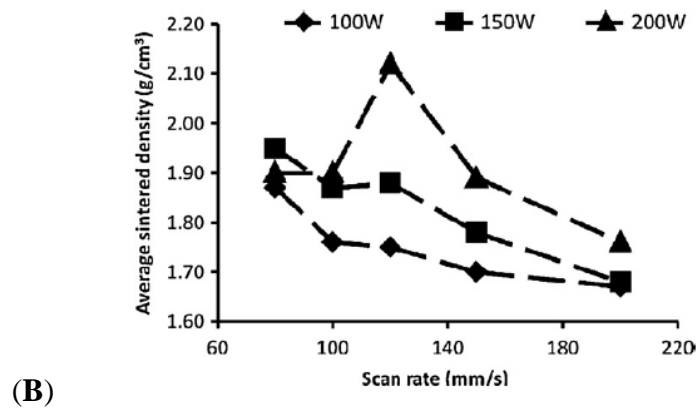
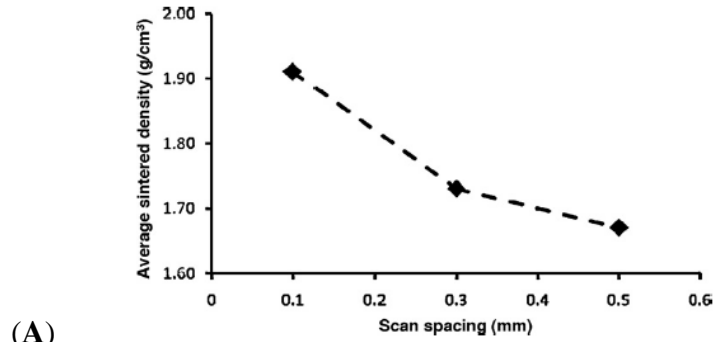
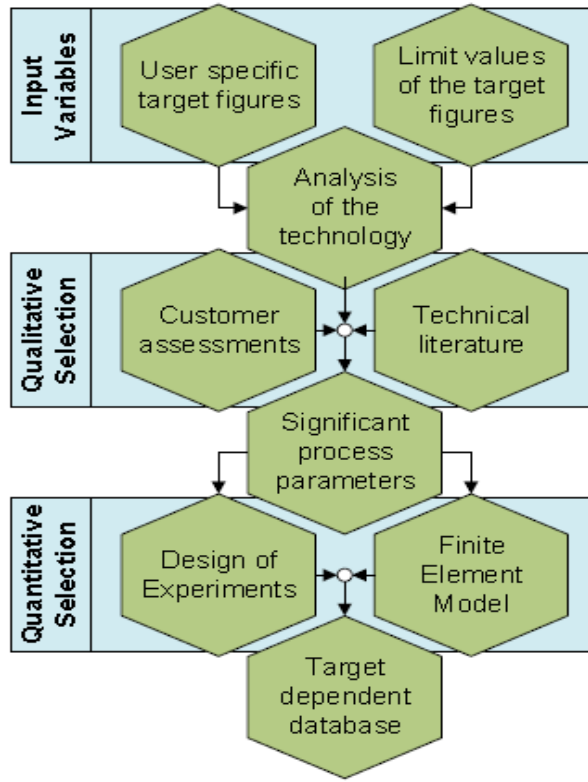


**Fig. 15.** (A) Variation of the density of SLS processed AlSi12 powder with scan spacing at fixed laser power (240 W); (B) Variation of the density of SLS processed AlSi12 powder with scanning rates at different laser powers. and layer thickness (0.25 mm); and (C) Variation of the density of SLS processed AlSi12 powder with layer thickness at fixed laser power (240 W), scanning rate (120 mm/s); scan spacing (0.1 mm) [28].

Furthermore, of much importance is the need to identify, categorise and prioritise the influencing SLS/SLM parameters and their interdependencies in order to ensure high process stability and reproducibility while reducing resource consumption and minimising uneconomic application of these processes as pointed out by Krol et al. [90] who developed procedure models (Fig. 16A) for an efficient and target figure dependent analysis of a high amount of different process parameter constellations via simulation models (Fig. 16B).

Meanwhile, the assertion by Olakanmi et al. [28] that densification is improved as the laser power increases and as the scan speed, layer thickness and scan spacing decrease is also found to be true for other materials such as Ni-Sn and Cu-Solder (Pb-Sn) [50], and Ni-alloy-Cu and Fe-Cu [91]. The implications of these findings with regard to how variation in processing parameters influences the occurrence of densification mechanism either through full melting (SLM), partial melting or binary liquid phase sintering (SLS) of metals (see Table 6) will now be considered. Similar to the P/M sintering process, it is an established fact that high temperature in SLS/SLM leads to a low contact angle and viscosity and high Marangoni flow thus improving densification [59]. Marangoni flow (Fig. 17) can be described as the initiation of thermocapillary forces for fluid flow as a consequence of the temperature gradient in the melt pool which gives rise to a corresponding differential surface tension between the edge and center of the melt pool [5, 56, 92-94]. Several researchers [5, 28, 41, 43, 56, 71, 85, 92-94] have related this fact to the volume fraction of the liquid phase formed during SLS/SLM processing as shown in the next paragraph.



(A)

Priority		Support	Scan.	Vel.	Heat.	Correlation value	
1	Support						None
2	Scan.						Very low
3	Vel.						Low
4	Heat.						Rather low
							Rather high
							High
							Very high
							Extensive

Vel.	Velocity	Scan.	Scanning strategy
Heat.	Substrate heating	Support	Support structure

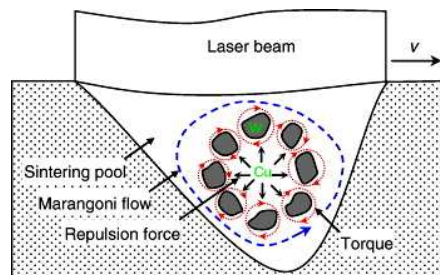
(B)

Fig. 16: (A) Procedure for a target dependent database. (B) Correlation and prioritisation matrix [90]

**Table 6**

Summary of application of SLS/SLM to metal systems.

Material	Key findings	Comments
AlSi12	Partial melting (SLS)	Partial melting indicates the choice of energy density is not sufficient to cause full densification.
High speed steels	Partial melting (SLS) incorporated with post-infiltration to achieve full densification.	Partial melting indicates the choice of energy density is not sufficient to cause full densification.
AlSi10Mg	Full melting (SLM) resulted in densification.	Applicable to single component, single material (e.g. AlSi10Mg) in which adequate energy density is supplied to the powder bed.
Ni-Sn Cu-Solder Ni-alloy-Copper Fe-Cu Bronze-nickel Al-TiO <sub>2</sub> -B <sub>4</sub> C	Binary liquid phase SLS employing high and low melting point materials to attain densification. Low melting point materials melt and bind the particles of the high melting point materials together.	Applicable to two-component material system having different melting points.  Fractograph suggests that bronze melts and wets the nickel particles which do not exhibit any melt.



**Fig. 17.** A schematic illustration of Marangoni flow as applied to the direct SLS of W-Cu 2-phase direct SLS [93].

It was noted that at processing parameters combining low scan speed and relatively low laser power, the resultant input energy is insufficient to generate adequate liquid phase that binds the particles together. Therefore, the outcome is partial melting (SLS) resulting in poor densification. As the laser power increases at low scan rates, the increasing incident laser energy increases the temperature of the powder bed thereby causing a significant amount of powder's inter-particulate melting as a consequence of the occurrence of adequate liquid phase. This condition culminates in higher densification due to the instability of the liquid cylinder which occurs as the surface free energy is minimised. Therefore, it can be inferred that appropriate increments in the laser energy input leads to high working temperature which eventually reduces both melt viscosity and surface tensions. Furthermore, at high temperature, the material transport during the laser sintering process is enhanced as a consequence of the formation of connective streams within the molten pool during SLS. This results in the reduction of the amount and sizes of inter-agglomerate pores, thereby obtaining fully dense parts.

Moreover, the wetting characteristics and the attendant forces for rearranging solid particles in the liquid phase increase as the amount of liquid phase increases provided the energy density increases appropriately. The implication of this finding as pointed out by Olakanmi et al. [28] is that there exists an optimal laser energy density combining relative high laser power with low scan speed, at which the solid-liquid wettability is most successful, such that the structural particles in the liquid are most suitably re-arranged with a view to achieving higher sintered density (Fig. 18). Further increment in laser energy density leads to reduced sintered density. In this condition, the higher laser power generates increased quantity of liquid phase, but the

reduced scan speed causes substantial increment in its lifetime, thereby promoting spheroidisation and breakdown in the melt pool. The reduced sintered density in this case is attributed to significant aggregation of the structural particles.

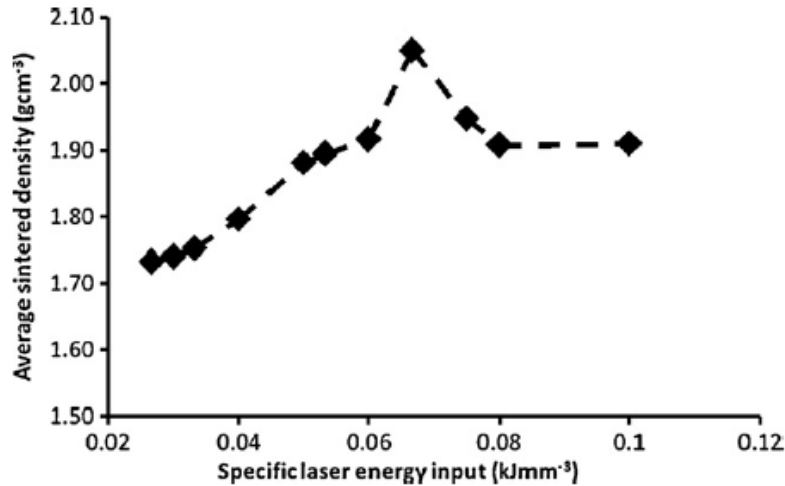


**Fig 18.** Variation of the density of SLS processed AlSi12 powder with the applied energy density. Processing conditions: laser power (100–200 W), scan rate (80–200mms<sup>-1</sup>), scan spacing 0.1–0.3mm, and layer thickness 0.25–1.00mm [28].

Successful SLM processing of metals demands that an appropriate layer thickness is established for the other processing parameters which are employed. For instance, if the powder layer thickness is very high, complete melt down of particles will be impossible to achieve due to insufficient laser energy penetration into the powder bed. Consequently, large and interconnected pores are formed in the sintered structure which reduces the density of the SLM fabricated sample. During laser processing of AlSi12, Olakanmi and co-investigators [28] discovered that

there exists a critical value for layer thickness at which most of the gas bubbles in the powder bed are able to move up to the layer's surface, and collapse when the molten liquid solidifies rapidly to form finer grains and produces a pore-free sintered part. This pore-free sintered sample obtained at the critical value of layer thickness was noted to possess excellent microstructural properties because the re-melting of the previously sintered layer was possible, thereby enabling the formation of coherently bonded layers with lesser degree of spheroidisation (see Fig. 19).

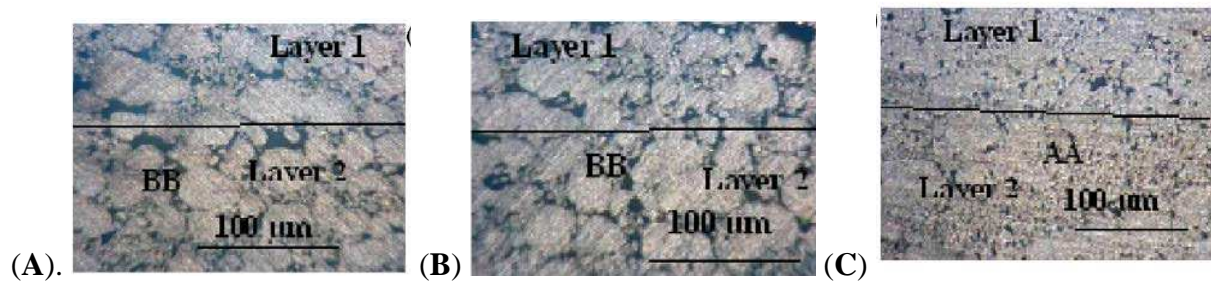


**Fig. 19.** Effect of variation in layer thickness on the microstructure of laser sintered AlSi12 powder at laser power of 200 W, scan rates of 120 mm/s; and scan spacing of 0.1mm: (A) 1.0mm, (B) 0.5mm and (C) 0.25mm [28].

It has also been proved that where re-melting of the substrate occurs, spheroidisation does not take place if there is wetting of the as-solidified material by the melt pool [46, 95, 96]. According to Agarwala et al. [50], the minimum possible layer thickness at which a pore-free structure is obtainable is determined by the maximum particle size of the powder deposited on the bed as well as the precision of the powder delivery mechanism employed in the sintering machine. Olakanmi and co-investigators [28] established that lowering the layer thickness below the minimal permissible layer thickness for a powder system would create complications in

spreading homogeneous layers of fresh powders with the previously laid layers being displaced and the surface roughness of the sintered samples exacerbated. This consequently hinders inter-particulate bonding or melting.

Furthermore, it must be emphasised that the most significant parameter SLS/SLM parameter influencing the densification of parts is the laser energy density which is defined by the relationship shown in Eq. (2). This shows that the energy density for the SLS/SLM process increases with increasing laser power, and decreasing scanning rates, scan spacing and layer thickness.

$$\psi = P/uhd \quad (2)$$

where  $\psi$  = Specific laser energy input ( $J/mm^3$ );  $P$  = Power (W);  $u$  = Scanning rates (mm/s);  $h$  = scan spacing (mm);  $d$  = layer thickness (mm).

Simchi & Pohl [94] and Sanz-Guerrero & Ramos-Grez [97] established that the resultant fractional sintered density of SLS/SLM processed parts is in direct relationship with the specific laser energy input incident on a powder bed. They pointed out that the fractional density,  $\rho$ , of these powders is an exponential function of the specific laser energy input ( $\psi$ ) as shown in Eq. (3).

$$\rho = C_1 - C_2 \exp(-K\psi) \quad 3$$

where  $C_1$ ,  $C_2$  and  $K$  (densification co-efficient) are material constants of the specific powders under investigation.

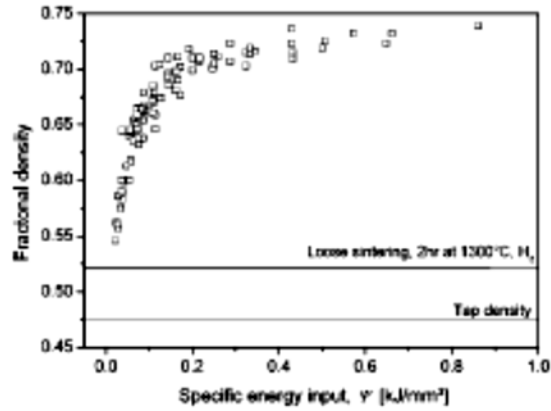


**Fig. 20.** Fractional density vs. the specific energy input ( $\psi$ ) for sintered iron using different processing parameters [94].

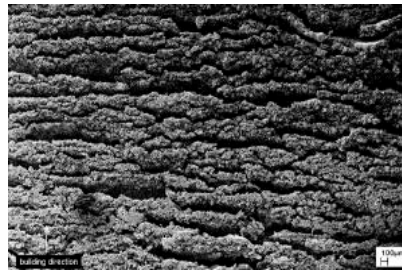


**Fig. 21.** SEM image of SLS/SLM processed iron powder at the excessive delivery of specific laser energy input of 0.8 kJ/mm<sup>3</sup> showing the occurrence of layer delamination as a result of increased life time of the generated liquid phase [94].

Fig. 20 illustrates that the fractional density increases with the specific laser energy input, for an iron powder, up to a maximum of 0.74 at the saturation specific laser energy input and at  $\psi = 0$ , the density approaches the tap density of the powder material [94]. Moreover, when the

experiment data were fitted according to Eq. (3),  $C_1=0.719$ ,  $C_2=0.214$ , and  $K=14.82$  at a  $\psi < 0.8$   $\text{kJ mm}^{-3}$ . Beyond the saturation specific laser energy input of  $0.8 \text{ kJ mm}^{-3}$ , the maximum fractional density remained constant irrespective of the amount of specific laser energy incident on the powder bed. Observations from Fig. 20 and 21 imply that excessive delivery of the energy density at very high laser power and low scan rates (i.e. above the saturation specific laser energy input) will result in complications such as balling and layer delamination due to increased life time of the generated liquid phase as noted earlier on in this section.

In summary, at low scan speed, small scan spacing, and relatively high laser power, the amount of liquid phase generated is higher and sintering time is longer, thereby promoting higher densification. Meanwhile, at a low volume fraction of liquid and short sintering time obtainable by using a high scan speed and scan spacing and low values of laser power, the liquid phase is not enough or has not sufficient time to enhance wettability. There appears to be a maximum sintered density which may be achieved in SLS/SLM at a critical value of the specific laser energy input. Above this critical value, it is unable to increase densification further because the increased lifetime of the liquid phase promotes the balling phenomenon which inhibits densification. The only exception is when substrate wetting occurs. The effect of the scanning strategy on the processing and quality characteristics of SLS/SLM processed parts will be considered in the next section.

#### *4.2.2: Effects of Laser Scanning Strategy on the Densification Mechanism*

Porosity, residual stresses, and cracking as a consequence of hot shortness, and poor surface finish are among the problems associated with the SLS/SLM process as a result of the generation of uneven thermal gradients in the parts [42, 56, 98-102]. To control the thermal gradient during powder heating and cooling and thereby fabricated unwarped and uncracked layers, various studies [42, 56, 98-102] have investigated the relationship between scanning strategies and the properties of SLS/SLM processed parts. For instance, Dewidar et al. [56] identified standard, diagonal and perimeter scanning strategies (Fig. 22) for producing single layers whereas Su et al. [98] tested the influence of four types of scanning patterns (Fig. 23) and various scan spacings on the building of overlapped beads of laser sintered specimens. Although Dewidar et al. [56] discovered that perimeter scan approach was less successful while the standard and the diagonal scan strategies gave very similar results for parts fabricated by direct SLS, Su and co-investigators concluded that the adoption of different scanning patterns culminated in different processing times which affected the nature of the microstructure obtained for the laser sintered parts. Hauser et al. [99] reported on the scanning routines for successful small scale direct SLS processing of parts at room temperature. It was established that the single layer shape affects warping but the heights of test samples do not.

In order to avoid non-uniform distribution of energy input in SLM processed parts, Su & Yang [101] identified three types of overlapping regime namely: intra-layer overlapping regime, inter-layer overlapping regime and mixed overlapping regime with coexistence of the first two types (Fig. 24).

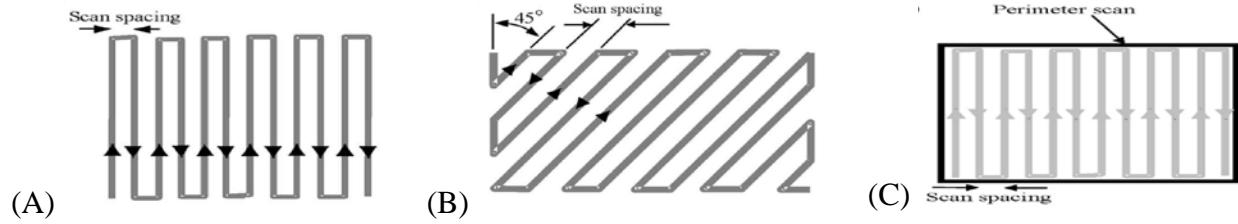


**Fig. 22.** SLS/SLM scanning strategies (A) Standard (B) Diagonal and (C) Perimeter [56].

	 ↓ ↓ ↓ ↓ ↓ 1 2 3 4 5 Pattern 1	 ↑ ↑ ↑ ↑ ↑ 1 2 3 4 5 Pattern 2	 ↓ ↓ ↓ ↓ ↓ 1 4 2 5 3 Pattern 3	 ↑ ↑ ↑ ↑ ↑ 1 4 2 5 3 Pattern 4
Travel time		minimum	maximum	

**Fig. 23.** Four different scanning strategies adopted in the direct laser sintering of tool steels using a Nd: YAG laser machine. The numbers indicate the scanning sequence while the arrows represent the scanning directions [98].

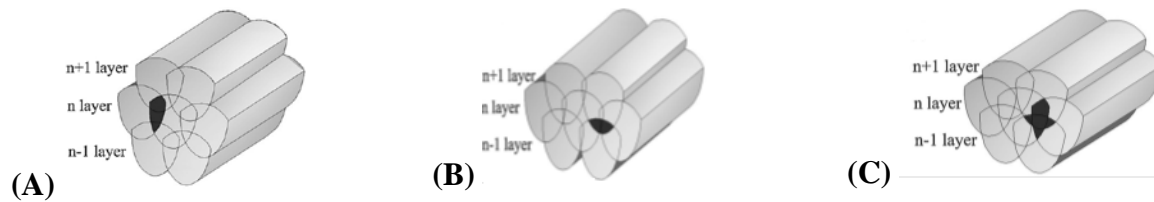


**Fig. 24.** Three types of overlapping regime under inter-layer stagger scanning strategy. (A) Intra-layer overlapping regime. (B) Inter-layer overlapping regime. (C) Mixed overlapping regime [101].

Their study establishes that inter-layer overlapping regime could be obtained when the track space was smaller than 0.2 mm, which produced a resultant with high relative density at the specified process parameters. Meanwhile, Su & Yang [101] noted that their study was about track space without consideration of other process parameters, such as laser power, hence, further study including other factors is expected to reveal more understanding of the track overlapping regime during SLM process. Moreover, Kruth et al. [103] discussed how the temperature gradient induced internal stresses are dependent on the part geometry and the scan strategy being adopted. They observed that if the area to be scanned is small, a short scan length normally occurs thereby leaving little time for the surface to cool before the next track is scanned, thus resulting in high temperature. For larger areas, the laser beam travels a longer distance so that successively scanned tracks have more time to cool down resulting in a lower temperature over the scanned area. The consequent lower temperature of the scanned area results in poor wetting conditions causing reduction in the material density because of larger heat sink between the loose powder and the solidified material.

Furthermore, Aboulkhair et al. [102] clarified how the design of the scanning strategy minimises porosity and amends defects in AlSi10Mg parts processed via SLM by considering the following scanning patterns: X (a unidirectional scan with a single scan per layer), 2X (similar to “X” but each layer is scanned twice), alternating (scanning each layer in a direction rotated by 90° to its precursor), X&Y 2HS (each layer was scanned twice having each scan perpendicular to the one before and with different hatch spacings for each scan), pre-sinter (first scan the layer with half the power followed by a second scan with full power), and overlap (each

layer was scanned twice with the second scan melting the overlap between each two adjacent melt pools).

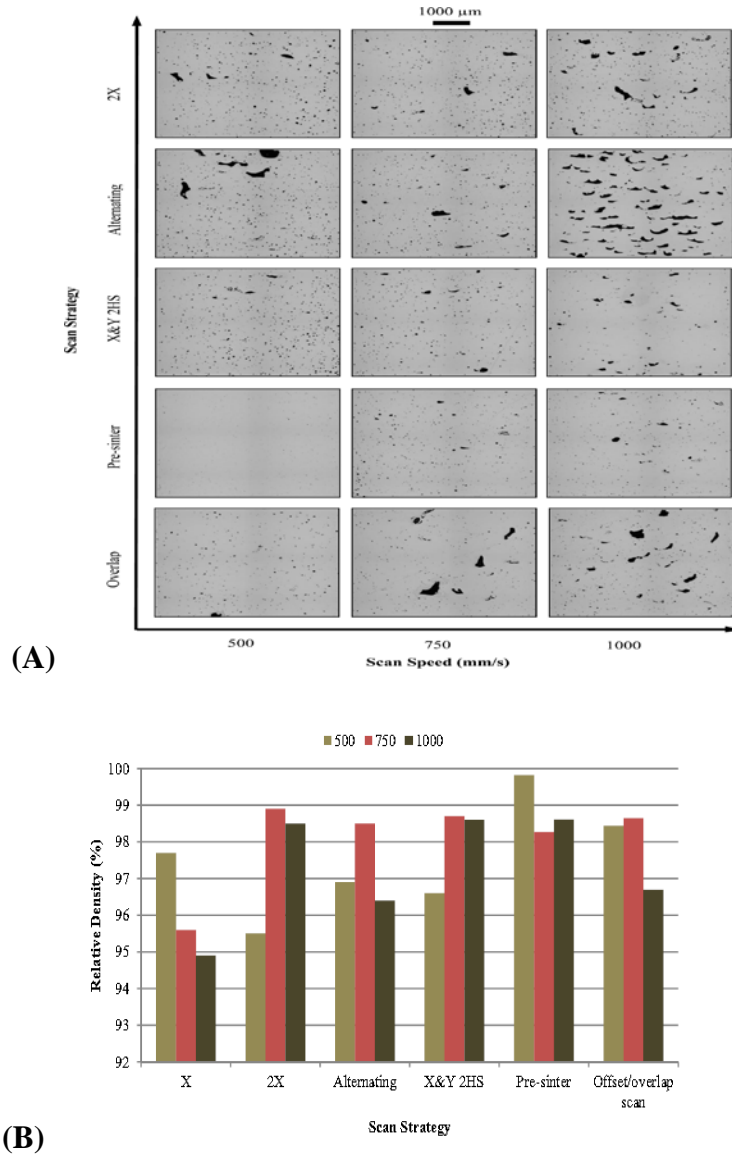


**Fig. 25.** (A) Porosity evolution in AlSi10Mg samples processed using different combinations of scan speeds and scan strategies, (B) Influence of scanning strategy on relative density [102].

They revealed that at a scanning speed of 500 mm/s, scanning each layer twice was effective in reducing the keyhole pores but pores still existed when scanning the layer once in alternating scan while the overlap scan reduced but could not eliminate the keyhole pores (Fig. 25A). In regards to the double scan per layer ( 2X, X&Y 2HS, pre-sinter, or overlap) the keyhole pores were significantly reduced even if not eliminated at all scanning speeds. Meanwhile, at slower scanning speeds, the dissipation of excessive energy resulted in extensive formation of metallurgical pores in SLM processed AlSi10Mg parts even though the keyhole pores were eliminated. In addition, employing double scans at scanning speeds of 500 and 1000 mm/s ensured that the the metallurgical pores were not significant as a result of lower energy density (Fig. 25A). Fig. 25B depicting the relative density of various SLM processed samples agrees with Fig. 25A thereby confirming that a relative density of 99.8% can be achieved using a double unidirectional scan with different laser powers for the two scans (pre-sinter) at the same speed. Hence, the work of Aboulkhair et al. [102] shows that achieving a near fully consolidated part using SLM requires the employment of compromise between the different parameters and scan strategies.

Similar to the outcomes from the study carried out by Li et al. [42] on the SLM processing of  $\text{Al}_{85}\text{Ni}_5\text{Y}_6\text{Co}_2\text{Fe}_2$  bulk metallic glass composites, the authors also observed that double or multiple scanning of the build area on the powder bed was useful during SLS/SLM processing of aluminium alloy powders. This approach was adopted in instances when the dissipated laser energy density was not adequate to consolidate the aluminium parts, thereby necessitating an alteration in scan count. However, if the applied laser energy density is more than necessary, this

results in heat transfer to the powder bed, thereby melting neighbouring particles in addition to those being targeted. This usually results in accumulation of stress and distortion of parts. This challenge may be overcome by reducing the laser power when scanning each layer twice before re-coating with a new layer of powders [42]. This procedure ensures more energy diffuses into the particles consequent upon increased laser-material interaction attained at lower scanning speed rather than high laser power. This approach effectively minimises dimensional inaccuracies in the SLS/SLM parts.

#### *4.2.3: Effects of SLS/SLM Atmospheres on the Densification Mechanism*

During the SLS/SLM of metal powders, the presence of oxygen in the operating atmosphere and as a form of passive layer of oxide on the powder surfaces does exacerbate the balling phenomenon due to the initiation of Marangoni convection. The major concerns arising from this are the significantly high absorption of laser energy on the sintering/melt pool and the liquid-metal surface tension which increases the wetting angle between the solid and liquid phases that can inhibit inter-particulate bonding/melting between rastered lines and individual layers [38, 105]. Therefore, the use of controlled atmosphere during SLS/SLM processing of aluminium alloys is very important because it prevents undesirable reactions, sweeps deleterious reaction products from the sintering chamber, initiates desirable reactions as demonstrated in the use of nitrogen atmosphere to form AlN (aluminium nitride) which improves the dimensional stability of sintered aluminium parts, and reduces oxide present on the metal surfaces as exemplified in iron through dissociated ammonia [106].

From the available literature, very limited experimental evidence could be gathered on the effect of sintering atmosphere on the density of materials fabricated via SLS/SLM. Wu et al. [107] assessed the effect of the oxygen content on the microstructure of the burn-resistant alloys, Ti-25V-15Cr-2Al-0.2C (wt%), processed in air; using the argon carrier as protection, and in a glove box with an argon atmosphere with  $O_2 < 5\text{ppm}$ . They discovered that the microstructures obtained differed for each atmosphere with the alloy laser processed in air characterised by large titanium carbide dendrites while the carbides obtained in the argon processed atmosphere had finer and more uniformly distributed carbides. While Wu and co-investigators discovered that the atmosphere influences the microstructure obtained, they were not able to propose a mechanism responsible for this effect. Moreover, Das et al. [108] evaluated the effect of a wider range of atmospheres (rough vacuum of the order of 30mtorr, rough vacuum purged with argon, high vacuum  $< 5 \times 10^{-5}$  torr, and high vacuum followed by argon-2% hydrogen backfill) on the fabrication of superalloy cermet abrasive turbine blade tips via the direct SLS process. Their results revealed that both rough vacuum and the purged argon contained sufficient oxygen to oxidize the molten superalloy matrix thereby causing balling, separation, and tearing due to surface tension effects. They concluded that a high vacuum atmosphere resulted in relatively uniform surface features, with no cracking, tearing, or separation when the investigation was conducted within an acceptable window of processing parameters. Meanwhile, only a study has detailed the effect of atmosphere on the densification of SLS/SLM of aluminium alloys as seen in Wang et al. [38] who investigated the role of argon, nitrogen and helium sintering atmospheres on the laser melting of Al12Si alloy powder. Their findings showed that laser melting under these atmospheres had no significant effect on densification as seen in Figure 26.

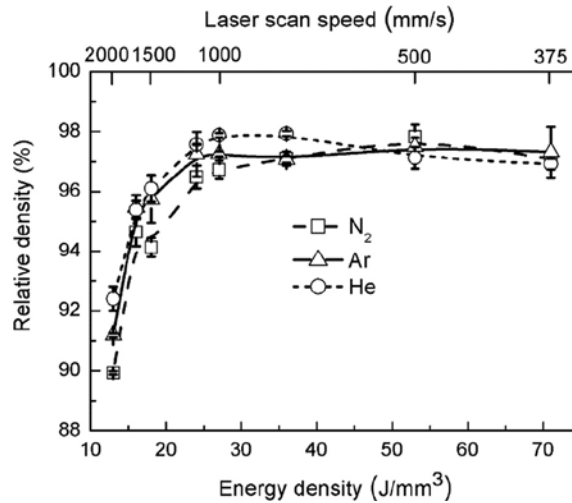


**Fig. 26.** Relative density of the SLM-produced Al-12Si samples in various atmospheres as a function of incident laser energy [38].

However, the outcome from Wang et al. Wang et al. [38] contradicts the findings from the studies carried out by Asgharzadeh & Simchi [6] and Simchi & Pohl [94] who reported that laser sintering of metal powders under argon atmospheres yielded better densification in comparison to nitrogen atmospheres especially at higher scan rates. The reported contradiction about the effects of processing atmospheres on the densification of SLM/SLS processed metal powders might have been possibly engineered by different mechanisms of chemical reactions occurring during laser processing of different materials. The exact nature of the chemical reactions and the associated mechanisms for various metallic powders need to be explored further in future studies. All the literature reviewed in this section so far are in concurrence with the observation made by Hauser et al [105] that the amount of oxygen present during heating, melting and fusing

of metal powder strongly inhibits the effectiveness of laser power and scanning rates for successful SLS processing.

Since there is paucity of literature detailing the exact nature of chemical reactions and its associated mechanisms during SLS/SLM of aluminium alloys in processing atmospheres, it would seem, on the other hand, instructive to examine the effect of atmosphere on the sintering response of aluminium and its alloys in the powder metallurgy route. Schaffer et al. [106] carried out an extensive literature survey on the effect of atmosphere on the sintering of aluminium and its alloys. They identified nitrogen, vacuum, argon and hydrogen gases as atmospheres that had been utilised for the conventional sintering of aluminium and its alloys. The outcome of their review suggested the effects were quite complex. For instance, Martin & Castro [109] found that nitrogen was more effective than vacuum for an Al-1Mg-0.5Si-0.2Cu (wt%) alloy while an improved sintering response was obtained for Al-4.5Cu-0.5Mg-0.2Si (wt%) alloy under vacuum. They pointed out that the differences noted in the sintering responses of the alloys under the two atmospheres under consideration were a result of varying cooling rates after sintering. It is worth noting that Martin & Castro [109] had not investigated the effect of the varying chemical composition of the alloys independently of the sintering atmospheres. Schaffer & Hall [110] discovered that sintering of aluminium alloys under nitrogen resulted in the beneficial formation of aluminium nitride.

Other researchers have also presented evidence that sintering of aluminium alloys under nitrogen yielded aluminium nitride, which possibly promoted the disruption of the surface oxide film and facilitated diffusional processes as a consequence of the greater degree of stability of  $\text{Al}_4\text{N}_3$  than  $\text{Al}_2\text{O}_3$  [106]. The available literature presents, however, contradictory findings regarding the role of hydrogen in the sintering of aluminium and its alloys. While some investigators have claimed that hydrogen has little influence on the sintering of aluminium and alloys, others have shown that it has a deleterious effect on its sinterability with the explanation that water vapour associated with hydrogen acts as a stabiliser of hydrated alumina thus inhibiting shrinkage [106]. While no convincing inference could be drawn from the available literature on the effect of atmosphere on the sintering response of aluminium and its alloys, Schaffer and co-workers noted that anecdotal evidence from the industry indicates that nitrogen is always the preferred atmosphere for the sintering of aluminium and its alloys because of its low cost. Schaffer and co-investigators [106] examined the sintering of aluminium alloys of varying compositions in vacuum, argon, wet and dry nitrogen, nitrogen-5%hydrogen and argon-5%hydrogen mixtures and proffered explanations as to why moisture is deleterious and the formation of aluminium nitride is essential. Fig. 27 presents the results of this investigation. The solid line represents no change in density between the green and sintered state. Hence, points above and below the line confirm the occurrence of net shrinkage and net expansion of the sintered parts respectively. It can be seen that shrinkage only occurs for all green densities under nitrogen atmosphere, whereas volumetric expansion of sintered parts occurred when 5%  $\text{H}_2$  was added to either a nitrogen or argon atmosphere.

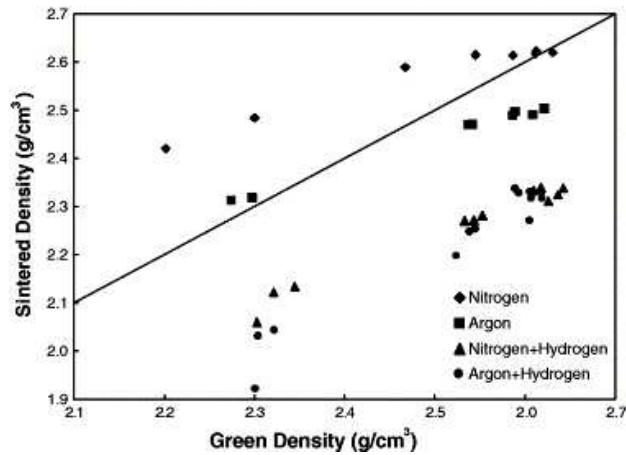


**Fig. 27.** The effect of the sintering gas on sintered density for Al-3.8Cu-1Mg-0.7Si (wt%) samples were sintered for 1 h and air cooled [106].

Therefore, Schaffer et al. [106] showed that dry nitrogen is the most efficacious atmosphere for the sintering of aluminium alloys while hydrogen (moisture) is extremely prejudicial to sintered density. It was explained that aluminium nitride formation was beneficial in the reduction of the pressure in the pore spaces thereby inducing pore filling at particle sizes that are smaller than those required for the sintering in inert atmospheres. Since the processing conditions of conventional powder metallurgy sintering differ from that of the direct selective laser sintering, it will be good to explore whether changing from argon to nitrogen atmosphere enhances the sinterability of aluminium alloys other than AlSi12 powder in SLS/SLM.

### *4.3: Effects of Powder Properties on the SLS Densification Mechanism*

In SLM, the effect of powder particle size and distribution is considered to be of no importance because all particles undergo melting. Similar to the observation of German [111, 112] for the P/M sintering process; chemical composition, particle shape, surface morphology, and the particle size distribution are among the factors that have tremendous influence on the SLS response of metallic powders. From the available literature, mean particle sizes of the bulk metallic powders that have been used in various SLS experiments vary from 0.6  $\mu\text{m}$  up to 400  $\mu\text{m}$  and are more often produced by gas atomisation methods. This manufacturing technique yields spherical shaped particles with smooth surfaces and, when inert gases are employed, the powder often has low levels of residual oxygen and surface oxidation [113]. These characteristics provide for ideal flow properties and reduced surface contamination which are the main causes for concern during the selection of powder for SLS. Previous investigations on laser sintered powder have dwelt mainly on the influence of processing parameters on the functional properties of sintered material. Very few research groups have addressed the issue of the role of powder particle size and shape on the sintering behaviour. Consequently, to gain an insight into this, it is necessary once again to consult the P/M literature, this time to explain the effect of particle shape, size and distribution on the sintering response of various powders via the conventional powder metallurgy route.

#### *4.3.1. Effects of Particle Size and Distribution on the SLS Densification Mechanism*

In a system having substantial solid solubility of the additive in the base metal and/or exhibiting preferential diffusive flow from the additive to the base metal during P/M sintering, Lumley & Schaffer [114] found that the use of fine additive powders resulted in a greatly reduced quantity of liquid phase formed whereas coarse powders increased the amount of liquid phase that formed and prolonged its existence. They concluded that where there is no mutual solid solubility, particle size is unimportant in liquid development for improving the densification mechanisms of parts. Although, Lumley & Schaffer [114] did not consider the effect of particles sizes and size distribution on the thermal conductivity of a packed powder since this is unlikely to be a significant factor in P/M sintering; however; this is an important consideration in SLS because it influences the amount of liquid formation in the laser sintered part. Lumley & Schaffer [115] also explored the nature of the influence of the additive particle sizes on the properties of sintered aluminium-copper alloys by demonstrating that bulk density and pore sizes might not be accurate indicators of the strength of sintered parts. They established that particles of intermediate size sintered at slow heating rates and fine particles sintered at fast heating rates with the resultant formation of an extensive, well distributed liquid phase, from which a well sintered matrix develops.

In order to improve the packing density of the powder bed during SLS, it is necessary to blend together powders of different particle size distributions. It is clear, however, that the introduction of fine particles to a powder can be influential in increasing its sintering response. Furthermore, while the introduction of smaller particles into the interstices of larger particles

which also increases packing density could lead to enhancement of the sintering process, it must be noted that the addition of smaller particles could result in the formation of defects in the SLS processed samples. This could be ascribed to the sintering stress encountered by the small particles which is much higher than that experienced by the larger particles. This means the larger particles are able to constrain the shrinkage of the smaller particles, thus resulting in circumferential cracking defects around large particles [112, 116].

Powder particle size and size distribution play a key role in the SLS densification mechanism given that chemical composition has a significant effect on the propensity of the resulting alloy to densify, and an appropriate component ratio of the powder blend is needed for a range of particle sizes, shapes, and surface morphology as demonstrated by Olakanmi et al. [29] in the laser sintering of blended Al-Si powders. Theoretically, there ought to exist a relationship between the sintered properties and the particle size distribution of a candidate powder for the SLS process. A comparison of the SLS process with the conventional P/M sintering process, suggests the following features of such a relationship: (1) smaller sized powder particles tend to sinter more quickly since the sintering stress is inversely related to particle diameter; (2) powder particle densification should take place through neck formation at points of contact between particles. The consequence of this is that with a higher packing density of similarly sized particles in a powder, the tendency should be for a faster sintering rate to be obtained [29].

Simchi [117] investigated the effect of powder particle size on the densification of SLS processed metal powder. It was discovered that the maximum attainable sintered density (saturation density), which was obtained at the optimal specific laser energy input, was for a mean particle size of 29.2  $\mu\text{m}$  (Fig. 28A and B). It was then pointed out that fine powder with a narrow particle size distribution tended to agglomerate, whereas coarse powders with broad particle size distribution tended to segregate: reduced sintered density obtained in both cases. Furthermore, a material-dependent factor,  $K$ , (Fig. 29A and B) was defined using Eq. (3) and employed by Simchi in an attempt to explore the influence of particle sizes and oxygen content of the powders upon densification. It was established that this material-dependent factor  $K$  increases as the densification kinetics of the powders become poorer thereby confirming that the particle size of 29.2  $\mu\text{m}$  is the most desirable for the chosen SLS process condition.

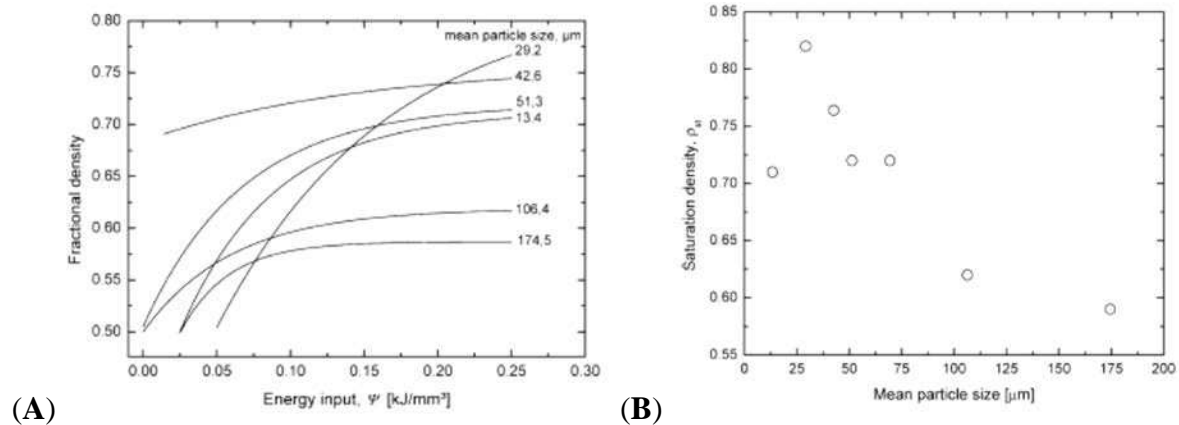


**Fig. 28.** The variation of (A) fractional density with specific energy input ( $\psi$ ) for iron powders of varying particle sizes; (B) saturation density with the mean particle sizes of iron powders [117].

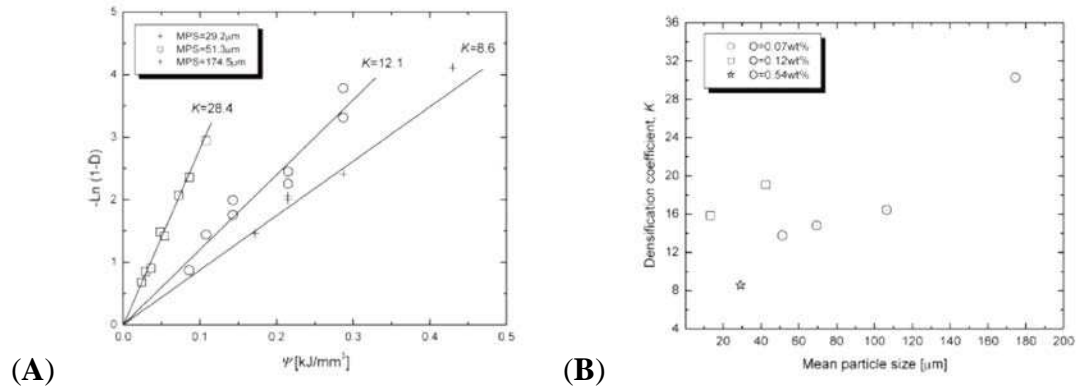


**Fig. 29.** The variation of (A) the densification (D) with the specific energy input ( $\psi$ ) for iron powders of different particle sizes; (B) the densification co-efficient (K) with the mean particle size of iron powders at different oxygen concentrations [117].

#### 4.3.2 Effect of Particle Shape on the Densification Mechanism

Liu et al. [69] discovered that particle size and size distribution, the tap density, the oxide film thickness, the surface chemistry, and impurity concentration had little effect on the P/M sintering behaviour of aluminium powders whereas particle shape was noted to have contributed significantly to differences in densification mechanism. They suggested that the differential thermal expansion between the aluminium particle and its oxide film might have caused the oxide to fracture and that the fracture characteristics are different for spherical and irregular particle shapes. Niu & Chang [83] explored the differences in the sintering response of both angular, water atomised and spherical, gas atomised powders. Their findings showed that SLS of gas atomised powder yielded a homogeneous, dense single layer. Agglomerates and inter-agglomerate pores were obtained for water atomised powders which were believed to be caused

by a combination of irregular shape and high oxygen content in the powder particles. Furthermore, Olakanmi [40] explored the role of powder properties (alloying element, oxidic constitution, and particle shape) in the densification kinetics of pure and pre-alloyed aluminium powders selectively laser melted (SLM) at an energy density of  $75 \text{ J/mm}^3$ . The densification kinetics of the powders was found to be primarily controlled by their oxide constitution (which is dependent on the alloying element) and partially dependent on the powder bed density and particle shape. However, Olakanmi et al. [29] established that powder properties such as apparent and tapping densities which determine the nature of heat transfer influencing the densification process on a powder bed could be controlled in blended bimodal and trimodal aluminium powders having different particle size and distribution, and particle shape in varying proportions. The outcome of the study revealed that blending of powders having appropriate particle size distribution, correct component ratios, and spherically shaped particles rather than irregular particles led to improvement in the thermal conductivity of the powder bed which consequently increased the sintered density of SLS processed parts (Fig. 30). It may be inferred that the exact influence of powder's particle shape on the densification mechanism of SLS processed parts is still ambiguous. Meanwhile, further studies clarifying the amount as well as the nature of contribution of the particle shape to the densification behaviour of SLS processed parts need to be carried out.

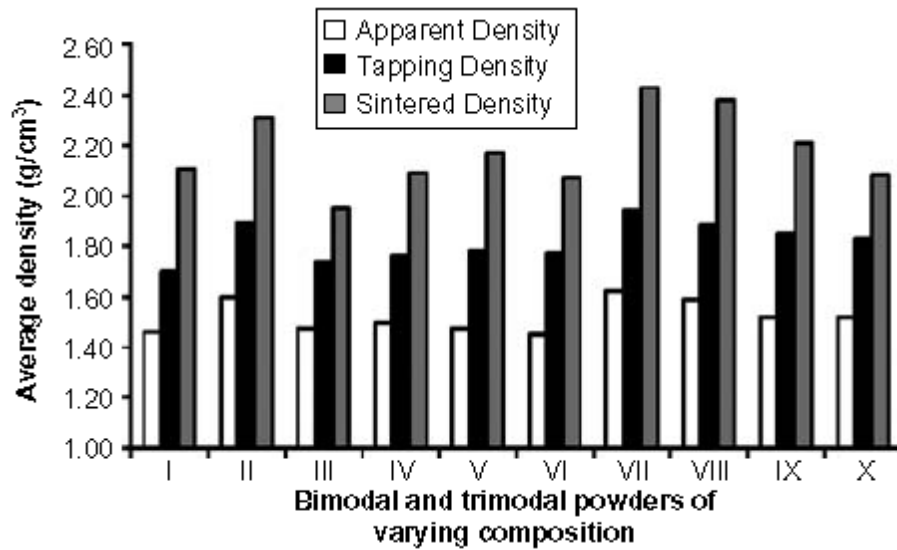


**Fig. 30.** Comparison of the apparent, tapping, and sintered densities (laser power of 200W, scan speed of 65 mm/s, layer thickness of 0.25 mm, and a scan spacing of 0.1 mm) of bimodal with trimodal powders [29].

#### 4.3.3 Effect of Alloying Elements and Oxide Constitution on the Densification Mechanism

Zhang et al. [118] investigated the nature of influence of nickel addition on the densification behaviour of SLM processed tungsten powder blended with 10 wt.%, 20wt.% and 40 wt. % nickel. The outcome of the study revealed that nickel addition enhanced the densification of SLM processed tungsten-nickel (W-Ni) parts and consequently reduced its viscosity via a combination of liquid phase sintering (LPS) and partial melting of W particles. Simchi [119] also explored the densification kinetics of SLS processed Fe, Fe-C, Fe-Cu, Fe-C-Cu-P, 316L stainless steel, and M2 high-speed powders. When the empirical sintering rate data was related to the energy input of the laser beam according to the first order kinetics equation in

order to establish a simple sintering model, it was established that the “densification coefficient K”; a material dependent parameter varied with the chemical composition, and oxygen content of the powder material (Fig. 31).

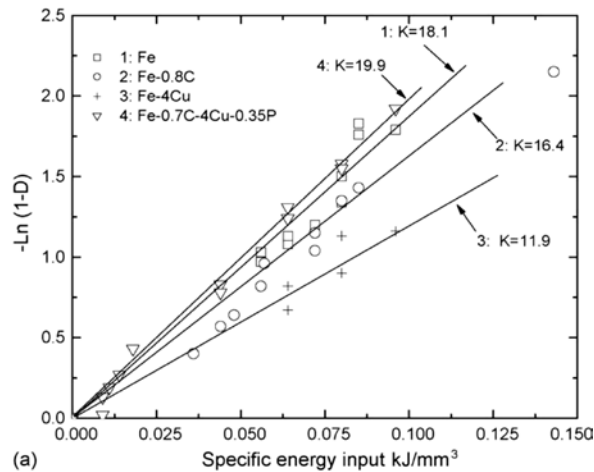


**Fig. 31.** The variation of the densification (D) with the specific energy input ( $\psi$ ) for iron-based powders of varying chemical composition under the same processing conditions [119].

Dadbakhsh & Hao [31] investigated the effects of various Al alloys (including pure Al, AlMg1SiCu, and AlSi10Mg), mixed with 15 wt% Fe<sub>2</sub>O<sub>3</sub>, on the selective laser melting (SLM) facilitated *in-situ* reaction and formation of Al metal matrix composite (MMC) components. Their findings showed that alloy composition directly influenced the SLM consolidation performance: with AlSi10Mg showing the best performance while AlMg1SiCu was more comparable to pure Al due to its lower content of alloying elements (Fig. 32). Moreover, inter-solid regions in AlMg1SiCu derived SLM part appeared comparable to that in pure Al derived

part, while AlSi10Mg improved the density and mitigated inter-solid porosity as a result of lower thermal conductivity and better SLM consolidation and oxide layers breakdown.

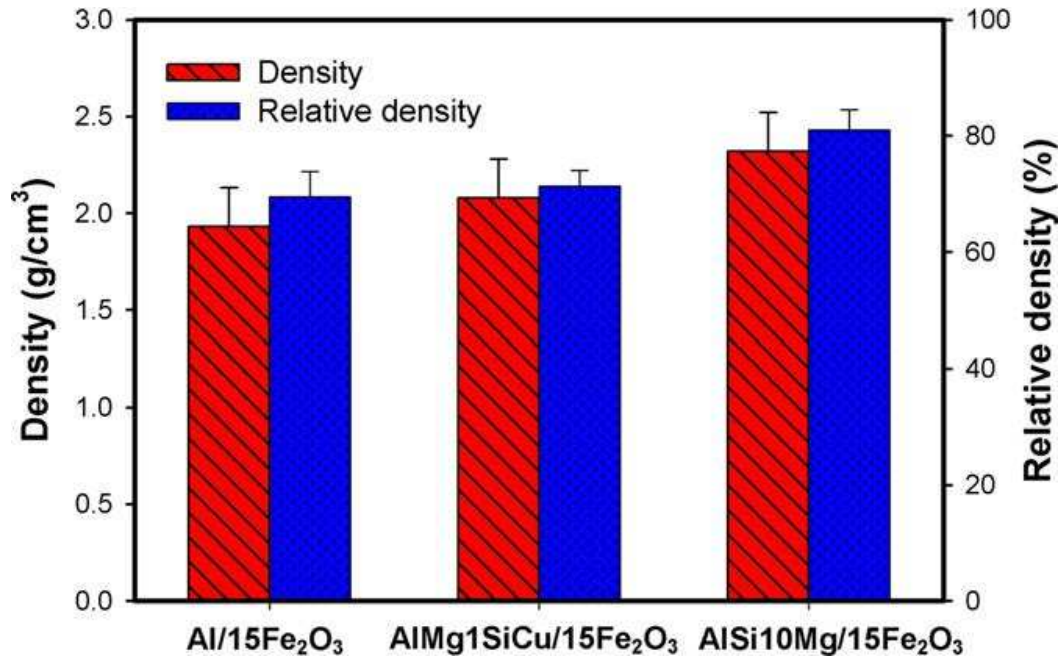


**Fig. 32.** Density and relative density of the SLM parts. The density was measured by dimensional method while relative density was achieved according to CT scanning experiments [31].

Olakanmi [40] established that AlSi12 powder had the highest sintered density among air atomised pure aluminium (AL-1), gas atomised pure aluminium (AL-2), water atomised AlMg5.6 (AL-3), water atomised AlMg6 (AL-4), and gas atomised AlSi12 (AL-5) powders. Enhanced SLS/SLM densification behaviour of AlSi12 powder was attributed to pre-alloying silicon into aluminium powder which reduces its viscosity [120], and has no effect on the surface tension of the aluminium melt pool [121], whereas increasing content of magnesium in an

aluminium melt pool reduced the surface tension while increasing the melt viscosity [122] thereby reducing the sintered density. Furthermore, the improved densification kinetics of aluminium alloy powders evident by the disruption of the oxide film covering the aluminium particles which resulted in the promotion of inter-particulate melting across the layers was found to be favoured by a high degree of thermal mismatch between the oxide film and the parent aluminium particles as well as a uniform oxide layer thickness. According to Olakanmi [40], this was the case for AlSi12 parts, whereas SLM of pure aluminium and pre-alloyed Al-Mg powders resulted in reduced sintered density. A densification co-efficient  $K$ , determined for all the powders, affirmed that AlSi12 is the most suitable SLM powder as reflected by the lowest value of  $K$  (32), highest sintered density, and coherent microstructure when compared to the other powders investigated. It is now evident that the nature of the oxide constitution of adherent films covering the aluminium particles as well as the film thickness determines whether their SLS/SLM processing will be successful or not. Therefore, introducing alloying elements, by powder producers, which form oxide films having low circumferential stress as a consequence of the significant disparity in thermal expansion co-efficient of the oxide film and aluminium particle is important for the attainment of the cracking of the film as well as full melting of aluminium alloy particles [40, 123]. Finally, a value of film thickness of around  $0.25 \mu\text{m}$  is the threshold above which thicker films would fracture whereas thinner films should just deform elastically during SLS/SLM processing of aluminium powders [40, 123].

#### *4.4 Effects of Laser Types on the on the Processing and Densification of Metal Powders*

The type of laser (see Table 7) used for SLS/SLM processing has been identified as one of the factors affecting the properties of SLS/SLM fabricated components [50]. Two most common types of lasers often applied in SLS/SLM processing are carbon dioxide (CO<sub>2</sub>) and Nd:YAG. The CO<sub>2</sub> laser is more popular due to its greater power output, higher efficiency, proven reliability and safety as well as its cost per watt output which is about 50 per cent that of Nd:YAG output [124]. With the development of high-output power, improvement in laser beam quality, and the possibility of glass fiber delivery, the Nd:YAG is increasingly used in various applications where the CO<sub>2</sub> laser had previously held sway [44, 124]. The shorter wavelength Nd:YAG laser has higher absorptivity, hence less power is required with the Nd:YAG laser in comparison to the CO<sub>2</sub> laser at the equivalent penetration depth and scanning speed [124-127]. According to Cao et al. [44], the shorter wavelength Nd:YAG laser beam allows light transmission via fibre optic cables rather than the articulated mirror delivery system for CO<sub>2</sub> laser. Therefore, this explains why a Nd:YAG laser beam is easier to manipulate and control such that the laser source may be remotely located from the SLS/SLM work station.

Moreover, the light beam from a single laser source can be delivered to a number of laser processing work stations via fibre optic delivery [44]. Through multifiber beam delivery via power or time options, multiple processing operations can be simultaneously carried out by

employing a single Nd:YAG laser source [44]. A Nd:YAG laser beam will produce a slightly larger and more stable scan track than a CO<sub>2</sub> laser beam SLS/SLM processing [7, 125, 127, 129].

**Table 7**

Commercial Machines and Lasers for SLS/SLM of Metal Powders [128].

Machines	Company	Process	Laser	Power
Sinter station 2000/2500	DTM	SLS	CO <sub>2</sub>	50 W
EOSINT 250	EOS	SLS	CO <sub>2</sub>	200 W
EOSINT 270	EOS	SLS	Ytterbium fibre laser	200 W
LUMEX 25C	MATSUURA	SLM	Pulsed CO <sub>2</sub>	500 W
TrumaForm LF 250	TRUMPF	SLM	Disk laser	250 W
Realizer	MCP	SLM	Fibre	100 W

Consequently, the wider Nd:YAG laser beam profile provides the ability to span large tracks while maintaining SLS/SLM build quality and speed, thus, leading to a more uniform scan track with little or no porosity [7, 129]. A Nd:YAG laser beam will operate at lower scanning speeds, in comparison to CO<sub>2</sub> laser beam, as a result of the reduced interaction among beam, plasma, and powder bed, thereby allowing increased powder's layer thickness to be melted [7, 129]. The reduced plasma effect allows argon to be used as a shielding gas for Nd:YAG laser processing while helium is suitable for CO<sub>2</sub> laser processing.

Lauwers et al. [125] explored the comparative fabrication of components by CO<sub>2</sub> and Nd: YAG lasers. They inferred that with the Nd: YAG laser, components of higher density, a deeper sintering depth, and a larger processing window are obtainable, given the same laser energy density for both laser types. Moreover, the studies of Hauser et al. [99, 105]; Niu & Chang [5, 82]; and Dewidar et al. [56], have all used a CO<sub>2</sub> continuous wave laser beam, which generated fairly high densities (about 55-75% of the theoretical density) for single layer tracks. However, O'Neill et al. [129] and Morgan et al. [7] utilised a Nd-YAG laser with Q-switched nanosecond pulsing for fabricating multiple layers. This pulsing generates high power densities which can lead to rapid vapourisation of the powder material, generating extreme pressures and a recoil effect which acts to flatten and widen the spherical melt bead, thereby improving the cohesive structure of layers.

Fischer et al. [130] also compared the temperature measurements between continuous wave sintering and pulsed sintering by verifying the predicted difference of skin and average temperature upon pulsed interaction. It was discovered that the average laser power required to attain consolidation of the powder in pulsed sintering is 30% lower than that reported for continuous sintering. This implies that the consolidation of the powder particles due to melting is much more efficient and generates stronger inter-particulate bonding across the layers in the pulsed laser radiation at lower wave length (1µm) than in the continuous sintering operating at higher wave length (10µm). This observation has been attributed to the presence of the temporarily higher skin temperature which was attained through lower average laser power in the case of pulsed interaction. It was pointed out the area of the temperature elevation during

continuous sintering is much larger and the achieved peak temperature nearly 1000K higher than that during the pulsed interaction which scales quite well with the higher average power. Consequently, because no complete melting occurs during pulsed interaction, reduced thermal distortion, higher lateral precisions and low residual thermal stresses in the parts can be achieved.

Abe et al. [131] also employed a dual laser scanning system combining a pulsed Nd: YAG, with a mean power of 50W and a maximum peak power of 3kW, and a CO<sub>2</sub> laser, to fabricate 3-D components from nickel, aluminium, iron, copper, stainless steel, chromium and nickel-base alloys. Their findings showed that reheating by CO<sub>2</sub> after initial heating by Nd: YAG improved the material's properties, the elimination of residual stress and ductility improvement being attributable to the reheating after melting. Steen [127] noted that in order to attain effective bonding between the layers, the depth of penetration should be of the order of the layer thickness with the aid of pulse lengths of a few milliseconds for layer thickness varying from 20 to 100 µm. Meanwhile, Dalgarno & Wright [58] noted that proper controlling of the pulsing can result in densities of up to 90% of the theoretical density.

The reported findings indicate that the type of laser employed for the SLS/SLM process determines to a very great extent, the behaviour of the powdered particles during SLS/SLM processing. The basis for these findings could be attributed to the dependence of the laser absorptivity of the investigated material on the wavelength of the laser type in use (Table 8), as

well as the resultant consolidation mechanism of metallic powders materials being a function of the energy density delivered as a consequence of laser type and the laser mode.

**Table 8**

Comparison of absorptance of single-component and two-component metallic powders using Nd:YAG and CO<sub>2</sub> lasers [126].

Material	Nd: YAG ( $\lambda$ = 1.06 $\mu$ m)	CO <sub>2</sub> ( $\lambda$ = 10.6 $\mu$ m)
Cu	0.59	0.26
Fe	0.64	0.45
Sn	0.66	0.23
Ti	0.77	0.59
Pb	0.79	-
Cu-10Al (wt.%)	0.63	0.32
Fe-3C-3Cr-12V + 10TiC (wt.%)	0.65	0.39
Fe-0.6C-4Cr-2Mo-1Si + 15TiC (wt.%)	0.71	0.42
Fe-1C-14Cr-10Mn-6Ti + 66TiC (wt.%)	0.79	0.44

The laser absorptivity and the applied energy density both determine the nature of the melt pool size. Table 8 reveals that the absorptance of metallic materials increases with decreasing wavelength which is in agreement with the findings from the literature on the SLS/SLM behaviour of metal powders when laser scanned with either CO<sub>2</sub> or Nd:YAG lasers.

Recently, a new generation of machines which employ lasers of enhanced beam quality are being developed [128]. Among such machines are EOSINT 270, TrumaForm LF 250, and Realizer. For example, Louvis and co-investigators [27] and Ahuja et al. [35] employed MCP and GmbH Realizer fiber lasers respectively at low laser powers (50 - 100W) and high scanning

rates to achieve SLM processing of 6061, AlSi12 and Al-Cu alloy powders. The outcome from these studies showed that with an optimum combination of process parameters maximum relative density varying between 89 – 99.9% was possible (Fig. 33).

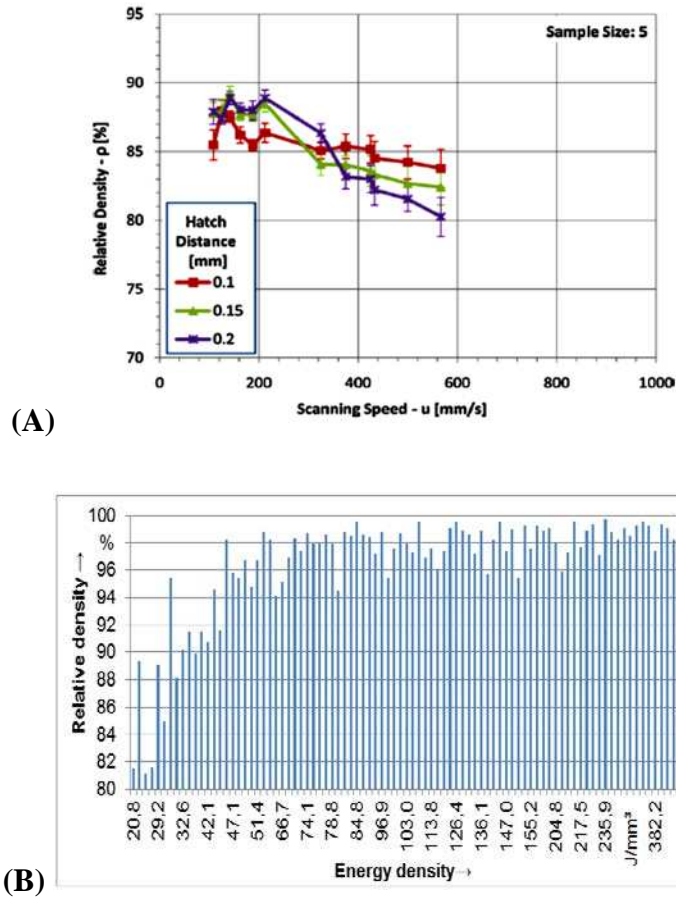


**Fig. 33.** (A) Effect of the main SLM parameters (laser scanning speed, hatch distance) on the resulting relative density of AlSi12 at 100 W [27]. (B) Relationship between Relative density in % and volumetric energy density in  $J\ mm^{-3}$  for AW-2618 processed with LBM machine system, Realizer SLM 50 [35].

The use of fibre laser in obtaining high density SLM processed aluminium alloy parts at low laser power and high scanning speeds is very promising for further development of multi additive layer manufacturing process. Machines using diode lasers are more cost effective than those employing CO<sub>2</sub> or Nd: YAG lasers, but they have limitation of poor beam quality as a result of high beam divergence, which needs to be improved upon [128, 132]. Gisario et al. [133] explored the application of a continuous wave (CW) high power diode laser to modify the surface of porous substrates made from spherical particles in sintered bronze by considering the influence of laser power and interaction time. Findings from the study indicated that a 70% decrease in the surface roughness of the porous substrates in addition to an improvement in micro-hardness, scratch and wear resistance were achievable after laser treatments when high laser power was combined with high scan speed. Meanwhile, a comparative processing test would be necessary for CO<sub>2</sub>; Nd: YAG; fibre and diode laser machines in order to observe the sintering behaviour of aluminium alloys and make conclusions regarding any of the machines that may yield a more acceptable processing window and improved functional properties for processing aluminium alloys.

## 5 Microstructure and Metallurgical Defects in SLS/SLM Fabricated Parts

### 5.1 Microstructure of SLS/SLM Fabricated Parts

SLS/SLM possesses the capability to employ transient cooling patterns to control grain sizes and shapes, phase percentages, and phase compositions in order to promote desirable mechanical properties. For instance, Zhuoxing et al. [134] demonstrated the feasibility of SLS processed Cu-Sn-C system to produce intermetallics/phases such as  $\alpha$ -Cu,  $\text{Cu}_{31}\text{Sn}_8(\delta)$ ,  $\text{Cu}_3\text{Sn}(\epsilon)$  and  $\text{Cu}_6\text{Sn}_5(\eta)$  in Cu-Sn-C systems. The Cu-based alloy was found to have a more homogeneous distribution than conventionally sintered materials as a result of improved flowability of the melt brought about by a relatively high sintering temperature. Furthermore, in an attempt to provide the necessary fundamental understanding that will lead to the fabrication of large- size, crack-free SLM processed  $\text{Al}_{86}\text{Ni}_6\text{Y}_{4.5}\text{Co}_2\text{La}_{1.5}$  metallic glass (MG) with high density, controllable microstructure and mechanical properties; Li et al. [36] reported that the morphology of the scan track of  $\text{Al}_{86}\text{Ni}_6\text{Y}_{4.5}\text{Co}_2\text{La}_{1.5}$  powder was influenced by the energy distribution of the laser beam and the heat transfer competition between convection and conduction in the melt pool. They attributed the fact that varying regions of the scan track were characterised by a gradient microstructure and mechanical properties consequent upon experiencing different thermal histories to the Gaussian distribution of laser energy and heat transfer process. They concluded that the thermal fluctuation at high laser power produced an inhomogeneous chemical distribution which gave rise to severe crystallization of the MG, despite the high cooling rate whereas the selection of an appropriate laser power resulted in crack-free scan tracks with no

crystallization. Meanwhile, an extensive search of the literature has revealed that an accurate interpretation of the complex microstructure of SLS/SLM processed samples requires knowledge of the thermal history during the process resulting from building a range of processing conditions. For example, the laser processing technique is capable of generating typical cooling rates ranging between  $10^3$  to  $10^{11}$  K/s [127, 135-138], hence, the fine microstructure usually observed in materials processed by SLS/SLM is a consequence of the high cooling rate [127, 136-138].

The nature of the microstructure obtained when laser power, scanning rates, scan spacing and layer thickness are varied is dependent on the duration of the interaction between the powder and the laser beam. The relationship between energy density and duration of laser-material interaction defines the operational regime of the SLM process which results in a unique temperature gradient (G), solidification rate (R) and cooling rate ( $dT/dt = G.R$ ). Steen [127] noted that increasing the ratio G/R results in a gradual change in the solidification regime from dendritic to cellular dendritic and consequently to planar front growth. Furthermore, higher cooling rate (G.R) promotes greater undercooling, thus producing finer grains. Hence, the parameters (G/R) and (G.R) control the type of microstructure and the scale of the microstructure, respectively [136, 137, 139, 140].

Longer laser-material duration or a higher energy density during SLM as a consequence of lower scanning rates and/or higher laser power lead to the formation of a superheated melt pool

and high surface temperature [127, 135]. Under these conditions, it takes longer for the liquid to start solidifying and the temperature of the base material becomes higher, thus lowering both the temperature gradient at the interface and the cooling rate. A coarse microstructure may result in this case. When low laser power and/or faster scanning rates are employed, superheating is not pronounced and the average temperature gradient at the interface is sufficiently high to give a faster cooling rate thereby leading to the formation of finer microstructure. The geometry of the melt bead in the SLM process is dependent on the laser processing parameters. For example, provided the energy density is less than a critical value, when the heat input is just sufficient to melt the powder, this will result in the melt pool having a cylindrical geometry due to high surface tension. The contact area between two such layers will be smaller resulting in poor heat conduction and a low cooling rate. For a multiple-layer part fabricated by the SLM process, where the substrate layers are pre-heated or partially melted in the subsequent deposition, both the cooling rate and the microstructure are affected [127]. The degree of formation of the heat affected zone (HAZ) in the deposited layer is a function of laser processing parameters. This could be responsible for the observed variations between the morphology and microstructure of individual laser deposited layers.

In order to present the background knowledge of the idea of remelting the underlying substrate with a view to weakening and/or disrupting surface contamination such as oxide films so as to provide a clean interface at the atomic level between the solid and the liquid, the principle of epitaxial solidification in SLM is highlighted by considering the work of Das [46] and other relevant fusion welding literature. Thereafter, we present various examples of how

varying SLS/SLM process parameters and powder properties affect the microstructure of laser sintered/melted metallic materials. Moreover, examples presented in these sections also demonstrated how inappropriate control of process parameters and powder properties may result in various metallurgical defects such porosity, microstructure coarsening, heterogeneity. Finally, remedial measures for the metallurgical defects are also presented.

### *5.1.1 Epitaxial Solidification in SLM*

According to Nelson et al. [141] and Das [46], SLM of metals could be likened to fusion welding. In fusion welding, the base metal and the weld metal may have similar but not necessarily the same composition, while in SLM of monolithic metallic materials, the substrate layer and the new layer of metallic powder to be melted are the same in composition. Meanwhile, it has been established that dilution of the base metal occurs in all types of fusion welding. Dilution is the partial localised remelting of the base metal which provides a continuous interface free of oxide films or other contaminants between solidifying liquid weld metal and the base metal. Dilution is a pre-requisite for good weld integrity. During dilution, or “melt back”, grain growth occurs at the solid-liquid interface between the base metal and the liquid in contact with it. Due to the significant similarities between fusion welding and SLM, it is instructive to understand the implication of epitaxial solidification on SLM process control.

In fusion welding, it is generally agreed that the liquid weld metal completely wets the partially melted substrate at the fusion boundary. Meanwhile, by likening the epitaxial

solidification mechanism in SLM to the formation of a nucleus of solid from its melt in contact with a substrate as it occurs in the fusion welding process (Fig. 34), the free energy required for the initiation of nucleation is a function of the wetting angle ( $\theta$ ) between the substrate and the solid formed. Therefore, the relationship between wetting angle and interfacial energies is illustrated in Fig. 34, Eq. (4), and (5).

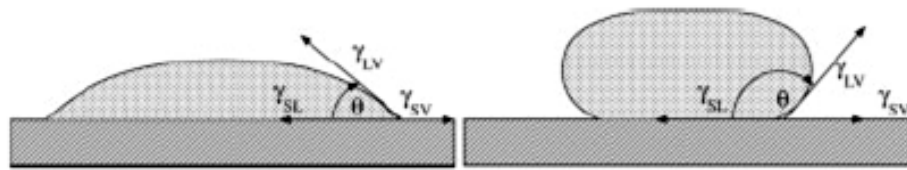


**Fig. 34.** Three-phase equilibrium for wetting and non-wetting systems [46].

$$W_a = (\gamma_{SV} + \gamma_{LV} - \gamma_{SL}) = \gamma_{LV} (1 + \cos \theta) \dots \dots \dots (4)$$

$$\cos \theta = (W_a / \gamma_{LV}) - 1 \dots \dots \dots (5)$$

where

$\gamma_{LV}$  = surface tension of the liquid-vapour interface

$\gamma_{SV}$  = surface tension of the solid-vapour interface

$\gamma_{SL}$  = surface tension of the solid-liquid interface

$\theta$  = contact angle.

During epitaxial solidification, both the contact angle, ( $\theta$ ), (Eq. (5)) and free energy  $\Delta G^*$ , become zero (Eq. (8)), and consequently, growth of the solid initiates at the fusion boundary

without difficulty [142]. As a result, it can be argued that little or no nucleation barrier in solidifying weld metals exists during fusion welding or SLM.

$$\Delta G_{het} = S(\theta) * (-V_S \Delta G_v + A_S \gamma_{SL}) = S(\theta) * (-4/3\pi r^3 \Delta G_v + 4\pi r^2 \gamma_{SL}) \dots \dots (6)$$

$\Delta G_v$  = the free energy change per unit volume associated with formation of the nucleus,

$V_S$  = The volume of the nucleus.

$A_S$  = The surface area of the new interface created by the solid nucleus and the liquid,

$S(\theta)$  = Shape factor dependent on the contact angle

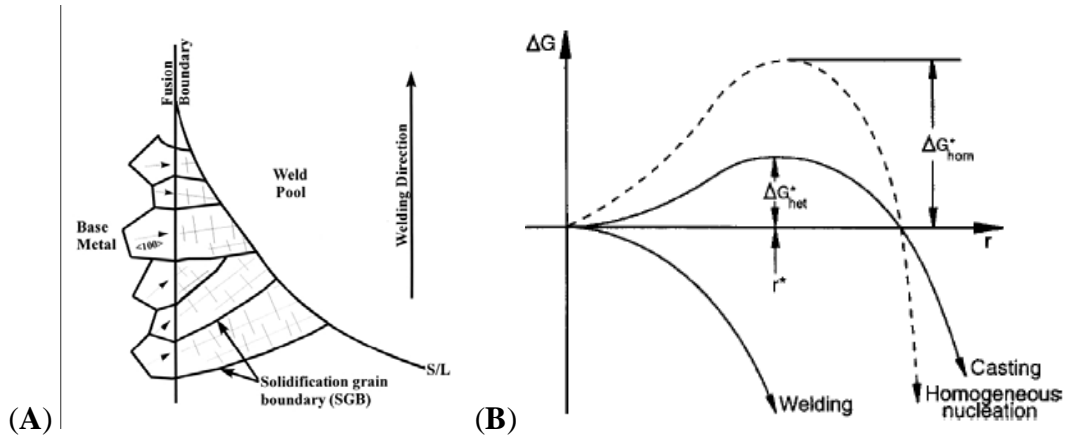


**Fig. 35.** (A) Illustration showing the epitaxial nucleation and competitive growth in the weld fusion zone [141], (B) Schematic of free energy change associated with heterogeneous nucleation in casting and welding juxtaposed with free energy change in homogeneous nucleation [143].

The critical radius  $r^*$  for heterogeneous nucleation is obtained by setting the first derivative of Eq. (6) to zero.

$$r^* = (2\gamma_{SL}) / \Delta G_V \dots\dots\dots(7)$$

The associated free energy barrier  $\Delta G^*$ , for heterogeneous nucleation is derived by substituting the expression for  $r^*$  into Eq. (6):

$$\Delta G^* = 16\pi\gamma_{SL}^3 S(\theta) / 3\Delta G_V^3 \dots\dots\dots(8)$$

According to Kou [144] and Savage [145], growth of the solid in fusion welding is perceived as being initiated by epitaxial growth from the substrate and proceeds by competitive growth toward the center line of the weld. At the fusion boundary, since the substrate is assumed to be completely wetted by the weld metal, grain growth is initiated in the weld by arranging atoms in the liquid phase on the existing crystalline substrate, thus extending the solid without altering the crystallographic orientation [146-148]. Moreover, Savage & Aronson [148] noted that solidification by epitaxial growth in fusion welding results in nearly complete continuity of the crystallographic orientation and grain boundary mis-orientation between base and weld metal grains adjacent to the fusion boundary. Therefore, Nelson et al. [141] reported that once solidification by epitaxial growth is initiated, it proceeds toward the weld center-line in a competitive-type growth mechanism illustrated in Fig. 35A above. This implies that grains with growth direction oriented most preferentially along the heat flow direction gradient tend to crowd out those grains whose growth directions are not as suitably oriented (Fig. 35A). Whereas,

the predominant mechanism of solidification in fusion welding is the competitive growth in the weld fusion zone, Kou [144] identified and discussed the details of other mechanisms such as dendrite fragmentation, grain detachment, heterogeneous nucleation and surface nucleation that may tend to interrupt and/or dominate the solidification structure in fusion welding.

Moreover, Nelson et al. [141] noted that it is unlikely that dendrite fragmentation, grain detachment, heterogeneous nucleation and surface nucleation would occur in fusion welding. In addition, Lippold et al. [149], defined the nature of the various boundaries observed in single-phase weld metal as solidification grain boundaries (SGB), solidification sub-grain boundaries (SSGB) and migrated grain boundaries (MGB). It is now understood that the nature of epitaxial growth in fusion welding metals described in this section produces a network of grain boundaries in the fusion zone (Fig. 35A). This network of grain boundaries in the fusion zone consists of the solidification grain boundary (SGB) network which is an extension of the heat affected zone (HAZ) grain boundaries at the fusion boundary. Nelson et al. [141] and Das [46] noted that the fusion boundary morphologies observed in the fusion welding of homogeneous or single-phase metal are in contrast to that observed in the welding of heterogeneous substrate and weld metals and traditional casting processes because the energy barrier in the latter processes is finite in nature (Fig. 35B).

For epitaxial solidification to take place in SLM, the substrate must be partially melted back (solidification regrowth) to promote growth from the prior grains of the substrate. For

solidification regrowth to occur, the amount of material constituted in the layer thickness of metal powder to be melted over the substrate metal must be commensurate with the laser energy intensity of the chosen processing parameters (laser power and scan rates e.t.c.). This strict control of laser-metal powder interaction is essential in order to obtain stronger interlayer bonding which results in full density components. Evidence of epitaxial solidification is usually confirmed by microstructural examination of cross-sections of SLM processed material encompassing several layer thicknesses as demonstrated by Das [46] and reproduced in Fig. 36. Fig. 36A is an example of incomplete homologous wetting and solidification whereby the melt front from the laser-melted powder layer above propagated down to barely contact the surface of the previous layer. The non-uniformity of layer thickness is especially notable. In contrast, layers in the cross-section of specimen fabricated at a higher laser power density, shown in Fig. 36B, completely indistinguishable indicating continuous grain growth across the layers. This result indicates sufficient remelt of the previous layer took place to induce epitaxial solidification. It should be noted that these micrographs traverse approximately three layer thicknesses.

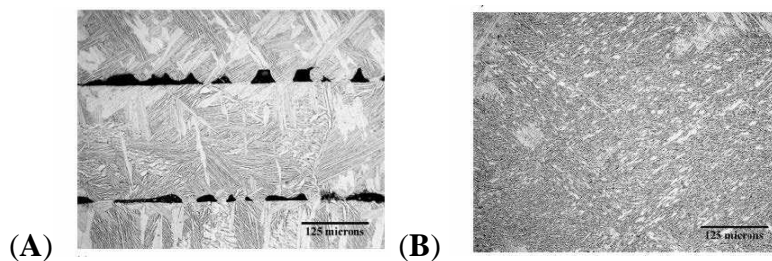


**Fig. 36.** (A) Microstructure of SLM processed Ti-6Al-4V exhibiting porosity and insufficient substrate remelts and (B) Etched microstructure of fully dense Ti-6Al-4V specimen [46].

Since SLM is a localised solidification process which occurs via epitaxial growth, evidence from Fig. 35 confirms that it can impart a finer and more uniform grain size to processed parts when compared to traditional casting processes. Consequently, this results in better mechanical properties. In summary, the mechanism for “good wetting” is ensured by partial remelting of the previous layer in SLM giving rise to epitaxial solidification. Remelting the previous layer removes surface contaminants, breaks down oxide films, provides a clean solid-liquid interface at the atomic level and allows epitaxial solidification. Laser processing parameters in SLM should be chosen so as to ensure that sufficient remelt of the previous layer takes place and continuity of the solid-liquid interface under the impingement of the laser beam is maintained.

#### *5.1.2: Effect of Processing Conditions on the Microstructure of SLS/SLM Fabricated Parts*

Olakanmi et al. [28] examined how the connectivity and orientation of the pores in the microstructure of SLS processed AlSi12 powder depended on the processing conditions using a CO<sub>2</sub> laser system. Their study shows that though the microstructures consist of small pores, the connectivity and orientation of pores are largely dependent on the choice of processing parameters which determine the quantity of specific laser energy dissipated to the powder bed. For instance, elongated pores which are nearly perpendicular to the building direction were found in a sample fabricated with laser power of 200 W; scan rates of 120 mm/s; scan spacing of 0.1 mm and layer thickness of 0.25 mm which generated specific laser energy input of 67 J/mm<sup>3</sup> (Fig. 37C). The inter-agglomerates are fully dense and consist of dendrite grains which are oriented nearly perpendicular to the build direction (Fig. 37C). Comparison of the inter-agglomerate pores obtained at specific laser energy input of 100 J/mm<sup>3</sup> and 75 J/mm<sup>3</sup> (Fig. 37A,

B) with that produced by  $67 \text{ J/mm}^3$  shows that the size of the inter-agglomerates pores are larger and appear less dense than the higher laser energy.

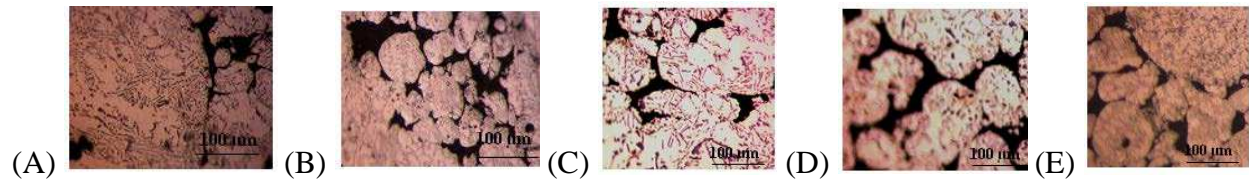


**Fig. 37.** Optical micrographs of etched, polished sections parallel to the build directions at different energy density: (A)  $100 \text{ J/mm}^3$  (B)  $75 \text{ J/mm}^3$  (C)  $67 \text{ J/mm}^3$  (D)  $40 \text{ J/mm}^3$  (E)  $13 \text{ J/mm}^3$  [28].

Furthermore, the inter-agglomerates obtained when specific laser energy inputs are reduced to of  $40 \text{ J/mm}^3$ , and  $13 \text{ J/mm}^3$  are observed not to have been as fully dense as the sample made with specific laser energy input of  $67 \text{ J/mm}^3$ . These findings are similar to the results obtained in SLS of iron [94] and H13 tool steel [104] as well as SLM of TiC/AlSi10Mg nanocomposites [39], AlSi12 [38] and AlSi10Mg [41] powders in that they identified a critical specific laser energy input at which microstructural characteristics are optimised. Above this energy input, the sintered microstructure of AlSi12 part was characterised by horizontal elongated pores while the sintered density remained almost constant.

It was also reported that both secondary dendrite arm spacing increased (Fig. 38) and the primary phase content decreased (Fig. 39) in the SLS processed AlSi12 microstructure as the

energy density increased [28]. Increased secondary dendrite arm spacing as the energy density increased was attributed to the fact that at the highest energy density ( $100 \text{ J/mm}^3$ ), there is the potential for greater melt superheat so it takes longer for the initiation of solidification therefore, a lower temperature gradient may result giving rise to a lower cooling rate, hence, coarser dendrite arm spacing (Fig. 38). Meanwhile, as the specific laser energy input is reduced by one-third to  $67 \text{ J/mm}^3$ , superheating is not so pronounced giving a higher average interfacial temperature gradient leading to a faster cooling rate and slightly finer microstructure as shown in Fig. 38.

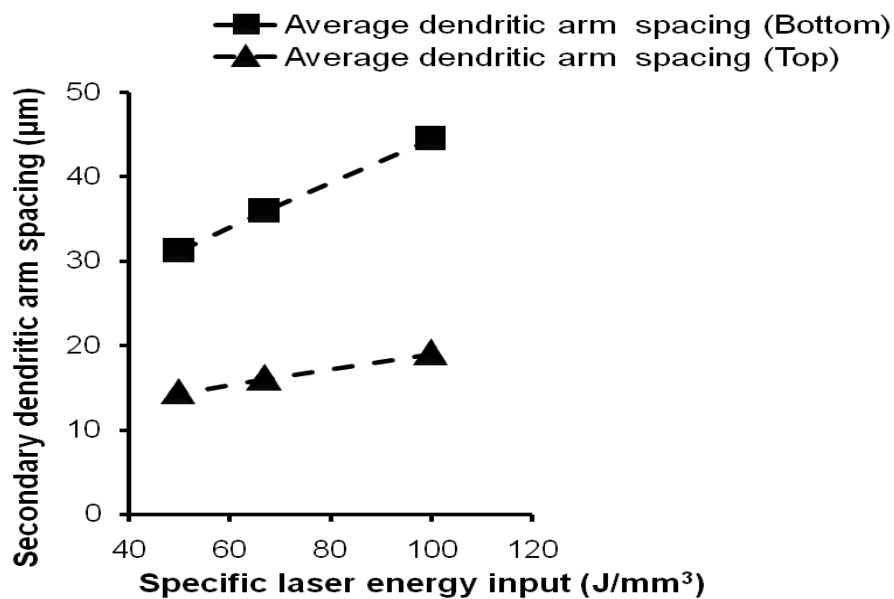


**Fig. 38.** Relationship between the energy density and the average dendritic arm spacing of the SLS processed AlSi12 powders across the depth of the laser sintered AlSi12 samples [28].

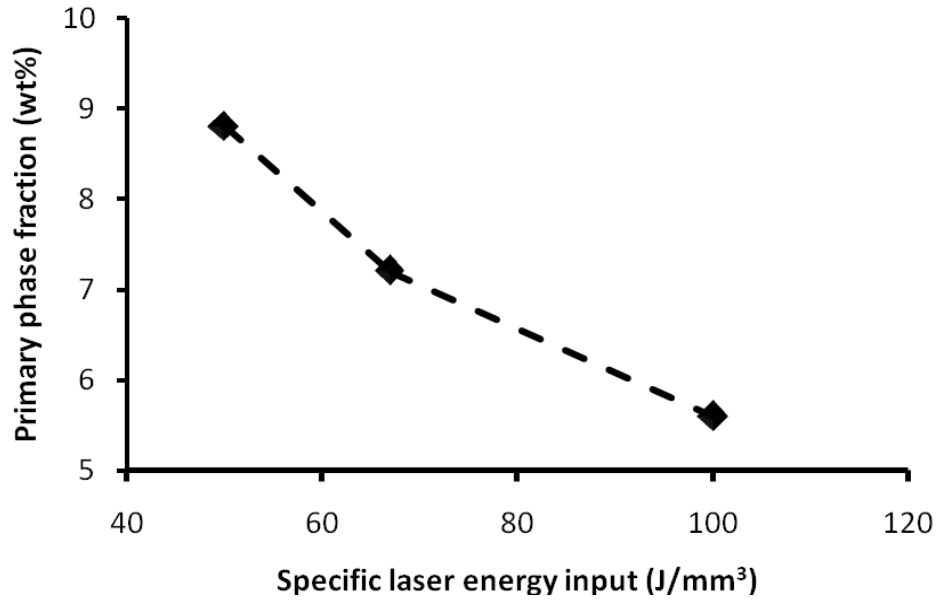


**Fig. 39.** Effect of energy density on the fraction of primary phase in SLS processed AlSi12 powder [28].

Moreover, with the specific laser energy input reduced to  $50 \text{ J/mm}^3$ , the heat is just enough to sinter the powder and the dendritic microstructure can be seen to have become finer whilst the interconnectivity of the porosity increases (Fig. 38). Furthermore, it was demonstrated that the growth of the secondary dendritic arm spacing is in direct relationship with the energy density irrespective of the depth of measurement because the dissipation of high energy density on the powder bed is accompanied by lower thermal gradient and slow undercooling which results in coarse “broomlike” dendritic microstructure (Fig. 38 and 40) [28].

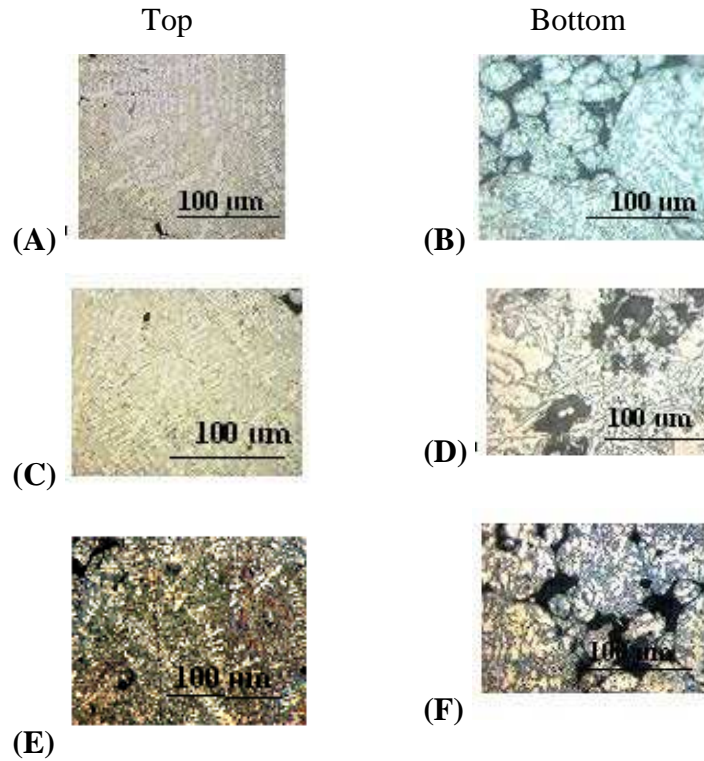


**Fig. 40.** Characteristic microstructures of SLS processed AlSi12 powder with varying processing conditions: (A, B)  $100 \text{ J/mm}^3$ ; (C, D)  $67 \text{ J/mm}^3$ ; (E, F)  $50 \text{ J/mm}^3$  [28].

In consonance with the observation of Steen [127], as the sample height increases, heat conduction through the built layers to the substrate becomes very poor and the build temperature increases (Fig. 41) thereby causing significant heating to a greater depth with microstructural changes to a larger part of the build (Fig. 38 and 40). As a result, the microstructure in the bottom part of the build (Fig. 38, 40B, D, and F) becomes coarse as evident by the occurrence of larger dendritic arm spacing which implies slower solidification rates. The occurrence of coarse structure at the bottom portion of the build could also be attributed to the lower thermal conductivity of the powder bed at the first instance laser beam was impinged on it. This initiates

low cooling rates at the bottom portion of the build. As the build height increases, subsequent layers being deposited solidify on solid metal substrates which initiates high cooling rates, thus finer dendritic microstructures are found at the top portion of the build. The disappearance of layer bands in AlSi12 parts fabricated with varying energy densities between 50-100 J/mm<sup>3</sup> could be attributed to the same effect [28] while noting that these observations made for SLS processed AlSi12 parts are similar to those reported by Srivastava et al. [150] in their studies of direct laser fabricated TiAl-based alloys.

The variation in fraction of primary phase in SLS processed AlSi12 part is marginal with variation in specific laser energy input (Fig. 39) [28]. Arnberg et al. [151] reported that the primary dendrite fraction in some Al foundry alloys decreased with increasing cooling rate whereas Veldman et al. [152] reported the opposite behaviour, a slight increase with cooling rate. Although, Olakanmi and co-investigators [28] emphasised that the processing techniques employed by these researchers is quite different from the SLS process, nevertheless, the finding from their study in respect of the influence of the cooling rates on the fraction of primary dendrite phase in SLS processed AlSi12 parts agrees with the findings of Veldman et al. [152]. The differences in the method of measurement of the fraction of primary dendrite phase as well as the chemical composition of the materials investigated by Arnberg and Veldman research groups [151, 152] should be noted as this may be responsible for the different findings of their work.

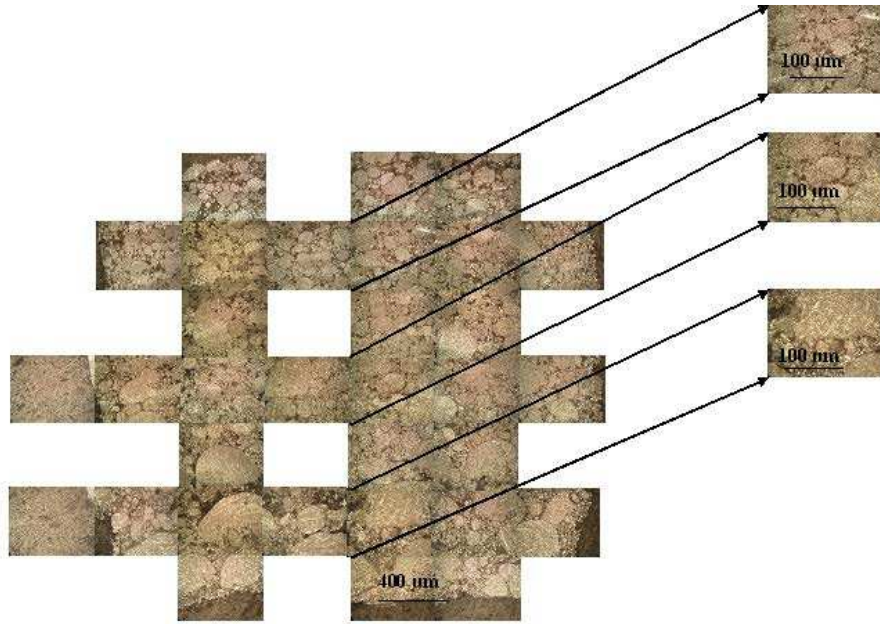


**Fig. 41.** Sections through the micrograph of AlSi12 (200W-120mm/s) generated by  $67 \text{ J/mm}^3$  [28].

Finally, it was concluded that the attainment of the highest density ( $2.05 \text{ g/cm}^3$ ) and most desirable microstructure when a critical specific laser energy input was dissipated during SLS of AlSi12 powders could be attributed to the initiation of appropriate laser-material interaction regime which generates adequate liquid phase for the solidification mechanism, inhibits the process of agglomeration, and promotes high cooling rates across the SLS fabricated specimens [28]. However, reduced densities and less desired microstructures obtained at the specific laser energy inputs lower or higher than the critical specific laser energy input could be explained by extremely shorter or longer laser-material interaction regime which promote the life time of the existing liquid phase beyond necessary, thus initiating spheroidisation, and extremely low cooling rates which result in coarse dendritic structures and porous microstructure in the

samples. It is pertinent to note that the work of Olakanmi et al. [28] is classified as SLS because the process could not impart full density into AlSi12 parts since infiltration will be needed to improve its consolidation process as well as mechanical properties.

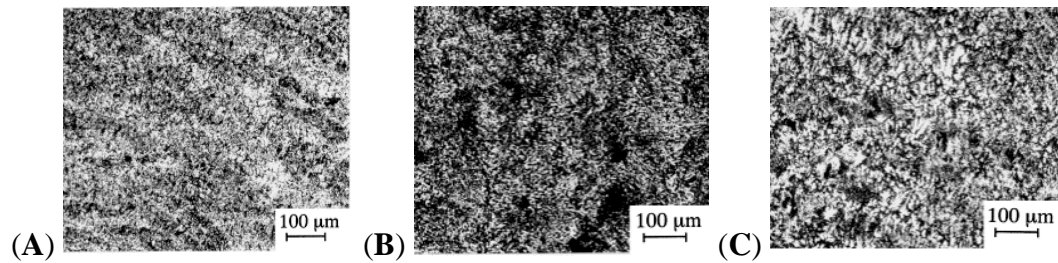


**Fig. 42.** Optical micrographs showing the variation of microstructure of Ti-48Al-2Mn-2Nb (wt.%) alloy consisting of lamellar ( $\alpha_2 + \gamma$ ), featureless ( $\gamma$ ) and partially lamellar [ $\gamma + (\alpha_2 + \gamma)$ ] and fabricated with laser power (A) 300W, (B) 360W, (C) 400W. (Scanning speed 8mm/s; powder feed rate 3g/min; z-increment 0.2mm; number of layers 20) [150].

Prior to Olakanmi et al. [28] study, Srivastava et al. [150] investigated the influence of process parameters and heat treatment on the microstructure of *direct laser fabricated* gamma titanium aluminide (TiAl) alloy samples. Their findings revealed that a variety of microstructures, ranging from cellular to columnar to dendritic morphologies and consisting of lamellar ( $\alpha_2 + \gamma$ ), featureless ( $\gamma$ ) and partially lamellar [ $\gamma + (\alpha_2 + \gamma)$ ], is obtainable upon the variation of the laser power and scanning speed (Fig. 42). Moreover, micro heterogeneous and finer microstructures were developed in direct laser fabricated titanium alloy samples by comparison with their conventionally processed counterparts due to high cooling rates.

Subsequent heat treatment of the direct laser fabricated samples eventually resulted in the elimination of the compositional heterogeneity and microstructural refinement of the samples.

Brandl et al. [30] also corroborated similar findings from the work of Srivastava et al. [150] when they investigated the impact of powder bed temperature, build orientation, and post-process heat treatment on the microstructure of Nd:YAG laser melted AlSi10Mg parts. They discovered that laser traces were present in the as-processed microstructure with its heat affected zones characterised by inhomogeneous, coarsened cellular dendrites of  $\alpha$ -Al and inter-dendritic Si-particles (Fig. 43A). Having analysed their results statistically by design of experiments, correlation analysis, and marginal means plots; they established that post heat treatment (peak hardening to T6) has the largest effect homogenising the as-built microstructure by dissolving dendrites, laser traces, and heat affected zones as the Si particles transform to globular shapes (Fig. 43B) while the building direction has the least effect on the microstructure of SLM fabricated AlSi10Mg parts.

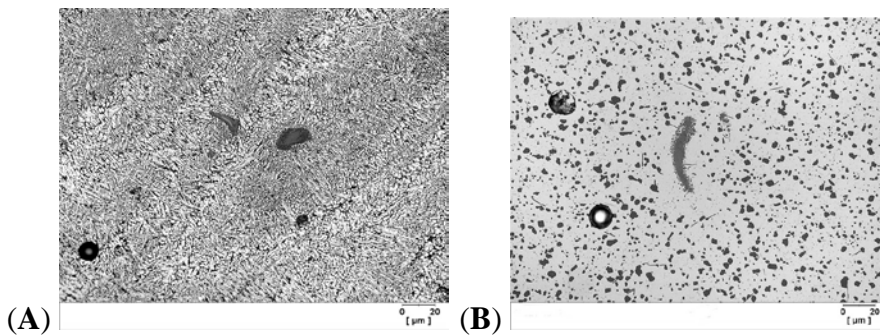


**Fig. 43.** Typical microstructure of SLM processed AlSi10Mg parts at powder bed temperature of 300 °C, and build orientation of 0°: (A) As built (B) Peak-hardened [30].

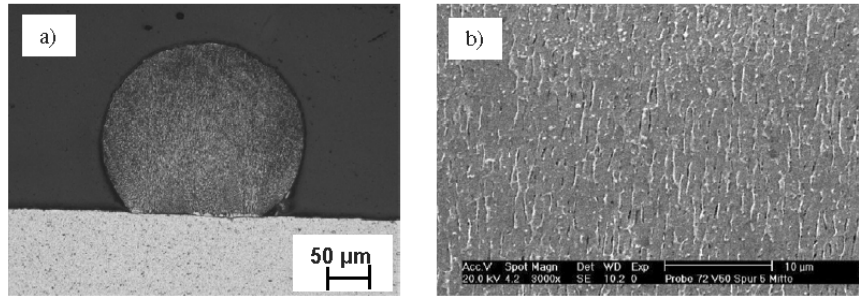


**Fig. 44.** Micrographs of aluminium alloy 2xxx on Al 6082 substrate after SLM processing (B) Optical micrograph of formation of single track; (B) SEM micrograph of microstructure of melted middle zone [153].

Fibre laser at low laser power and high scanning rates had also been employed to achieve SLM processing of a range of aluminium alloy powders [27, 36, 138, 153]. Analysis of the micrographs of the SLM processed aluminium alloys by fibre lasers confirmed that the microstructure was characterised by a high density and a crack-free structure with no occurrence of brittle hard oxidation layer (Fig. 44A and B). On a final note, of great interest is the recent work of Huang et al. [154] who addressed the SLS/SLM constraints of settings optimal parameters to obtain a dense product by employing electromagnetic vibrations (Fig. 45A) to alter the solidification process thereby allowing the microstructure (Fig. 45B and C) to be varied via magnetic flux density. This technique may be adopted for creating microstructure-controllable products with complex shapes.

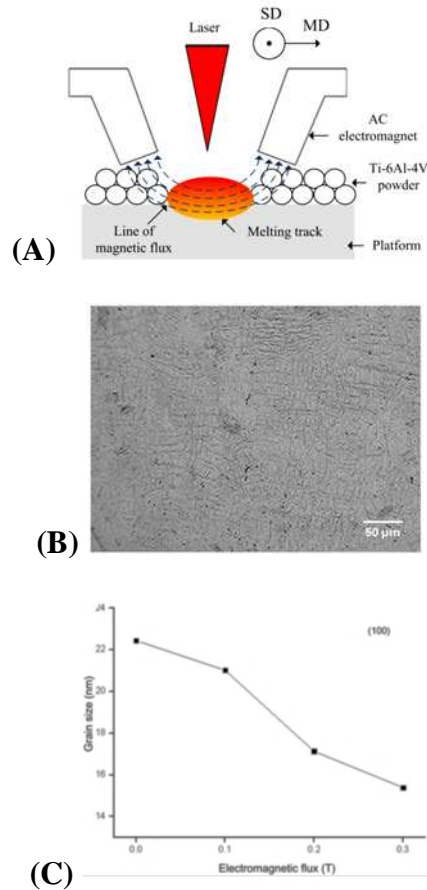


**Fig. 45:** (A) Diagram of basic SLM experimental platform with dual-magnetic-pole AC electromagnet (SD: scanning direction of laser; MD: movement direction of electromagnet). (B) optical metallographic images for Ti-6Al-4V SLM part. (C) Variations of electromagnetic flux density with the average grain size [154].

Analysis of the literature cited in this section reveals the following:

- Microstructural evolution in SLS/SLM fabricated parts is controlled by the specific laser energy input.
- The use of suitable heat treatment (e.g. peak hardening to T6 temperature) is able to homogenise the microstructure of as-built SLS/SLM fabricated parts.

- The use of both CO<sub>2</sub> and Nd:YAG laser systems imparts defects such as porosity, and cracks into the as-built SLS/SLM fabricated microstructure while fibre laser SLM processed specimens are crack and pore free.

### *5.1.3 Effect of Powder Properties on the Microstructure of SLS/SLM Processed Components*

*5.1.3.1: Effect of Particle Size on the Microstructure of SLS Processed Components:* Niu & Chang [5] observed that SLS of gas atomised powder yielded a highly porous structure when the particle size was small (<38 μm) or coarse (>150 μm) but discovered that laser sinterability was better for particle sizes ranging between 53 and 150 μm as evidenced by a smooth, dense surface of the single layer part (Fig. 46). They attributed the behaviour of finer particle sizes under SLS to oxidation, which is more dominant when heating powder of smaller particle sizes. The porous structure might have been as a consequence of incomplete wetting rather than some other phenomenon being governed only by particle size. Niu & Chang [5] also stated that large particles (>100μm) require higher laser power for melting since heat transfer into the powder layer is lower. Therefore, for a given energy density, the structure tends to be more porous than a structure produced using smaller particle sizes. The observations of Niu & Chang [5] are only indicative: to ascertain the actual impact of the particle size and shape on the microstructure and mechanical properties, multiple layer experiments need to be carried out.

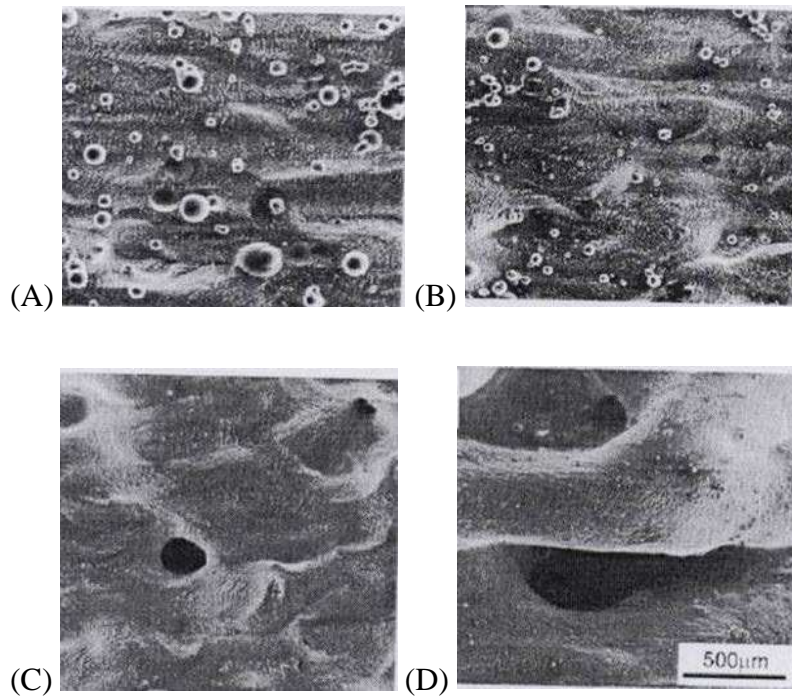


**Fig. 46.** SEM images of laser sintered high speed steel powders using laser power of 50 W and a scan rate of 5.0 mm/s and a scan line spacing of 0.15 mm. Particle sizes were: (A) as supplied from atomiser (full range), (B) 53  $\mu\text{m}$  – 150  $\mu\text{m}$ , (C) >150  $\mu\text{m}$  and (D) <38  $\mu\text{m}$  [5].

*5.1.3.2 Effect of Alloying on the Microstructure of SLS/SLM Fabricated Parts:* It is widely believed that additives can have profound effect on the microstructure of laser-sintered components: this is illustrated in the following examples. Murali et al. [155] investigated the SLS of a powder mixture of iron and graphite (99.22wt.% and 0.78wt.% respectively) using a pulsed Nd: YAG laser and observed the laser sintered iron-graphite parts to be porous with a microstructure and mechanical properties substantially different from the same parts fabricated from the same powder mixture via conventional P/M. Moreover, they discovered that the carbon content in the sintered samples was as low as 0.3wt%. They concluded that in order to achieve a

target carbon content, a powder mixture of higher graphite content must be used. Simchi & Pohl [156] followed up this suggestion by varying the graphite content between 0.4 to 1.6wt% in direct laser sintering. They found that with the addition of graphite (0.4wt% to 0.8wt%) to the iron powder, the continuous network of pore channels was eliminated and irregular shaped pores surrounded by a fully dense iron matrix were formed (Fig. 47B and C). The microstructure consisted of small, spherical pores with no degree of orientation. With increasing graphite content (1.2wt%), the total porosity decreased steadily, and more pores were found in the microstructure (Fig. 47D). Simchi & Pohl [156] clearly demonstrate that a heterogeneous distribution of carbon in the iron matrix (Fig. 48 and Table 9) leads to the formation of different phases as corroborated through the work of Murali et al. [155].

**Table 9**

The local carbon concentration measured by X-ray photoelectron spectroscopy (XPS) method and microhardness values of marked areas in Fig. 48 [156].

Area	Possible phases	Carbon content (wt.%)	Hardness (HV <sub>0.025</sub> )
I	Ferrite	0.1	137
II	Tempered Martensite	1.6	463
III	High Carbon Austenite	1.9	476

Similar results were obtained for the other sintered parts, although heterogeneity is more pronounced in the case of samples having higher graphite content. The work of Simchi & Pohl [156] and Murali et al. [155] once again have directed attention to the issue of altering the starting powder composition and making the correct choice of alloy addition in order to

overcome the problem of heterogenous distribution of phases with the resultant poor mechanical properties.

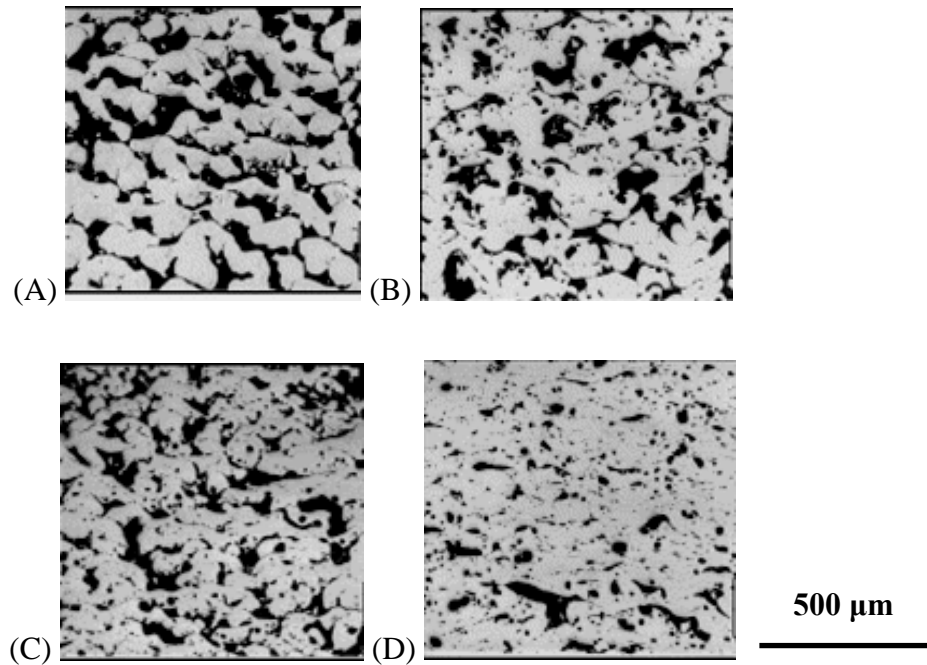


**Fig. 47.** Polished section of laser sintered parts shows the effect of graphite addition on the pore structures on a section cut parallel to the building direction; laser power is 215 W, scan rate is 75 mm/s, scan line spacing is 0.3 mm, and layer thickness is 0.1 mm (A) 0% C (B) 0.4% C (C) 0.8% C (D) 1.2% C [156].

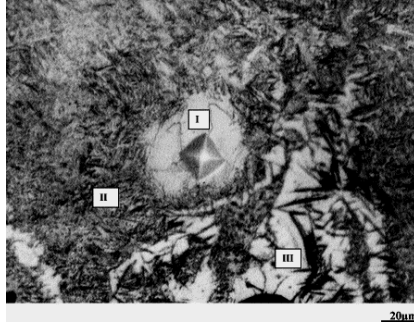


**Fig. 48.** Characteristic microstructure of laser sintered iron-1.2 wt.% graphite powder mixture on a section cut parallel to the building direction shows heterogeneous carbon dissolution in the iron matrix resulting in the varying local hardness values (Table 2.4). Laser power is 215 W, scan rate is 75 mm/s, scan line spacing is 0.3 mm, and layer thickness is 0.1 mm [156].

Prior to these findings, Tang et al. [57] described how microstructural features such as porosity, pore size and shape, the agglomerate size, and grain shape of laser sintered copper alloy (Cu and Cu<sub>3</sub>P) are associated with the variation of the amount of *in-situ* - deoxidiser (SCuP). They noted the existence of a large amount of pores at a low SCuP level (25vol%) with small agglomerate sizes (200-300 μm) of ball-like shape. When the amount of deoxidiser increased to 40vol%, more molten binder flowed and infiltrated into pores between the copper particles, thereby forming big agglomerates and a denser microstructure, but the pore sizes became larger. However, at higher fractions of SCuP, the re-arrangement force is higher and the viscosity of the mixture was lower, leading to faster re-arrangement of Cu particles and spreading of the binder. The molten binder spreads and wets the Cu particles well. The copper particles are pulled together by the liquid towards the centre of a laser scan path, thus forming long bar shaped tracks. Tang et al. [57] concluded that high porosity was still left in the microstructure due to the

short transient interaction duration (0.1 to 1s) between laser and metal powder. The porosity could be eliminated by the appropriate choice of the laser processing parameters which allows sufficient laser-material interaction duration that eliminates porosity and balling.

Moreover, the work of Zhang et al. [118] also affirmed that the addition of nickel (Ni) to SLM fabricated tungsten components in varying contents of 10, 20 and 40wt% resulted in bar-shaped structures, dendrites and honeycomb structures respectively via a mechanism consisting of the combination of LPS and partial melting of W particles. Meanwhile, the findings in this section corroborate the results obtained from the investigation on the effect of component ratios on the attainable liquid phase which determines, to a very great extent, the nature of microstructural features and densification mechanisms of direct laser sintered powders (see Section 3.2). Therefore, the right choice and correct amount of the appropriate additive for microstructural improvement in a typical SLS powder system is very important.

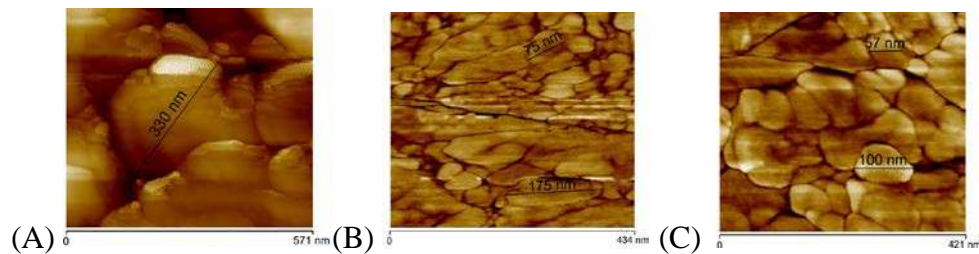


**Fig. 49.** AFM results presenting ultrafine/nanoscale particles in the cross section of the SLM parts made from (A) Al/15wt%Fe<sub>2</sub>O<sub>3</sub>, (B) AlMg1SiCu/15wt%Fe<sub>2</sub>O<sub>3</sub>, and (C) AlSi10Mg/15wt%Fe<sub>2</sub>O<sub>3</sub> [31].

Dadbakhsh & Hao [31] studied the effects of alloying composition of Al, AlMg1-SiCu and AlSi10Mg on the microstructure of SLM facilitated aluminium matrix composites via *in-situ* interaction with 15 wt%Fe<sub>2</sub>O<sub>3</sub>. They discovered that the *in-situ* composites made from all the Al alloys were reinforced by abundant and very fine particles with the *in-situ* composite made from AlSi10Mg containing the finest particles typically around 50–100 nm in size (Fig. 49). Moreover, a solid solution strengthening mechanism resulted in the microstructural characteristics of the composites having significant superior microhardness than that of unreinforced aluminium alloys thereby suggesting the promising prospective of SLM facilitated *in-situ* reaction to produce advanced Al MMCs. The *in-situ* formed particles in the composites were Al oxides (i.e., stable  $\alpha$ -Al<sub>2</sub>O<sub>3</sub>), Al–Fe intermetallics (i.e., equilibrium Al<sub>13</sub>Fe<sub>4</sub> and other non-equilibrium Al–Fe phases), and Si crystals (alone or in combination such as Al<sub>0.5</sub>Fe<sub>3</sub>Si<sub>0.5</sub>, Al<sub>0.7</sub>Fe<sub>3</sub>Si<sub>0.3</sub> and Al<sub>3</sub>FeSi<sub>2</sub>), depending on the Al alloy composition. The lower thermal conductivity of AlMg1SiCu or AlSi10Mg caused transformation of non-equilibrium Al–Fe intermetallics into equilibrium Al<sub>13</sub>Fe<sub>4</sub> thereby resulting in extension of the solubility of Mg, Si, and Cu in Al matrix via rapid solidification.

Meanwhile, there is still scarcity of literature dealing with the effect of sintering atmospheres and alloying additions in the SLS/SLM of aluminium or its alloys on microstructure with the exception of Wang et al. [38] who established that a He atmosphere produces lower ductility due to the formation of pore clusters in the AlSi12 microstructure whereas both argon and nitrogen atmospheres result in the SLM produced parts having a small amount of porosity. However, the mechanism responsible for the He processed porous microstructure as well as Ar

and N processed well consolidated microstructure is not currently understood. In addition, Ferrar et al. [157] examined the effect of inert gas flow within the SLM process as well as the nature of its influence induced by this gas flow on the reproducibility of the key attributes of porous titanium components. It was revealed that the measured attributes were significantly affected by the improved gas flow, with porosity reducing and the compression strength improving. Ferrar and co-investigators then incorporated the design modifications into a new machine designed to enable the production of porous components of closer control and greater reproducibility. Reports on the indirect SLS of aluminium alloys carried out at the University of Queensland in Australia, document the effects of nitrogen sintering atmospheres and alloying addition but only as they affect the dimensional stability of the components, [158-161] as no mention is made of their effect on microstructure.

## *5.2 Metallurgical Defects*

Common metallurgical defects in SLS/SLM processed metallic parts are porosity, cracking, oxide inclusions, and loss of alloying elements. In the remaining parts of this section, each of these defects is elucidated by highlighting the mechanism of their formation, main influencing factors, and the remedial measures.

### *5.2.1 Porosity*

Typical porosities common in SLS/SLM processed parts are insufficient/incomplete melting (lack of fusion) porosity; porosity as a consequence of entrapment of gases by surface

turbulence, and shrinkage porosity [28, 41, 96, 162, 163]. Porosities caused by insufficient/incomplete melting (lack of fusion porosity) are usually found along layer boundaries, irregularly shaped, and elongated in the x-y plane of the deposit with the size and number of pores strongly influenced by processing parameters such as laser power, layer thickness, scanning rates, and scan spacing [28, 41, 96]. The highest fusion porosity is obtained in regions having a preponderance of insufficient/incomplete melting across the interlayers, whereas the porosity is minimised when laser processing results in continuous interlayer melting [28, 41, 50, 95, 96]. Poor fusion porosity has been attributed to insufficient dissipation of the laser energy density into the powder layer thickness such that the top of the previous layer cannot be re-melted to attain coherent bonding (Fig. 19 and 36).

Another possible explanation for the low fusion porosity in SLS/SLM processed parts is that the gas bubbles are entrapped in the interlayers during laser scanning. The entrapment of the gas bubbles thereby results in an unstable scan track because the vapourisation of the scan tracks is not uniform while their positions vary with time [7, 58, 96, 129, 163]. Scan track stability during SLS/SLM processing is also a function of the balance of forces active within the scan track. With the formation of a vapour cavity, the fluid forces of the molten pool tend to be balanced by the vaporisation pressure within the cavity [7, 58, 96, 129, 163]. The characteristic instability of the scan tracks consequently results in periodic collapse of the liquid metal surrounding the vapour cavity and the formation of periodic voids [7, 58, 96, 129, 163]. It was speculated that the metallic vapour was the major gas inside the scan track, with some shielding gas, possibly entrained into the scan track [7, 58, 96, 129, 163]. With the metal vapour thought to

have condensed during cooling; therefore, the main gas species in these pores at room temperature are expected to be mainly the entrained shielding gas. In order to reduce porosity, the scan track must be kept stable by employing high power/high speed SLS/SLM processing parameters [162]. Another possibility is the use of high-power continuous wave Nd:YAG lasers resulting in only a slightly ionised vapour flow [7, 58, 129]. The shorter wavelength of Nd:YAG lasers, in comparison to CO<sub>2</sub> lasers, is responsible for less severe plasma effects (absorption and defocusing); thus leading to improved stability of the scan track [7, 58, 99, 105, 129, 164]. Moreover, increased average power (and hence energy density) dissipation on the powder bed/substrate has been found to maintain a continuous scan track during SLS/SLM processing [162].

Similar to the processing conditions in laser welding, it is also possible that scan track instability and pore formation may also be minimised by suitably adjusting the defocus of the beam [165]. It had also been reported that during pulsed wave (PW) laser processing, there is a scanning speed at which the occurrence of porosity reached a maximum. This was attributed to the potential for gas to escape during the delayed solidification time at high energy density (low scanning rates/high laser power) and at reduced depth of the scan track at low energy density (high scanning rates/low laser power). Pulsed laser systems may provide the possibility to control the laser energy dissipation into the powder bed/substrate and thereby control the solidified microstructure, porosity, and solidification cracking [130]. The stability of the scan track is greatly affected by the pulse because each pulse has to reopen the scan track after its breakdown. Process cavities can be reduced if the porosity formed in a previous pulse is

effectively removed from the scan track formed by the next pulse when the overlapping ratio of two scan tracks is adequate [7, 58, 129, 130, 164]. Therefore, it is recommended to shorten the off-time of the pulse to less than the solidification time of the molten pool [7, 58, 129, 130, 164]. This requires a high-duty cycle and high amount of overlap of the fusion zone during one pulse transition [7, 58, 129, 130, 164]. It is recommended the adoption of short pulse durations and low energies in the case of pulsed wave systems to keep the area melted as small as possible [7, 58, 129, 130, 164]. A pulse shape with gradually decreasing peak power levels or possibly combined with the use of a CW laser beam can also be used to reduce or prevent porosity and cracking [131]. The proper tailing wave allows withdrawal of the scan track gradually during solidification while the CW contribution causes a preheating effect to increase absorptivity [131]. With the development of high-power and high-quality lasers, stable scan tracks can be obtained, especially using CW Nd:YAG lasers.

Moreover, porosity may still occur by another important mechanism, i.e. the entrapment of gases by turbulent flow of liquid metal in molten pools as mentioned in [7, 58, 96, 129, 162, 166]. Gases are entrapped into liquid metal in the molten pool via surface turbulence (but not bulk turbulence). The entrapment of gas and surface oxide films via surface turbulence had been explored in castings [167]. The turbulent motion in a molten pool is supposed to be extensively understood in SLS/SLM: however, no investigation has been conducted on this mechanism. As noted earlier on, the entrapped gas by this mechanism was thought to be the shielding gas [162]. Possibly, the entrained gas species by surface turbulence may be metal vapour, shielding gas, or their combination. Further study is needed to explore the mechanism and control fluid motion in

the molten pool to avoid entrapment of gases (and the possible entrapment of oxide films). Shrinkage porosity occurs during solidification as a consequence of inadequate metal feeding [28].

In summary, three mechanisms of pore formation may operate in SLS/SLM processing: however, the dominant mechanisms for pore formation during SLS/SLM processing of aluminium alloys need to be thoroughly investigated. The collapse of imperfect scan tracks or surface turbulent flow in the molten pool is considered to be the main causes of pores during SLS/SLM processing of metallic powders. An explicit relationship between the types of porosity and SLS/SLM process parameters is still lacking. Moreover, no information is available on the structural significance of small pores in SLS/SLM processed aluminium alloys.

### *5.2.2 Cracking*

The tendency of aluminium alloy parts processed by SLS/SLM to encounter cracking is very strong. This could be explained by their large solidification temperature range, high coefficient of thermal expansion, and large solidification shrinkage [4, 168]. Similar to laser welded aluminium alloy components, SLS/SLM processed parts can also encounter liquation and solidification cracks. Liquation cracks had been attributed to the high amount of alloying additions, present in heat treatable alloys, which precipitate low melting point eutectic phases [4, 168]. Provided sufficient stress is present with the application of high laser energy density, the melt will tear. Occurrence of liquation cracking can be reduced in SLS/SLM processed aluminium alloy parts by minimising the dissipated energy density on the powder bed/substrate.

Liquation cracking has not been investigated in SLS/SLM processed aluminium alloy parts. Therefore, a detail study exploring how the SLS/SLM process parameters, powder properties, alloy composition, cooling rates, and part geometry influence the susceptibility of SLS/SLM processed aluminium alloy parts to liquation cracking will be necessary.

Solidification cracking had been observed in SLS/SLM fabricated parts made in several alloyed metallic parts [169]; however, it is scarcely observed in aluminium alloy parts processed with CW Nd:YAG laser systems while the contrary is true for PW Nd:YAG laser systems [30, 170]. Moreover, heat treatable 2000 and 6000 series alloys are known to be more susceptible to solidification cracking than work hardening 5000 alloys during laser processing [4, 165, 171, 172]. Cao et al. [168] highlighted how different theories have been employed to elucidate the mechanism of solidification cracking in laser processing. They asserted that solidification cracking is a function of the interaction between the augmented strain rate and the total strain resulting from external displacement and internal free shrinkage related to the ductility curve. On the basis of the outcome of the study by Cieslak & Fuerschbach [170], who compared the hot cracking susceptibility data of Al-Mg-Si alloys fabricated via casting and arc welding with PW Nd:YAG laser processing, it was established that the guidelines developed for minimising occurrence of solidification cracking in arc welding needed to be modified for laser processing because the cooling rates and the heat inputs encountered are different.

Solidification cracking in aluminium alloy parts had been found to be metallurgically influenced by the temperature range of dendrite coherence, and the amount of liquid available

during freezing [30, 172]. The possibility for solidification cracking to occur is higher when an alloy has a wide critical solidification temperature range because solidification strains are directly related to the temperature interval over which solidification takes place and the tensile properties and ductility of the alloy are low in the freezing range [30, 171-173]. In regards to SLS/SLM processing, the actual liquidus and solidus temperatures are depressed further because of a lack of diffusion during non-equilibrium rapid solidification [30, 45]. Consequently, a wider critical temperature range and higher solidification cracking susceptibility are expected during SLS/SLM processing of aluminium alloys. Analysis of the literature on the solidification cracking susceptibility of laser processed aluminium alloys confirms that its occurrence is more pronounced in 0.8% Si in Al-Si; 1 to 3% Cu in Al-Cu; 1 to 1.5% Mg in Al-Mg; and 1% Mg<sub>2</sub>Si in Al-Mg-Si alloys [168]. The addition of alloying elements with a view to narrowing the critical solidification range can also alter the melt pool composition to avoid cracking [30, 172, 174].

During solidification, alloying elements and impurities are segregated at the grain boundaries by a micro-segregation mechanism, causing liquation films to persist down to low temperature [172, 174]. To minimise the initiation of stresses and cracks, it is necessary that sufficient liquid is available to fill in the cracks and take up the strain formed during solidification [172, 174]. Therefore, crack initiation by strain evolution competes with crack healing via refilling by residual liquid. Even though, crack initiation rate increases with strains, the refilling and healing movement of the residual liquid are controlled by its fluidity [172, 174]. The amount of eutectic necessary to prevent cracking varies with composition and freezing rate. The 5000 series alloys are not susceptible to solidification cracking due to their high Mg

contents, whereas, heat treatable alloys have higher solidification cracking tendency as a result of greater amount of alloying which create a tendency to form low melting constituents and widen the critical temperature ranges [2]. Therefore, 5000 alloys can be SLS/SLM processed without solidification cracking, whereas 2000 and 6000 alloys require alloying addition to modify composition and avoid solidification cracking [175].

The solidification cracking susceptibility of SLS/SLM processed aluminium alloys is expected to be process sensitive. In SLM process, it had been reported that there exists an optimum laser energy density at which a crack-free fully densified part is obtainable. Above this value, solidification cracking occurs at energy density higher than the optimum value due to a low liquid viscosity, a long liquid lifetime, and resultant elevated thermal stresses; whereas at lower energy density, a disorderly liquid solidification front and a significant balling effect result in crack formation due to an enhanced instability of the liquid caused by Marangoni convection [28, 36, 176].

The dissipation of lower laser energy density enhances the tendency for a fine dendritic structure and grain size on the SLM processed part as a consequence of rapid cooling [28, 176]. The occurrence of solidification cracking suggests that rapid cooling associated with lower laser energy density ensures the mushy zone remains wide in the laser processed parts [168]. Rapid cooling accelerates the development of high thermal shrinkage strains and increases stress gradient that promote high crack initiation rate. The residual liquid along grain boundaries in the mushy zone may be formed in a film-like shape, leading to easier concentration of strains and

occurrence of solidification cracks during SLM processing [162, 169]. Moreover, rapid cooling also reduces the time required for the residual liquid to refill and heal the initiated cracks [162, 169, 177]. According to Cao et al. [168], rapid cooling rate may also be responsible for the increased solidification crack susceptibility in pulsed laser processed parts; though, pulsed-laser processing produces grain refinement and higher process control flexibility in comparison to CW laser processing. For example, higher susceptibility of solidification cracking and porosity at lower duty cycles was established by PW Nd:YAG processing of 2024-T3 alloy [177].

In similarity to laser welding, it is expected that by decreasing the cooling rate and the solidification rate, especially at the late stage of solidification of the melt pool during SLM processing, the propensity for the formation of solidification cracking will eventually be reduced [168]. During PW laser processing, higher pulse repetition rate and higher duty cycle are effective in reducing cracking [7, 129]. According to Morgan et al. [7]; O'Neil et al. [129]; and Cao et al. [168], the cracking may be prevented during PW laser processing provided the next pulse takes place before the initiation of solidification cracking caused by the previous pulse. On this ground, it is recommended to shorten the off-time of the pulse (using high duty cycle) to less than the solidification time of the molten pool [7, 129, 168]. The control of pulse shape with gradually decreasing peak power levels (tailing) or possibly combined with use of a CW laser beam can be used to reduce or prevent porosity and cracks [131].

Moreover, Cao et al. [168] noted that during the pulsed mode of operation, a pulse with a laser output greater than a minimum is thought to be effective for crack prevention. Since the

susceptibility of wider parts to cracking is less than that for narrower parts, a larger focussed spot size and a lower scanning speed to produce wider parts may overcome cracking [168]. Preheating the powder bed or the substrate can also avoid solidification cracking because it affects cooling rates [30]. To produce crack-free SLS/SLM processed parts, it is necessary that investigation is carried out to define the parameter-operating window for different aluminium alloys.

### *5.2.3 Oxide Inclusions*

The surface oxide film is known to inhibit the densification mechanism by promoting balling and disrupting inter-particulate coalescence/wetting across the laser sintered/melted layers. Similar to the casting process as pointed out by Campbell [167], oxide may get into the melt pool either via alloying addition into the metal powder during primary processing (“old oxides”) or air/gas entrapment via surface turbulent flow (“young oxides”) during SLS/SLM processing. For example, addition of Mg or Si to the aluminium alloy prior to atomisation might be expected to change the nature of the oxide film. Specifically, Mg promotes the formation of spinel ( $\text{MgAl}_2\text{O}_4$ ) in thin layers and Si, the formation of mullite ( $\text{Al}_2\text{O}_3 \cdot \text{SiO}_2$ ) [178]. As noted earlier on, because the vapourisation of alloying elements in the scan tracks is not uniform while the scan track positions vary with time, rapidly fluctuating scan tracks tend to entrap the shielding gas or even air since the shielding gas may not be truly pure [7, 58, 129, 179]. Consequently, some oxide particles possibly occur in the scan track vapour. The surface of the liquid metal in the melt pool then become oxidised to form oxide film as a result of the entrapment of air or shielding gas into the melt pool.

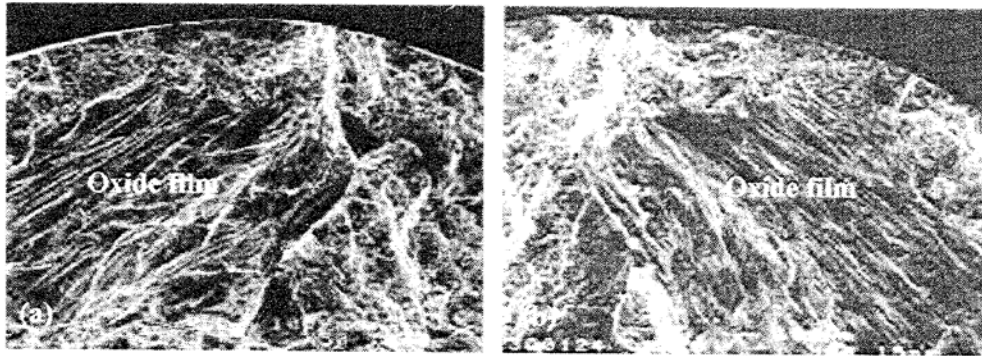


**Fig. 50.** SEM secondary electron image taken from the two opposing fracture surface of sand cast Al-Si11.5-Mg0.4 showing an extensive double oxide film [180].

Oxide films in powdered aluminium alloys have two sides: the dry, unbonded inner surfaces, and their wetted exterior surfaces. According to Campbell [167], oxide films are always folded dry side to dry side (on the opposing fracture surfaces of a tensile casting as shown in Fig. 50. The wetted sides of oxide films during SLS/SLM processing of aluminium alloys may possibly nucleate into intermetallics phases as cracks in the fabricated parts. In agreement with Nyahumwa and co-researchers [181], other possible position for oxides in SLS/SLM processed aluminium alloys may be the grain boundaries since aluminium dendrites are unlike not nucleate through the unwetted dry side of the oxide films. Consequently, according to Cao & Campbell, [182], the gap between the two dry sides of the folded doubled oxide films constitutes the cracks in the aluminium alloy part with the width between them always less than 10  $\mu\text{m}$ . Therefore, the unwetted dry sides of oxide films become the potential nucleation sites for gas and shrinkage porosity [167]. Oxide films in the inside surfaces of porosity had been reported in laser processed

aluminium alloy parts [168]. The oxide films as cracks in nature are expected to initiate cracks or inclusions in the SLS/SLM processed aluminium alloy parts.

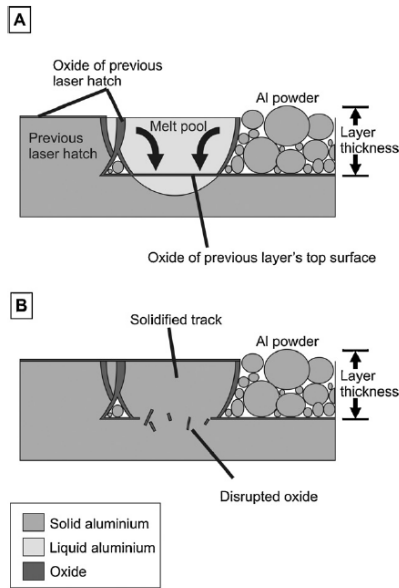


**Fig. 51.** (A) Marangoni convection in the melt pool. (B) Oxide disruption and solidification of the melt pool [27].

Louvis et al. [27] pointed out that the difficulties encountered when SLM processing aluminium and its alloys appeared to be caused by thin oxide films, and in many ways these defects are the same as those seen in conventional casting. They observed that the formation of oxide films on both solid and liquid metal surfaces leaves oxide films between the laser hatches at every layer of the aluminium parts and where two oxide films meet then pores are formed (Fig. 51). As noted earlier on, since the formation of oxide films cannot be avoided completely, the SLM process must break up these oxides if fully dense parts are to be formed, and this is why SLM fabrication of high density parts requires high laser power. According to Louvis and co-researchers, the

oxide film on the upper surface of the melt pool evaporates under the laser beam but on the other surfaces it remains intact. They then reasoned that Marangoni forces that stir the melt pool are the most likely mechanism by which lower oxide films are disrupted but not the sides, thereby creating the ‘walls’ of oxides. They concluded that further research on the SLM of aluminium should be primarily orientated towards new methods of controlling the oxidation process and disrupting oxide films formed within the components.

Just as oxide films are damaging to aluminium alloy castings, so they are to SLS/SLM processed parts made in aluminium alloys. However, the potential role of oxide films has not been elucidated in SLS/SLM processed aluminium alloy parts due to abundance of some defects such as porosity, cracking, and loss of alloying elements. It is expected that the potential role of oxide films will possibly be highlighted in SLS/SLM processing of aluminium alloys in the future, once these defects are eliminated.

#### *5.2.4 Loss of Alloying Elements*

High-power density employed in laser processing may cause selective vapourisation of alloying elements with low fusion points because of their higher equilibrium vapour pressure than aluminium [46, 183, 184]. According to Collur et al. [184], intrinsic vaporisation of alloying elements at the melt pool surface controls the overall vaporisation during laser processing while its mechanism of formation entails (i) transportation of vaporisation elements from the bulk to the surface of the molten pool; (ii) vaporisation of elements at the liquid/vapour interface; and (iii) transportation of the vaporised species into the surrounding gas phases.

Selective vaporisation of alloying elements leads to degradation of functional properties of laser processed parts. For example, vaporisation of Mg in laser processed aluminium alloys may result in the loss of precipitation strengthening, thereby, causing reduction in yield strength and hardness [183]; elongation and formability [184]; corrosion resistance and solidification cracking susceptibility [183]. The depletion of alloying elements also lead to scan track instability and high level of porosity in laser processed parts [46] thereby necessitating that appropriate measures be taken with a view to ensuring a reduction in vaporisation loss of alloying elements.

By controlling the beam power density distribution and adjusting the pulsing parameters during CW and PW laser processing respectively, the temperature of the molten pool can be regulated, thereby reducing the loss of alloying elements. The change in the chemical composition of the laser processed part is a function of the vaporisation rate and the volume of the molten pool [185, 186]. Although, alloying vaporisation rate increases with the dissipated energy density, the change in composition is most pronounced at low energy density levels due to small size, and the high surface-to-volume ratio, of the molten pool [185, 186]. Therefore, employing laser processing conditions combining medium or high power with high scanning rates is critical to avoiding alloying vaporisation [184]. Fluxing materials can also be used to compensate for the loss of alloying elements: however, no science-based measures are currently used to avoid alloying losses during SLS/SLM processing of aluminium alloys.

## 6 Mechanical Properties of SLS/SLM Fabricated Parts

From Table 10, it is evident that the SLS/SLM process is able to impart adequate mechanical properties to components produced from metal powders when compared to other manufacturing techniques [187-189]. To understand how mechanical properties of SLS/SLM processed parts vary with the fractional density, the effect of pores (porosity and pore shape) on the structural integrity (impact energy, fracture toughness, and fatigue strength) of P/M sintered parts will be discussed briefly. Thereafter, recent studies detailing the mechanical properties of SLS/SLM parts will be presented. Although, a sintered sample may attain full density; nevertheless, it may possess inferior mechanical properties as a result of microstructural defects, the presence of inclusions such as oxides (Fig. 52). Pores reduce the effective load carrying capacity of a material and act as stress concentrators and effective crack initiation sites which affect hardness, tensile properties, and ductility [187]. Therefore, a sample with residual microstructural porosity would be expected to be weaker than fully dense bulk material. Interestingly, mechanical properties of sintered parts are sensitive to pore shape and placement. Smooth pores at large spacings are noted to be less detrimental than small, closely spaced pores (Fig. 53). The undesirable influence of pores on ductility is as a consequence of crack initiation at the pores. Therefore, aside from the effect of pore volume on ductility, there is a further sensitivity to pore shape.

**Table 10**

Comparative analysis of parts fabricated by SLS/SLM and other traditional production processes [188, 189].

<b>Techniques</b>	<b>Min. mass (g)</b>	<b>Max. mass (g)</b>	<b>Min. section Thickness (mm)</b>	<b>Shape complexity</b>	<b>Tooling</b>	<b>Lead time</b>	<b>Typical Tensile Strength (M Pa)</b>
SLS/SLM	5	5,000	0.5	5 Highest	Nil	Days	100- 230
Machining	1	No limit	0.1	4 High	Nil	Days to weeks	100- 600
Investment casting	5	30,000	0.5	4 High	Simple	Days to weeks	100- 280
Sand casting	50	No limit	3	3 Fair	Moderate	Weeks	130- 480
Powder metallurgy	1	1,000	1.5	3 Fair	Complex	Months	130- 400
Die casting	<50	50,000	1	2 Low	Complex	Months	200- 360
Closed die forging	10	No limit	3	2 Low	Complex	Months	330- 660
Extrusion	1,000	No limit	1	1 Lowest	Moderate	Weeks	100- 400

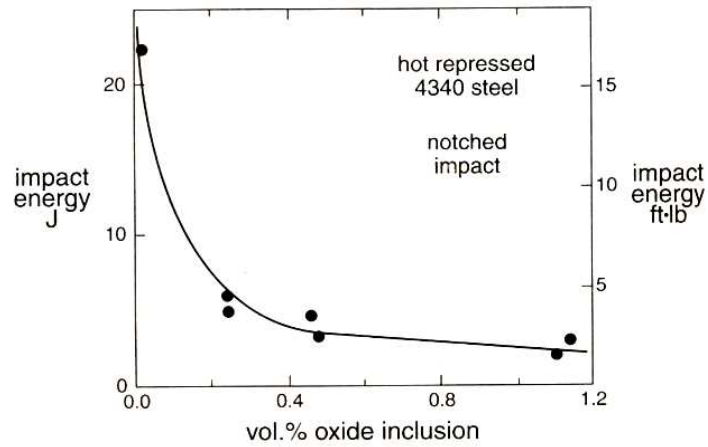


**Fig. 52.** Impact energy as a function of the oxide inclusion content in a hot-repressed 4340 steel, showing the detrimental effect of a small level contamination [113].

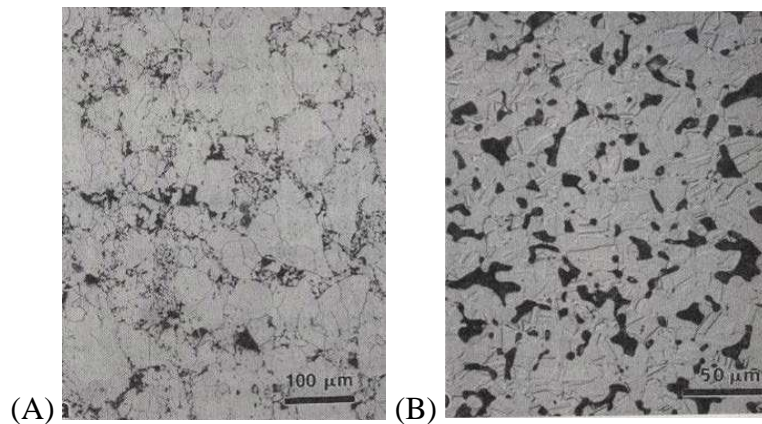


**Fig. 53.** The pores (dark spots) in these two sintered steels vary in shape and size, largely due to differences in sintering cycles. The arrangement of pores outlining the particles in (A) is detrimental to final properties, while the smooth pore structure evident in (B) is more desirable [113].

On the basis of the above discourse, German [113] and Grayson et al. [190] inferred that the shape, spacing, size, and placement of pores contribute to the significant variation in ductility observed in P/M materials. German [113] noted that with a porosity level greater than 15%, ductility is often negligible. Grayson et al. [190] characterised the fatigue behaviour of unreinforced pressed and sintered aluminium alloys by examining aspects of crack initiation and growth. They discovered that crack initiation occurred at surface or sub-surface pores and pore clusters with the veins of oxide observed on fatigue fracture surfaces. The presence of the veins of oxide was attributed to pre-existing microstructural features arising from the residue of the alumina film on the aluminium powder particles. Moreover, Upadhyaya [191] established that, for a common P/M alloy (201 AB), the tensile strength for a compaction pressure of 110 MPa and sintered density of  $2.53 \text{ g/cm}^3$  (approximately 9vol% porosity) was 169 MPa. When the sintered density was increased to  $2.70 \text{ g/cm}^3$  (6% higher density), the tensile strength increased by ~25% to 209 MPa.

Furthermore, German [113] highlighted the role of porosity in low-alloy (Ni-Mo-C) steels; for instance, the fatigue endurance strength for hot forged material having 0% porosity is 650 MPa, whilst the value for the same alloy produced by metal injection moulding (3% porosity) is 575 MPa and die compaction (12% porosity) is 390 MPa. In the formation of fatigue cracks and their propagation through the microstructure, pores play a significant role. Given the condition of dynamic loading, the crack grows ever so slightly on each stress cycle, eventually reaching a point where fracture takes place [113]. The nature of the final failure may be ductile or brittle.

An understanding of the nature of the failure demands an accurate interpretation of the microstructure and of the fracture surface [192]. The presence of dimples on the SEM fractured surfaces is an indication of ductile failure while brittle fracture is characterised by cleavage with each fractured grain flat and differently oriented, thereby giving a “crystalline” or “rock candy” appearance to the fracture surface [192]. The impact energy and fracture toughness are also sensitive to pores. The impact energy is the energy needed to fracture a sample, while the fracture toughness indicates the energy required for the crack growth in an already defective structure [113]. Porous P/M parts are poor in impact toughness and fracture toughness tests. In the subsequent section, the mechanical behaviour of SLS/SLM processed parts is presented.

### *6.1 Hardness and Wear Resistance*

Fig. 54A illustrates the optimum hardness of 145 HV<sub>0.1</sub> obtained when a scanning rate of 2,500 mm/s was employed for SLM processing of AlSi10Mg samples at high scanning velocities and laser powers as investigated by Buchbinder et al. [24]. The outcome of this study showed that the hardness of the SLM processed AlSi10Mg samples was not influenced by the adoption of high scan rates and laser power in contrary to earlier finding in Buchbinder et al. [193] where an increase in hardness with increasing scanning velocity had been demonstrated.

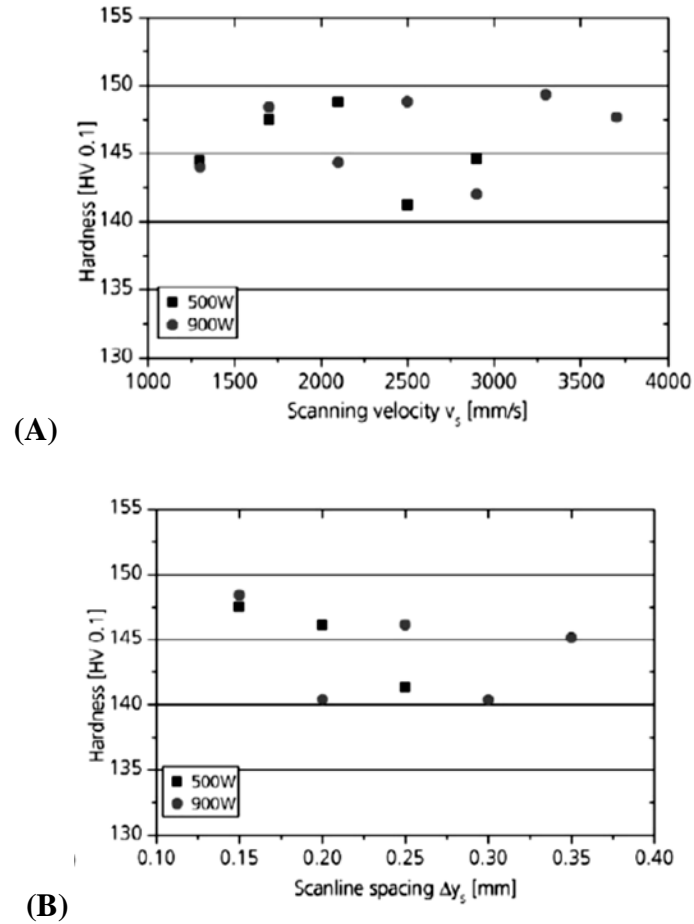


**Fig. 54.** Hardness of SLM processed AlSi10Mg samples depending on (A) scan rate (B) scan spacing [24].

Figure 54B also shows the variation of hardness of SLM processed AlSi10Mg parts with different scan spacings as measured by Buchbinder et al. [24]. It is evident that the resulting hardness of samples is independent of the adopted range of scan spacing and reaches an optimum value of 148 HV<sub>0.1</sub> at a scan spacing of 0.15mm (Figure 54B). Optimum hardness value reported for SLM processed AlSi10Mg parts was found to be twice the hardness value obtained for die

cast AlSi10Mg components according to EN 1706 standards and this could be attributed to high solidification rates resulting from the adoption of high scanning velocities.

According to Mercelis & Kruth [194] and Gu & Meiners [195], residual stresses are not always disadvantageous in SLM fabricated parts because its retention at a reasonable level enhances the part's hardness provided a sufficiently high densification without the formation of cracks or pores could be achieved. Moreover, the rapid solidification effect imparted on the as-processed parts by the SLM which results in grain refinement of microstructure is another reason that could be attributed to increased hardness of SLM fabricated parts. Consequently, this lowers the part's co-efficient of friction (COF), thereby improving the wear resistance of SLM fabricated parts. Gu and co-researchers [176] demonstrated how variation of process parameters altered the phase constitutions and microstructural characteristics of SLM fabricated commercial pure (CP) Ti parts with the variation in hardness and wear rate obtained for the parts attributed to this effect.

For example, when Gu et al. [176] employed scanning rate of  $100 \text{ mm s}^{-1}$  for the SLM processing of commercially pure (CP) Ti parts, the average COF reached a high value of 1.41, resulting in a considerably elevated wear rate of  $1.19 \times 10^{-3} \text{ mm}^3 \text{ N}^{-1} \text{ m}^{-1}$ . The worn surface obtained at  $100 \text{ mm s}^{-1}$  primarily consisted of parallel, deep grooves representing abrasion wear with the loose fragments at the edges of grooves revealing the local severe deformation and plowing of the surface during sliding. Moreover, some irregular shaped debris in the form of particles was also observed on the wear surface (Fig. 55A). Upon increasing the scanning rate to

200 mm s<sup>-1</sup>, the worn surface showed much shallower grooves, free of any loose abrasive fragments (Fig. 55B), thereby reducing the mean COF and attendant wear rate to 1.16 and 8.82 x 10<sup>-4</sup> mm<sup>3</sup> N<sup>-1</sup> m<sup>-1</sup>, respectively. Interestingly, both the co-efficient of friction (0.98) and wear rate (8.43 x 10<sup>-4</sup> mm<sup>3</sup> N<sup>-1</sup> m<sup>-1</sup>) of CP Ti parts were minimised at the optimum scanning rate of 300 mm s<sup>-1</sup> as a consequence of very high hardness of 3.89GPa imparted on the parts.

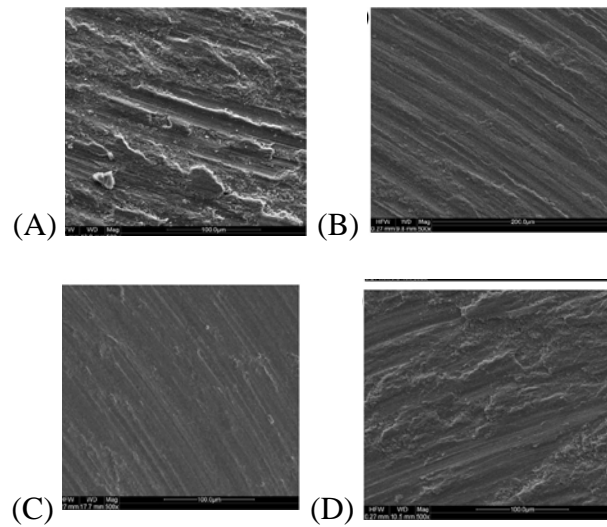


**Fig. 55.** SEM images showing characteristic morphologies of worn surfaces of SLM-processed Ti parts at: (A) 900 J m<sup>-1</sup>, 100 mm s<sup>-1</sup>; (B) 450 J m<sup>-1</sup>, mm s<sup>-1</sup>; (C) 300 J m<sup>-1</sup>, 300 mm s<sup>-1</sup>; (D) 225 J m<sup>-1</sup>, 400 mm s<sup>-1</sup> [176].

Similar to Jain et al. [196], the formation of an adherent, plastically smeared tribolayer (Fig. 55C) on the worn surface contributed to the enhancement of wear performance at the instance scanning rate was optimised. Analysis of findings from the work of Gu et al. [176] implies that the mechanism of material removal during sliding changes from abrasion (Fig. 55A) to adhesion of the tribolayer (Fig. 55C) for SLM fabricated CP Ti part with the transition

phenomena favouring the reduction in wear rate after sliding. When a higher scanning rate of  $400 \text{ mm s}^{-1}$  was adopted, although the localized formation of tribolayer was still observed on the worn surface, severe spalling and delamination of the tribolayer occurred (Fig. 55D). Both the COF and the wear rate were found to have increased significantly to 1.29 and  $1.08 \cdot 10^{-4} \text{ mm}^3 \text{ N}^{-1} \text{ m}^{-1}$  respectively. According to Gu et al. [176], comparative analysis of the phase constitution, densification kinetics, and microstructural properties of SLM fabricated CP Ti parts reveals that limited hardness and wear performance of the part processed at a low scan speed is ascribed to insufficient densification rate due to the formation of thermal microcracks; and the formation of relatively coarsened grains. For parts processed at a higher scan rate, although the formation of considerably refined martensitic  $\alpha'$  phase should favour an improvement in hardness and wear property, the undesirable densification kinetics of the powder due to the presence of interlayer micropores weakens the ultimate performance of the as-processed Ti part. In conclusion, they stated that the applied SLM conditions for various Ti samples exerted a significant influence upon obtainable hardness and wear performance.

Chlebus et al. [197] reported the effect of build orientation (x, y, and z-directions) on the hardness of SLM processed Ti—6Al—7Nb alloy. Their study revealed that the larger the specimen area parallel to the built platform and the smaller the specimen height (measured in z direction), the higher the hardness as a consequence of the grain size of the primary  $\beta$  phase. However, lower hardness obtained for vertical specimens in comparison to hardness of horizontal ones was attributed to the larger  $\beta$  grain size, and consequently the longer and thicker  $\alpha'$  martensite laths. The implication of these outcomes is that differences in the surface area of

the layers initiated variation in the thermal history of the material, thereby altering the microstructural properties and consequently the hardness values.

## 6.2 Tensile Strength

Tensile strength “which is primarily dependent on fractional density” exhibits similar trends to the variation of sintered density with respect to scan speed and laser power (Fig. 56). Besides the fractional density, the strength of SLS/SLM processed samples also depends on various powder characteristics such as particle size and distribution, and particle shape, alloying element e.t.c. As observed in other studies, higher SLS/SLM part densities were obtained by using a lower layer thickness [50, 94]. However, the minimum layer thickness that can be successfully employed is determined by various factors and most importantly by the maximum particle size in the system, as discussed in Section 4.2.1.

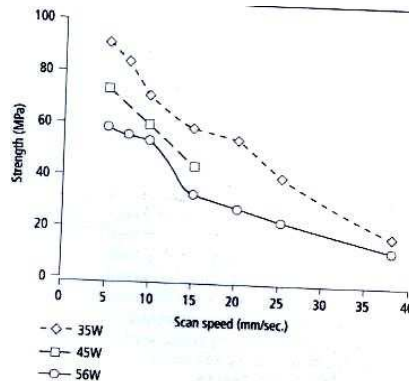


**Fig. 56.** Ultimate tensile strength of SLS-processed bronze-nickel parts as a function of scan speed and laser power [50].

Below a certain layer thickness, the roller mechanism tends to displace the previously sintered layers from their predetermined position, thus disturbing the geometry of the component. [50]. This problem is particularly serious during the early build-up of the component. In a study carried out by Agarwala et al. [50] on bronze (Cu-10%wt.Sn)-nickel powders having agglomerate particles as large as  $\sim 150 \mu\text{m}$ , it was discovered that lowering layer thickness from  $500 \mu\text{m}$  to  $250 \mu\text{m}$  resulted in an increase in ultimate tensile strength from approximately 35MPa to 60 MPa, irrespective of laser power or scan speed. The lower layer thickness resulted in improved sintering between layers thus advancing the part density. However, lowering the layer thickness to  $125 \mu\text{m}$  resulted in difficulty in spreading fresh layer of powders without disturbing previously sintered layers.

Agarwala and co-investigators [50] also observed that strength was considerably lower when bronze-nickel specimens were oriented and scanned in a longitudinal direction (40 MPa) in comparison to when they were oriented and scanned in the transverse direction (60 MPa). This is as a result of the short scan vector in the transverse scanning direction which resulted in better sintered part. Kruth et al. [103] demonstrated that short scan vectors cause the receipt of more localized net energy than a series of longer scan vectors because of the shorter time interval between successive pulses, minimising the temperature decay.

Chlebus et al. [197] found that the strategy of specimen building influences the tensile strength values with the horizontal specimens built in x and y orientation tensioned along the

longer scanning lines characterised by significantly smaller rigidity than the specimens built in the z-orientation. The modulus of the sample built in the z-orientation is 15% higher than the value given in literature for wrought Ti—6Al—7Nb alloy (105 GPa ) by Boyer et al. [198]; but 16% lower than in the case of specimens built in x and y orientation. Chlebus et al. [197] subsequently confirmed that specimens built at the direction of 45° to the long axis of a specimen have their Young's modulus to be of intermediate value. Chlebus and co-investigators [197] then noted that the differences in elasticity of the horizontally and vertically built specimens could be influenced by different distribution and level of residual stresses. Furthermore, samples built in the y direction have slightly higher yield and tensile strength values, and lower elongation in comparison to samples built in the x-direction. Since the orientation of pores and the solidification direction with respect to the tension direction was identical in both x- and y- orientations, the influence of built orientation can be related to the distribution of residual stresses. The drastically low tensile strength values of the z- direction built specimens in comparison to the x- and y- built orientation are undoubtedly related to the build defects (pores), with surface developed in the x–y plane, perpendicular to the specimen axis, consequently pulled apart by the tensile force; small tip radii of flat-shaped pores, which concentrate and magnify the applied stress; arrangement of layers perpendicular to the tension direction; larger number of pores (because of) resulting from a larger number of layers; and higher level of residual stresses in the z-axis direction. Furthermore, the tensile strength of SLM Ti6Al7Nb builds are higher than that of their counterpart wrought products and those having  $\alpha$ -equiaxial microstructure obtained via thermomechanical processing [199]. Finally, plastic elongations of SLM processed Ti6Al7Nb parts are small, similarly as found by Vandembroucke

& Kruth [200] and Murr et al. [201], and significantly (very) smaller in comparison to the elongations ranging from 7.5 to 12% for wrought alloys.

Comparison of the studies carried out by Agarwala *et al.* [50]; and Chlebus et al. [197] on bronze-nickel and Ti alloy components respectively to the outcome from Buchbinder et al. [24] who studied the role of build-up direction on the tensile strength of SLM processed AlSi10Mg parts confirms that samples with a layer orientation parallel to the tensile direction ( $0^\circ$ ) display the highest tensile strength ( $R_m = 420$  MPa), while those built with a layer orientation perpendicular to the applied load ( $90^\circ$ ) have the lowest strength ( $R_m = 360$  MPa) (Fig. 57). Buchbinder et al. [24] then concluded that the tensile strength obtained for SLM processed AlSi10Mg parts so far outreached the minimum tensile strength reported for die-cast AlSi10Mg part ( $R_m = 240$  MPa) in accordance with EN 1706 standard (Fig. 57).

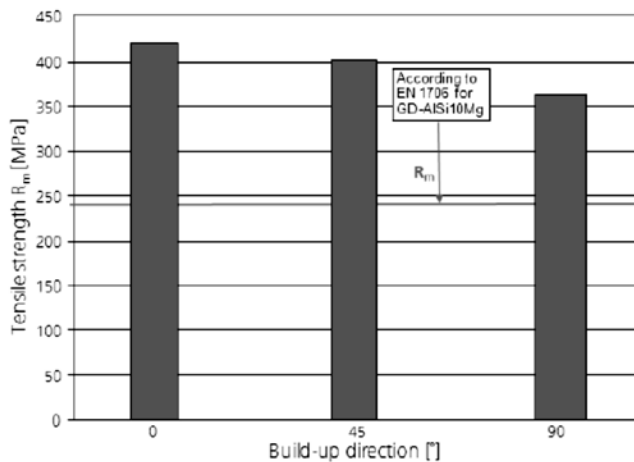


**Fig. 57.** Tensile strength depending on build up direction for SLM processed AlSi10Mg part [24].

Powder properties also exert significance influence on the tensile strength of SLM fabricated parts. For instance, Spierings et al. [202] explored the effect of three different powder granulations on the resulting tensile strength of the steel produced with a view to elucidating the variation in the mechanical properties as stated in the material data sheet of the machine producers. Their results show that two powders 1 and 2 having different particle size distributions, but of finer granulation, showed a comparable higher tensile strength; in contrast to the coarser powder 3 with lower tensile strength (Fig. 58). The behaviour of the powders was attributed to the fact that the coarser powder 3 resulted in bigger pores in comparison to finest powder 1 (Fig. 59) as a consequence of bigger particles and possibly a higher amount of hollow particles, which can be specific to the production process.

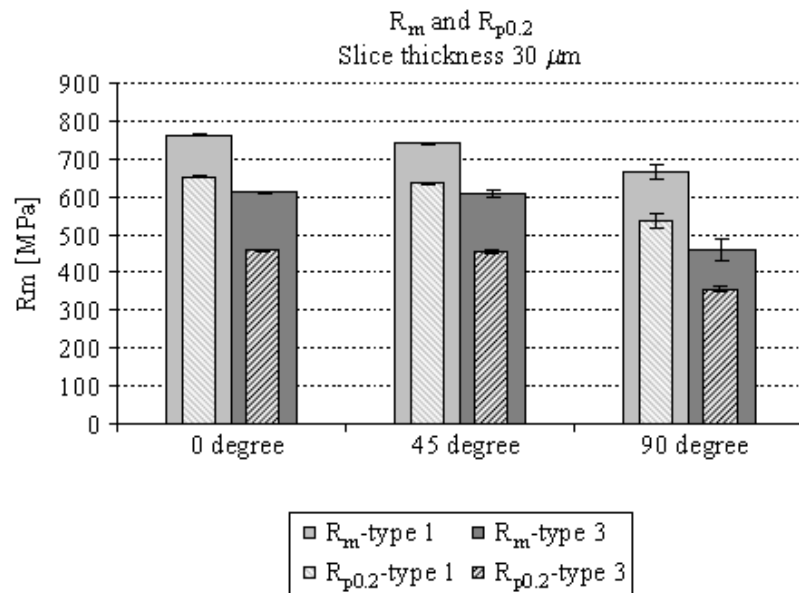


**Fig. 58.** Ultimate tensile strength  $R_m$  and yield strength at 0.2 per cent offset  $R_{p0.2}$  for 0°, 45° and 90° orientations for finer powder type 1 and coarsest powder type 3 [202].

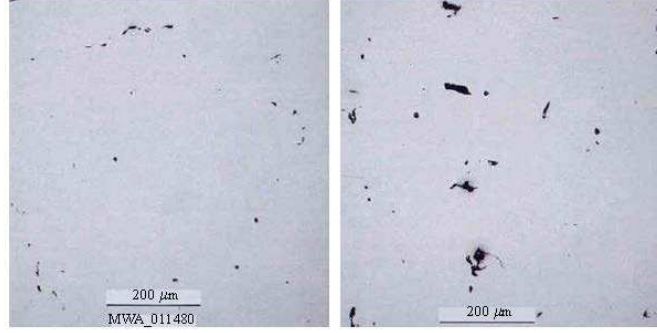


**Fig. 59.** Pore sizes of test cubes for finer powder type 1 (left) and coarse powder type 3 (right) for 30mm layers in  $0^\circ$  orientation [202].

Spierings *et al.* [202] reported that energy absorption requirement of bigger particles to achieve full melting is higher in comparison to smaller particles as depicted by Eq. (9):

$$\frac{E_{av}}{E_{need}} = \frac{A * I_0 * \pi * r^2}{\left(\frac{4}{3}\right)\pi * r^3 * \rho * (C_p \Delta T_m + L_m)} \quad (9)$$

$$= \frac{1}{r} * \frac{3AI_0}{4\rho(C_p \Delta T_m + L_m)} \quad (10)$$

where  $C_p$  and  $L_m$  are the specific or latent heat of fusion, respectively.  $A$  is the absorption coefficient of the powder material and  $I_0$  the intensity of the laser beam.

According to Spierings & Levy [203], SLM processing of coarse powders leads to generally higher effective powder layer thicknesses which reduces the amount of energy reaching the underlying surface. Consequently, the reduced thermal penetration depth prevents a reliable connection of the layers via re-melting of the underlying surface, thereby, resulting in more

inhomogeneous regions like cracks and incomplete fusion in the material. This effectively decrease the fracture toughness ( $K_{IC}$ ) value because the cracks have their long axis in parallel to the layer orientation so that external loads perpendicular to the layers open the cracks. This explains the reduction in the tensile strength of samples made of coarse powders and built in the vertical direction ( $90^\circ$ ). Spierings et al. [202] also established that increasing amount of coarser particles in a powder blend increased the ductility (Fig. 60), although this effect is less pronounced for higher layer thicknesses. They identified this as an evidence for a weaker bonding of the different layers. However, Spierings and co-researchers reasoned that the differences should be less distinct for laser sources with a higher laser beam quality, as for such beams deep penetration welding occurs while the size range of particles has to remain limited as for broader size distributions the mechanical strength is reduced. Meanwhile, in order to assure that coarser powders lead to a reduced re-melting of the underlying layers, additional investigations have to be undertaken.

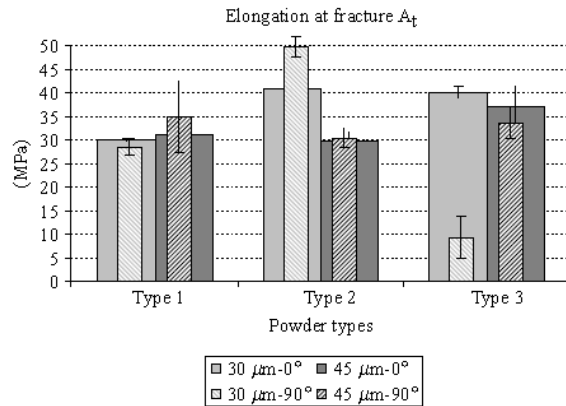


**Fig. 60.** Elongation at fracture  $A_t$  for finest powder type 1, fine powder type 2, and coarse powder type 3 [202].

While Dewidar and co-workers [56] adopted infiltration with bronze to improve the mechanical properties of high speed steel components fabricated via direct SLS, Uzunsoy & Chang [51] also carried out a comparative evaluation of the microstructure and mechanical properties of laser sintered low carbon stainless steel (316L) processed using three different copper alloy infiltrants. Uzunsoy & Chang [51] found the tensile fracture strength increased in the order of high tensile brass < bronze < cast aluminium manganese bronze.

### *6.3 Fatigue*

In similarity to the fatigue behaviour of conventional P/M sintered parts, the presence or absence of microstructural defects such as porosity or shrinkage cavities, dictate to a very great extent the fatigue life of SLS/SLM processed components. In SLS/SLM processed components, the occurrence of low melting porosity in between their layers reduces the effective load-bearing area perpendicular to the layers (z-direction) and causes stress concentration (notch effect), resulting in reduction of static and dynamic strength in the z-direction [30, 162, 169, 204-208]. Wang et al. [205, 206] investigated the crack path, initiation, and propagation of SLS processed FeNiCu-alloy via surface replication in four-point bending fatigue tests. They discovered that the fatigue behaviour was controlled by the complex layered structure with the pores on or under the surface being the preferable places for crack initiation. Furthermore, crack linkage and deflection occurred due to crack tip interaction with microstructure and sinter layers where microcracks initiated at pores adjacent to the advancing crack tip. According to Wang et al. [205, 206],

porosity has the most deteriorating influence on the fatigue strength of components whenever pore size and amount exceed certain threshold values.

Brandl et al. [30] employed this concept to elucidate the effects of varying powder bed temperature, peak hardening heat treatment, and build direction on the microstructure, and fatigue response of SLM processed AlSi10Mg alloy. It was established that the combination of heating the powder bed to 300 °C and post-built peak hardening treatment of AlSi10Mg parts led to the homogenisation of the microstructure of the parts via the formation of spheroidal interdendritic eutectic Si-particles and reduction of crack initiation and/or propagation, which eventually increased the fatigue resistance and the ductility [30]. However, Brandl and co-investigators reported that build direction has the least effect on the fatigue resistance of SLM processed AlSi10Mg parts. It is clear that heating the AlSi10Mg powder bed reduced the amount of metallurgical defects (e.g. cracks, porosity) because when the laser beam impinges on the already heated powder bed, the cooling rate is reduced, thus the distortion is reduced since fewer stresses are developed [30].

Analysis of the fracture behaviour of SLS/SLM parts shows that the crack initiation always started from the imperfections (pores, non-melted spots) at the surface or subsurface. This is generally expected due to the stress conditions and localized plastic deformation induced by surface discontinuities [209, 210]. According to Brandl et al. [30], the imperfections, however, can turn into a surface-notch after final machining and even promote crack initiation. Moreover, the peak-hardened samples showed dimples in the area of forced fracture (Fig. 62B)

in comparison to the as-built samples (Fig. 61B) which suggests ductile fracture behaviour. Brandl and co-investigators further reported that even though the peak-hardened sample demonstrated similar (ductile) forced fracture behaviour independent of the adopted powder bed temperature (30 °C, or 300 °C) or the building direction (0°, 90 °). In order to avoid such imperfections in SLM processed aluminium alloys, the process must therefore be improved upon by exploring the effects of scanning strategy of the laser beam, flow of inert gas, powder deposition etc.

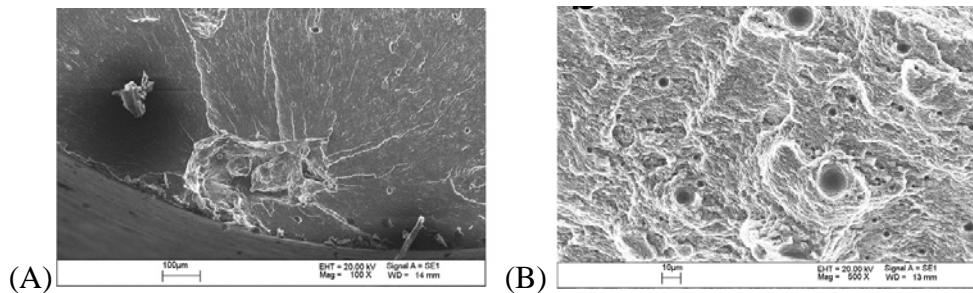


**Fig. 61.** Typical fracture surfaces of SLM processed AlSi10Mg parts (powder bed temperature of 300 °C / build direction of 0° / as-built): (A) crack initiation site and (B) area of forced fracture. [30].

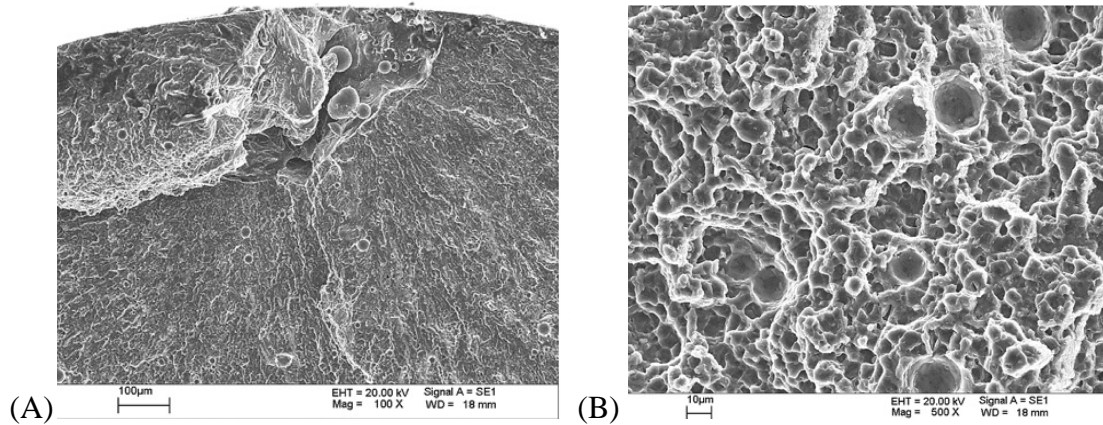


**Fig. 62.** Typical fracture surfaces of SLM processed AlSi10Mg parts (powder bed temperature of 300 °C / build direction of 0° / peak hardened): (A) crack initiation site and (B) area of forced fracture [30].

## 7. Perspectives on SLS/SLM Processing of Aluminium Alloy Powders

An analysis of the available literature on the SLS/SLM of metallic materials has revealed that aluminium, an engineering material in very high demand but which has not been extensively investigated by the SLS/SLM manufacturing method to explore the possibilities it offers for engineering applications. Therefore, SLS/SLM will be increasingly employed for fabricating high quality, low cost, repeatable, and reliable aluminium alloy parts in automotive, aerospace, and aircraft industries since it aids manufacturing businesses engaging in the fabrication of aluminium parts to deliver their new customised products more quickly and gain more consumer markets for their products. To date, the effects of the SLS/SLM process and powder parameters on the physical, mechanical and microstructural properties of aluminium powders and its alloys are yet to be fully proven. However, the aluminium powder is known to be uniquely bedevilled

with a tenacious surface oxide film which is difficult to avoid during SLS/SLM processing and therefore tends to produce processing problems and metallurgical defects. It is this lack of understanding of the effect of process and powder parameters on the processing and performance of SLS/SLM fabricated aluminium alloy components that has been addressed in this review in order to provide a basis for follow-on- research that leads to the development of high productivity of SLS/SLM processed aluminium alloy parts.

## 8. Conclusions

Consolidation regimes associated with SLS/SLM of aluminium alloys have been identified. The variants of SLS/SLM process of aluminium alloys have been categorised on the basis of material component system, type of laser employed for consolidation, the intensity of the specific laser energy input dissipated on the powder bed, as well as laser induced *in-situ* chemical reaction for fabricating aluminium alloy-based composites. Knowledge of these variants provides basic understanding of overcoming associated challenges of fabricating aluminium alloy powders for various technological applications via the SLS/SLM process. Available literature on SLS/SLM, powder metallurgy (P/M) sintering, and pulsed electric current sintering (PECS) of aluminium and its alloys were evaluated with a view to gaining useful insights especially in the aspect of alloying effect in disrupting the surface oxide film barrier to sintering or melting; liquid phase sintering (LPS); and alloying design suitable for the SLS/SLM process of aluminium powders. This led to highlighting the importance of reducing the oxide content of aluminium and its alloys during SLS/SLM processing. Provided oxide levels are low and adequate amount of liquid phase is available for filling all inter-particle pores completely,

components with inter-particulate bonding exhibiting pore free microstructure across the layers are obtainable by SLS process.

Furthermore, an extensive analysis of the available literature on the direct SLS/SLM of metals has led to the recognition of the influential process parameters (processing atmosphere, laser processing parameters, layer thickness, and type of laser employed for the sintering process) and material properties (powder particle size and distribution, powder particle shape, apparent and tapping densities, powder flowability, chemical composition, and liquid phase forming additives). All the process and powder parameters reported above have been shown throughout the literature as having strong influences on the properties of metallic powdered parts fabricated via SLS/SLM with their effects being linked to what impact each has over the wetting conditions between the layers, density, surface roughness, dimensional accuracy, surface morphology, microstructure and mechanical properties.

## **Acknowledgement**

Dr. Eyitayo Olatunde Olakanmi wishes to acknowledge the Commonwealth Scholarship Commission in the UK for the sponsorship of this study at the Institute for Materials Research, University of Leeds. Special thanks to the Federal University of Technology, Minna, Nigeria for granting the study leave to carry out this study at Leeds University. Moreover, the insightful discussions held with Dr. Peter Fox of the University of Liverpool during my Ph.D viva and Mr Herman Burger of the Laser Materials Processing Group of the National Laser Centre, Pretoria, South Africa are highly appreciated.

## References

- [1] Polmear IJ. Light Alloys: metallurgy of the light metals. 3rd ed. London: Arnold; 1995.
- [2] Cam G, Kodak M. Progress in joining of advanced materials. Int Mater Rev 1998;43:1-44.
- [3] Mondolfo LF. Aluminium Alloys: Structure and Properties. London: Butterworths; 1976.
- [4] Bias CT. In: Olsen FO editor, Hybrid laser-arc welding, Woodhead Publishing Ltd: CRC Press; 2009, p. 216-69.
- [5] Niu HJ, Chang ITH. Selective laser sintering of gas atomized M2 high speed steel powder. J Mater Sci 2000;35:31-38.
- [6] Asgharzadeh H, Simchi A. Effect of sintering atmosphere and carbon content on the densification and microstructure of laser-sintered M2 high-speed steel powder. Mater Sci Eng A 2005;403(1-2):290-298.
- [7] Morgan R, Papworth A, Sutcliffe C, Fox P, O'Neill W. High density net shape components by direct laser re-melting of single-phase powders. J Mater Sci 2002;37:3093-3100.
- [8] Gu DD, Meiners W, Wissenbach K, Poprawe R. Laser additive manufacturing of metallic components: materials, processes and mechanisms. Int Mater Rev 2012;57:133-64.
- [9] Weiss LE. Process overview. <[http://www.wtec.org/loyola/rp/02\\_01.htm](http://www.wtec.org/loyola/rp/02_01.htm)> [accessed 30.09.12].
- [10] Liu ZH, Zhang DQ, Sing SL, Chua CK, Loh LE. Interfacial characterization of SLM parts in multi-material processing: Metallurgical diffusion between 316L stainless steel and C18400 copper alloy. Mater Characterization 2014;94:116-125.

- [11] Abdul Aziz MS, Ueda T, Furumoto T, Abe S, Hosokawa A, Yassin A. Study on machinability of laser sintered materials fabricated by layered manufacturing system: Influence of different hardness of sintered materials. In: *Procedia CIRP* (Volume 4) of the 3rd CIRP Conference on Process Machine Interactions (3rd PMI), Nagoya, Japan; 2012. p 79 – 83.
- [12] Wits WW, Weitkamp SJ, van Es J. Metal additive manufacturing of a high-pressure micro-pump. In: *Procedia CIRP* (Volume 7) of the Forty Sixth CIRP Conference on Manufacturing Systems, Sesimbra, Portugal; 2013. p 252 – 257.
- [13] Calignano F, Manfredi D, Ambrosio EP, Biamino S, Pavese M, Fino P. Direct fabrication of joints based on direct metal laser sintering in aluminum and titanium alloys. In *Procedia CIRP* (Volume 21) of the 24th CIRP Design Conference, Milan, Italy; 2014. p 129 – 132.
- [14] Das S, Wohlert M, Beaman JJ, Bourell DL. Producing metal parts with selective laser sintering/hot isostatic pressing. *JOM* 1998;50(12):17-20.
- [15] Das S, Wohlert M, Beaman JJ, Bourell DL. Processing of titanium net shapes by SLS/HIP. *Mater Des* 1999;20:115-21.
- [16] Stoodley MA, Abbott JR, Simpson A. Titanium cranioplasty using 3-D computer modelling of skull defects. *J Clin Neur Sci* 1996;3(2):149-55.
- [17] Hayashi T, Maekawa K, Tamura M, Hanyu K. Selective laser sintering method using titanium powder sheet toward fabrication of porous bone substitutes. *JSME Inter J* 2005;A 48(4):369-375.
- [18] Hollander DA, von Walter M, Wirtz T, Sellei R, Schmidt-Rohlfing B, Paar O, et al. Structural, mechanical, and in vitro characterisation of individually structured Ti-6Al-4V

produced by direct laser forming. *Biomaterials* 2006;27:955-63.

[19] Kanazawa M, Maiko M, Minakuchi S, Nomura N. Fabrication of titanium alloy frameworks for complete dentures by selective laser melting. *J Prosth Dent* 2014;112(6):1441-47.

[20] Wauthle R, van der Stok J, Yavari SA, Van Humbeeck J, Kruth J-P, Zadpoor AA, et al. Additively manufactured porous tantalum implants. *Acta Biomater* 2014 doi: 10.1016/j.actbio.2014.12.003 (Article in press).

[21] Vasquez M, Cross J, Hopkinson N, Haworth B. Developing new laser sintering materials for snowboarding applications. In *Procedia Engineering* (Volume 34) of the 9th Conference of the International Sports Engineering Association (ISEA), Lowell, Massachusetts; 2012. p 325–30.

[22] Ardila LC, Garcíandia F, González-Díaz JB, Álvarez P, Echeverria A, Petite MM, et al. Effect of IN718 recycled powder reuse on properties of parts manufactured by means of Selective Laser Melting. In *Physics Procedia* (Volume 56) of the 8th International Conference on Photonic Technologies LANE, Fürth, Germany; 2014. p 99 – 107.

[23] Seyda V, Kaufmann N, Emmelmann C. Investigation of aging processes of Ti-6Al-4V powder material in laser melting. In *Physics Procedia* (Volume 39) of the 7th International Conference & Exhibition on Photonic Technologies LANE, Fürth, Germany; 2012. p 425 – 31.

[24] Buchbinder D, Schleifenbaum H, Heidrich S, Meiners W, Bültmann J. High power selective laser melting (HP SLM) of aluminium parts. In *Physics Procedia* (Volume 12A) of the Sixth International WLT Conference on Lasers in Manufacturing, Munich ICM, Germany; 2012. p 271–78.

[25] Cooper DE, Stanford M, Kibble KA, Gibbons GJ. Additive Manufacturing for product improvement at Red Bull Technology. *Mater Des* 2012;41:226–30.

- [26] Wang CY. Rapid Manufacturing: overview. <<http://www.csa1.co.uk/discoveryguides/rapidman/overview.php>> [accessed 30.09.12].
- [27] Louvis E, Fox P, Sutcliffe CJ. Selective laser melting of aluminium components. *J Mater Process Technol* 2011;211:275–84.
- [28] Olakanmi EO, Cochrane RF, Dalgarno KW. Densification mechanism and microstructural evolution in selective laser sintering of Al-12Si Powders. *J Mater Process Technol* 2011;211:113-121.
- [29] Olakanmi EO, Dalgarno KW, Cochrane RF. Laser sintering of blended Al-Si powders. *Rapid Prototyp J* 2012;18:109–119.
- [30] Brandl E, Heckenberger U, Holzinger V, Buchbinder, D. Additive manufactured AlSi10Mg samples using selective laser melting (SLM): Microstructure, high cycle fatigue, and fracture behaviour. *Mater Des* 2012; 34:159–69.
- [31] Dadbakhsh S, Hao L. Effect of Al alloys on selective laser melting behaviour and microstructure of in situ formed particle reinforced composites. *J Alloy Comp* 2012; 541:328–334.
- [32] Dadbakhsh S, Hao L. In-situ formation of particle reinforced Al matrix composite by selective laser melting of Al/Fe<sub>2</sub>O<sub>3</sub> powder mixture. *Adv Eng Mater* 2012;14(1-2):45-48.
- [33] Dadbakhsh S, Hao L, Jerrard PGE, Zhang, DZ. Experimental investigation on selective laser melting behaviour and processing windows of in situ reacted Al/Fe<sub>2</sub>O<sub>3</sub> powder mixture. *Powder Technol* 2012; 231:112–121.

- [34] Dadbakhsh S, Hao L. Effect of Layer Thickness in Selective Laser Melting on Microstructure of Al/5 wt.%Fe<sub>2</sub>O<sub>3</sub> Powder Consolidated Parts. *The Scient World J* 2014;2014, doi:10.1155/2014/106129
- [35] Ahuja B, Karg M, Nagulin KY, Schmidt M. Fabrication and characterization of high strength Al-Cu alloys processed using laser beam melting in metal powder bed. In *Procedia* (Volume 56) of the 8th International Conference on Laser Assisted Net Shape Engineering LANE, Fürth, Germany; 2014. p 135 – 146.
- [36] Li XP, Kang CW, Huang H, Zhang LC, Sercombe TB. Selective laser melting of an Al<sub>86</sub>Ni<sub>6</sub>Y<sub>4.5</sub>Co<sub>2</sub>La<sub>1.5</sub> metallic glass: Processing, microstructure evolution and mechanical properties. *Mater Sci Eng A* 2014;606:370–79.
- [37] Kenzari S, Bonina D, ubois J-M, Fournée V. Additive manufacturing of lightweight, fully Al-based components using quasicrystals. *J Mater Process Technol* 2014;214:3108–11.
- [38] Wang XJ, Zhang LC, Fang MH, Sercombe TB. The effect of atmosphere on the structure and properties of a selective laser melted Al–12Si alloy. *Mater Sci Eng A* 2014;597:370–75.
- [39] Gu D, Wang H, Chang F, Dai D, Yuan P, Hagedorn Y-C. et al. Selective laser melting additive manufacturing of TiC/AlSi10Mg bulk-form nanocomposites with tailored microstructures and properties. In *Procedia* (Volume 56) of the 8th International Conference on Photonic Technologies LANE, Fürth, Germany; 2014. p 108 – 16.
- [40] Olakanmi EO. Selective laser sintering/melting (SLS/SLM) of pure Al, Al–Mg, and Al–Si powders: Effect of processing conditions and powder properties. *J Mater Process Technol* 2013;213:1387–1405.

- [41] Read N, Wang W, Essa K, Attallah MA. Selective laser melting of AlSi10Mg alloy: Process optimisation and mechanical properties development. *Mater Des* 2015;65:417–24.
- [42] Li XP, Kang CW, Huang H, Sercombe TB. The role of a low-energy–density re-scan in fabricating crack-free  $\text{Al}_{85}\text{Ni}_5\text{Y}_6\text{Co}_2\text{Fe}_2$  bulk metallic glass composites via selective laser melting. *Mater Des* 2014;63:407–11.
- [43] Ghosh SK, Bandyopadhyay K, Saha P. Development of an in-situ multi-component reinforced Al-based metalmatrix composite by direct metal laser sintering technique — Optimization of process parameters. *Mater Charact* 2014;93:68-78.
- [44] Cao X, Wallace W, Immarrigeon J\_P, Poon C. Research and progress in laser welding of wrought aluminium alloys. I. Laser welding Processes. *Mater Manuf Process* 2003; 18:1–22.
- [45] Olakanmi EO. Direct selective laser sintering of aluminium alloy powders. PhD thesis, University of Leeds, Leeds. 2008.
- [46] Das S. Physical aspects of process control in selective laser sintering of metals. *Adv Eng Mater* 2003;5(10):701-11.
- [47] Kruth J-P, Levy G, Klocke F, Childs THC. Consolidation phenomena in laser and powder-bed based layered manufacturing. *Ann CIRP* 2007;56(2):730-59.
- [48] Shellabear M, Nyrhilä O. Advances in materials and properties of direct metal laser-sintered parts. [http://www.rm-platform.com/index.php?option=com\\_docman&task=cat\\_view&gid=24&Itemid=38](http://www.rm-platform.com/index.php?option=com_docman&task=cat_view&gid=24&Itemid=38) [accessed 30.09.12]
- [49] Kruth J-P, Mercelis P, Van Vaerenbergh J, Froyen L, Rombouts M. Binding mechanisms in

selective laser sintering and selective laser melting. Rapid Prototyp J\_2005;11(1):26-36.

[50] Agarwala M, Bourell D, Beaman J, Marcus H, Barlow J. Direct selective laser sintering of metals. Rapid Prototyp J\_1995;1(1):26-36.

[51] Uzunsoy D, Chang ITH. The effect of infiltrant choice on the microstructure and mechanical properties of Rapidsteel\*2.0. Mater Lett 2005;59(22):2812-2817.

[52] Simchi A, Pelzoldt F, Pohl H. Direct metal laser sintering: materials considerations and mechanisms of particle bonding. Int J Powder Met. 2001;37(2):49-61.

[53] Sercombe TB, Schaffer GB. Rapid manufacturing of aluminium components. Sci 2003;301:1225-1227.

[54] Miani F. On the development of new metal powders for the selective laser sintering process. In: Proceedings of the third world congress on intelligent manufacturing processes & system, Cambridge, MA, USA; 2000. p 245-52

[55] Laoui T, Froyen L, Kruth JP. Effect of mechanical alloying on selective laser sintering of WC-9Co powder. Powder Met 1999;42(3):203-205.

[56] Dewidar MM, Dalgarno KW, Wright CS Processing conditions and mechanical properties of high-speed steel parts fabricated using direct selective laser sintering. Proc Inst Mech Eng Part B: J Eng Manuf 2003;217:1651-62.

[57] Tang Y, Loh, HT, Wong YS, Fuh JYH, Lu L, Wang X. Direct laser sintering of a copper-based alloy for creating three-dimensional metal parts. J Mater Process Technol 2003;140(1-3):368-72.

- [58] Dalgarno KW, Wright CS. Approaches to processing metals and ceramics through the laser scanning of powder beds- A review. *Powder Metall Prog* 2001;1(1): 70-79.
- [59] German RM. *Liquid phase sintering*. London: Plenum Press; 1985.
- [60] Tandon R, Johnson J. Liquid-phase sintering. In: Davis RJ, editor, *Powder metal technologies and applications*. Materials Park (OH): ASM International; 1998. p. 565-573.
- [61] Schaffer GB, Sercombe TB, Lumley RN. Liquid phase sintering of aluminium alloys. *Mater Chem Phys* 2001;67(1-3):85-91.
- [62] Gu D, Shen Y. WC-Co particulate reinforcing Cu matrix composites produced by direct laser sintering. *Mater Lett* 2006;60(29):3664-68.
- [63] Gu D, Shen Y. Effect of dispersion technique and component ratio on densification and microstructure of multi-component Cu-based metal powder in direct laser sintering. *J Mater Process Technol* 2007;182: pp.564-573.
- [64] Gu D, Shen Y. Influence of reinforcement weight fraction on microstructure and properties of submicron WC-Cop/Cu bulk MMCs prepared by direct laser sintering. *J Alloys Comp* 2007; 431:112-20.
- [65] Gu D, Shen Y. Direct laser sintered WC-10Co/Cu nanocomposites. *Appl Surf Sci* 2008;254 (13):3971-78.
- [66] Zhu HH, Fuh JYH, Lu L. Formation of Fe-Cu metal parts using direct laser sintering. *Proc IMechE Part C: J Mech Eng Sci* 2003;217(1):139-47.
- [67] Xie G, Ohashi O, Song M, Furuya K, Noda T. Behavior of oxide film at the interface

between particles in sintered Al powders by pulse electric-current sintering. Metall Mater Trans A 2003;34(3):699-703.

[68] Xie G, Ohashi O, Song M, Mitsuishi k, Furuya K. Reduction mechanism of surface oxide films and characterization of formations on pulse electric-current sintered Al–Mg alloy powders. Appl Surf Sci 2005;241, (1-2):102-06.

[69] Liu Z. Y, Sercombe TB, Schaffer GB The effect of particle shape on the sintering of aluminium Metall Mater Trans A 2007;38:1351-57.

[70] Zhu HH, Lu L, Fuh JYH, Wu CC. Effect of braze flux on direct laser sintering Cu-based metal powder. Mater Des 2006;27(2):166-70.

[71] Zhu HH, Fuh JH, Lu L. Microstructural evolution in direct laser sintering of Cu-based metal powder. Rapid Prototyp J 2005;11(2):74-81.

[72] Sercombe TB. Sintering of freeformed maraging steel with boron additions. Mater Sci Eng A\_2003;363:242-52.

[73] Chen XC, Xie JW, Fox P. Direct laser remelting of iron with addition of boron. Mater Sci Technol 2004;20:715-19.

[74] Sercombe TB, Schaffer GB. Freeform fabrication of functional aluminium prototypes using powder metallurgy. J Mater Sci 1999;34:4245-51.

[75] Sercombe TB, Schaffer GB. The effect of trace elements on the sintering of Al-Cu alloys. Acta Mater 1999;47(2):689-97.

[76] Schaffer GB, Huo SH, Drennan J, Auchterlonie GJ. The effect of trace elements on the

sintering of an Al-Zn-Mg-Cu alloy. *Acta Mater* 2001;49(14):2671-78.

[77] McPhee WAG, Schaffer GB, Drennan J. The effect of iron on liquid film migration and sintering of an Al-Cu-Mg alloy. *Acta Mater* 2003;51(13):3701-12.

[78] Delgado ML, Ruiz-Navas EM, Gordo, E, Torralba, JM. Enhancement of liquid phase sintering through Al-Si additions to Al-Cu systems. *J Mater Process Technol* 2005;162-163:280-85.

[79] MacAskill IA, Hexemer Jr RL, Donaldson IW, Bishop DP. Effects of magnesium, tin and nitrogen on the sintering response of aluminium powder. *J Mater Process Technol* 2010;210(15):2252-60.

[80] Gökçe A, Fındık F, Kurt AO. Microstructural examination and properties of premixed Al-Cu-Mg powder metallurgy alloy *Mater Charact* 2011;62:730-735.

[81] Gu D, Shen Y. Balling phenomena during direct laser sintering of multi-component Cu-based metal powder. *J Alloy Comp* 2007;432:163-66.

[82] Niu HJ, Chang ITH. Liquid phase sintering of M3/2 high speed steel by selective laser sintering. *Scripta Mater* 1998;39(1):67-72.

[83] Niu HJ, Chang ITH. Selective laser sintering of gas and water atomized high speed steel powders. *Scripta Mater* 1999;41(1):25-30.

[84] Niu HJ, Chang ITH. Instability of scan tracks of selective laser sintering of high speed steel powder. *Scripta Mater* 1999;41(11):1229-34.

[85] Zhu HH, Lu L, Fuh JYH. Influence of binder's liquid volume fraction on direct laser

sintering of metallic powder. Mater Sci Eng A 2004;**371**:170-77.

[86] Khan M, Dickens P. Selective laser melting (SLM) of gold (Au). Rapid Prototyp J 2012;18:81–94.

[87] Zhang B, Liao H, Coddet C. Effects of processing parameters on properties of selective laser melting Mg–9%Al powder mixture. Mater Des 2012;34:753–758.

[88] Gu D, Shen Y. Balling phenomena in direct laser sintering of stainless steel powder: metallurgical mechanisms and control methods. Mater Des 2009;30:2903-2910.

[89] German RM. Particle packing characteristics. Princeton, NJ: Metal Powder Industries Federation; 1989.

[90] Krol TA, Seidel C, Zaeh MF. Prioritization of process parameters for an efficient optimisation of additive manufacturing by means of a finite element method. In Procedia (Volume 12) of the 8th CIRP Conference on Intelligent Computation in Manufacturing Engineering, Ischia (Naples), Italy; 2013. P 169–74.

[91] Tolochko NK, Mozzharov SE, Laoui T, Froyen L. Selective laser sintering of single- and two-component metal powders. Rapid Prototyp J 2003;9(2):68-78.

[92] Gu D, Shen Y. Processing and microstructure of submicron WC-Co particulate reinforced Cu matrix composites prepared by direct laser sintering. Mater Sci Eng A 2006;435-436:54-61.

[93] Gu D, Shen Y, Wu X. Formation of a novel W-rim/Cu-core structure during direct laser sintering of W-Cu composite system. Mater Lett 2008;62:1765-68.

[94] Simchi A, Pohl H. Effect of laser sintering processing parameters on the microstructure and densification of iron powder. Mater Process Engr 2003;A359(1-2):119-28.

- [95] Chatterjee AN, Kumar S, Saha P, Mishra PK, Choudhury AR. An experimental design approach to selective laser sintering of low carbon steel. *J Mater Process Technol* 2003;136(1-3):151-57.
- [96] Ma M, Wang Z, Gao M, Zeng X. Layer thickness dependence of performance in high-power selective laser melting of 1Cr18Ni9Ti stainless steel. *J Mater Process Technol* 2015;215:142–50.
- [97] Sanz-Guerrero J, Ramos-Grez J. Effect of total applied energy density on the densification of copper–titanium slabs produced by a DMLF process. *J Mater Process Technol* 2008;202(1-3):339-46.
- [98] Su WN, Erasenthiran P, Dickens PM. Investigation of fully dense laser sintering of tool steel powder using a pulsed Nd:YAG laser. *Proc IMechE Part C: J Mech Eng Sci* 2003;217(1):127–38.
- [99] Hauser C, Childs THC, Dalgarno KW. Selective laser sintering of stainless steel 314S HC processed using room temperature powder beds. In: *Proceedings of the 10th Solid freeform fabrication symposium, Austin, Texas; 1999. p 273-80.*
- [100] Hauser C. Selective laser sintering of a stainless steel powder PhD thesis, University of Leeds, UK; 2003.
- [101] Xubin Su X, Yang Y. Research on track overlapping during Selective Laser Melting of powders. *J Mater Process Technol* 2012;212:2074–79.
- [102] Aboulkhair NT, Everitt NM, Ashcroft I, Tuck C. Reducing porosity in AlSi10Mg parts processed by selective laser melting. *Add Manuf* 2014;1–4:77–86.

- [103] Kruth J.-P, Froyen L, Van Vaerenbergh J, Mercelis P, Rombouts M, Lauwers B. Selective laser melting of iron-based powder. *J Mater Process Technol* 2004;149:616-22.
- [104] Xie W, Fox P, O'Neill W, Sutcliffe CJ. Effect of direct laser re-melting processing parameters and scanning strategies on the densification of tool steels. *J Mater Process Technol* 2005;170 (3):516-23.
- [105] Hauser C, Childs THC, Dalgarno KW, Eane RB. Atmospheric control during selective laser sintering of stainless steel 314S powder. In: *Proceedings of the 10th solid freeform fabrication symposium, Austin, TX; 1999. p 265-72.*
- [106] Schaffer GB, Hall BJ, Bonner SJ, Huo SH, Sercombe TB. The effect of the atmosphere and the role of pore filling on the sintering of aluminium. *Acta Mater* 2006;54(1):131-38.
- [107] Wu X, Sharman R, Mei J, Voice W. Direct laser fabrication and microstructure of a burn-resistant Ti alloy. *Mater Des* 2002;23:239-47.
- [108] Das S, Fuesting TP, Danyo G, Brown LE, Beaman JJ, Bourell DL. Direct laser fabrication of superalloy cermet abrasive turbine blade tips. *Mater Des* 2000;21:63-73.
- [109] Martin JM, Castro F. Liquid phase sintering of P/M aluminium alloys: effect of processing conditions. *J Mater Process Technol* 2003;143-144:814-21.
- [110] Schaffer GB, Hall BJ. The influence of atmosphere on the sintering of aluminium. *Metall Trans A* 2002;33(10):3279-84.
- [111] German RM. The importance of particle characteristics in powder injection moulding. *Rev Partic Mater* 1993;1:109-160.

- [112] German RM. Sintering theory and practice. New York: John Wiley & Sons; 1996.
- [113] German RM. Powder metallurgy of iron and steel. Chichester: John Wiley & Sons; 1998.
- [114] Lumley RN, Schaffer GB. The effect of solubility and particle size on liquid phase sintering. *Scripta Mater* 1996;35(5):589-95.
- [115] Lumley RN, Schaffer GB. The effect of additive particle size on the mechanical properties of sintered aluminium-copper alloys. *Scripta Mater* 1998;39(8):1089-94.
- [116] German RM, Bulger M. A model for densification by sintering of bimodal particle size distribution. *Inter J Powder Metall* 1992;28(3):301-11.
- [117] Simchi A. The role of particle size on the laser sintering of iron powder. *Metall Mater Trans B* 2004;35B:937-48.
- [118] Zhang DQ, Liu ZH, Cai QZ, Liu JH, Chua CK. Influence of Ni content on microstructure of W–Ni alloy produced by selective laser melting. *Int. J Refr Metals Hard Mater* 2014;45:15–22.
- [119] Simchi A. Direct laser sintering of metal powders: Mechanism, kinetics and microstructural features. *Mater Sci Eng A*. 2006;428(1-2):148-58.
- [120] Dinsdale AT, Quested PN. The viscosity of aluminium and its alloys- A review of data and models. *J Mater Sci* 2004;39(24):7221-28.
- [121] Geiger GH, Poirier DR. Transport phenomena in metallurgy. Wesley: Pearson Addison; 1973.
- [122] Park S-H, Hur B-H, Kim S-Y, Ahn D-K, Ha D-I. A study on the viscosity and surface tension for Al foaming and the effects of addition elements. In: Proceedings of the 65th world

foundry congress, Gyeongju, Korea; 2002. p 515-24.

[123] Olakanmi EO, Cochrane RF, Dalgarno KW. Spheroidisation and oxide disruption phenomena in direct Selective Laser Melting (SLM) of pre-alloyed Al-Mg and Al-Si powders. In: Supplemental Proceedings: (Volume I: Materials Processing and Properties: Materials Issues in Additive Powder-Based Manufacturing Processes Symposium) of the 2009 TMS Annual Meetings and Exhibition, San-Francisco, California; 2009. p 371-80.

[124] Williams C. CO laser processing - an overview. *Aircraft Eng Aero Technol* 1997;69(1):43-52.

[125] Lauwers B, Kruth, J-P, Froyen L, Laoui T. Comparison between Nd:YAG and CO2 laser for use with selective laser sintering of metal powders. In: Proceedings of the PHOTOMECH'99-Liège, Belgium; 1999. p 165-73.

[126] Tolochko NK, Khlopkov YV, Mozzharov SE, Ignatiev MB, Laoui T, Titov VI. Absorptance of powder materials suitable for laser sintering. *Rapid Prototyp J* 2000;6(3):155-61.

[127] Steen WM. *Laser materials processing*. London: Springer; 2003.

[128] Santos EC, Shiomi M, Osakada K, Laoui T. Rapid manufacturing of metal components by laser forming. *Inter J Mach Tools Manuf* 2006;46(12):1459-68.

[129] O'Neill W, Sutcliffe C.J, Morgan R, Landsborough A, Hon KKB. Investigation on multi-layer direct metal laser sintering of 316L stainless steel powder beds. *Ann CIRP* 1999;48(1):151-54.

[130] Fischer P, Locher M, Romano V, Weber HP, Kolosov S, Glardon R. Temperature measurements during selective laser sintering of titanium powder. *Inter J Mach Tools Manuf*

2004;44:1293-1296.

[131] Abe F, Osakada K, Shiomi M, Uematsu K, Matsumoto M. The manufacturing of hard tools from metallic powders by selective laser melting. *J Mater Process Technol* 2001;111:210-13.

[132] Reutzel EW. In: Olsen FO editor, *Hybrid laser-arc welding*, Woodhead Publishing Ltd: CRC Press; 2009, p. 1-27.

[133] Gisario A, Barletta M, Veniali F. Surface reconstruction of porous substrates in sintered bronze by cw-high power diode laser. *Opt Lasers Eng* 2012;50:1306–15.

[134] Zhuoxing G, Jiandong H, Zhenfeng Z. Laser sintering of Cu-Sn-C system P/M alloys. *J Mater Sci* 1999;34:5403-06.

[135] Ion JC. *Laser processing of engineering materials: principles, procedures and industrial applications*. London: Elsevier Butterworth Heinemann; 2005.

[136] Basu B, Date AW Rapid solidification following laser melting of pure metals—I. Study of flow field and role of convection. *Inter J Heat Mass Transf* 1992;35(5):1049-58.

[137] Basu B, Date AW. Rapid solidification following laser melting of pure metals—II: study of pool and solidification characteristics. *Inter J Heat Mass Transf* 1992;35(5):1059-67.

[138] Li Y, Gu D. Parametric analysis of thermal behavior during selective laser melting additive manufacturing of aluminum alloy powder. *Mater Des* 2014;63:856–67.

[139] Loretto MH, Godfrey AB, Hu D, Blenkinsop PA, Jones IP, Cheng TT. The influence of composition and processing on the structure and properties of TiAl-based alloys. *Intermetall* 1998;6( 7-8): 663-66.

- [140] Srivastava D, Hu D, Chang ITH, Loretto MH. The influence of thermal processing route on the microstructure of some TiAl-based alloys. *Intermetall* 1999;7(10):1107-12.
- [141] Nelson TW, Lippold JC, Mills MJ. Nature and evolution of the fusion boundary in ferritic-austenitic dissimilar weld metals, Part I – Nucleation and growth. *Weld J* 1999;78(10):329-37.
- [142] Savage WF, Nippes EF, Erickson JS. Solidification mechanisms in fusion welds. *Weld J* 1976;55(8):213-21.
- [143] [Grong Ø., Ed. (1997). Metallurgical Modelling of Welding (2nd Edition) Materials Modelling Series. London, The Institute of Materials.
- [144] Kou S. *Welding metallurgy*. New York: Wiley Interscience; 1987.
- [145] Savage WF. Solidification, segregation and weld imperfections. *Weld World* 1980;18(5-6):89–114
- [146] Savage WF, Lundin CD, Aronson AH. Weld metal solidification mechanisms. *Weld J* 1965;44(4):175-81.
- [147] Savage WF, Hrubec WJ. Synthesis of weld solidification using crystalline organic materials. *Weld J* 1972;51(5):260-71.
- [148] Savage WF, Aronson AH. Preferred orientation in the weld fusion zone. *Weld J* 1966;45(2):85-89.
- [149] Lippold JC, Clark WAT, Tumuluru M. An investigation of weld metal interfaces. In: Cieslak MJ, Perepezlo JH, Glicksman ME, editors *The metal science of joining*. Warrendale PA: The Minerals, Metals & Materials Society; 1992. p. 141–46.

- [150] Srivastava D, Chang ITH, Loretto MH. The effect of process parameters and heat treatment on the microstructure of direct laser fabricated TiAl alloy samples. *Intermetall* 2001;9:1003-13.
- [151] Arnberg L, Chai G, Backerud L. Determination of dendritic coherency in solidifying melts by rheological measurements. *Mater Sci Eng* 1993;A173(1-2):101-03.
- [152] Veldman NLM, Dahle AK, StJohn DH, Arnberg L. Dendrite coherency of Al-Si Cu alloys. *Metall Mater Trans A* 2001;32A(1):147-55.
- [153] Bartkowiak K, Ullrich S, Frick, T, Schmidt M. New Developments of Laser Processing Aluminium Alloys via Additive Manufacturing Technique. *Phys Proc* 2011;12:393–401.
- [154] Huang W-C, Chuang C-S, Lin C-C, Wu C-H, Lin D-Y, Liu S-H, et al. Microstructure-controllable laser additive manufacturing process for metal products. In *Physics Procedia* (Volume 56) of the 8th International Conference on Photonic Technologies LANE, Fürth, Germany; 2014. p 58–63.
- [155] Murali K, Chatterjee AN, Saha P, Palai R., Kumar S, Roy SK, et al. Direct selective laser sintering of iron-graphite powder mixture. *J Mater Process Technol* 2003;136:179-85.
- [156] Simchi A, Pohl H. Direct laser sintering of iron-graphite powder mixture. *Mater Sci Eng A* 2004;383(2):191-200.
- [157] Ferrar B, Mullen L, Jones E, Stamp R, Sutcliffe CJ. Gas flow effects on selective laser melting (SLM) manufacturing performance. *J Mater Process Technol* 2012;212:355–364.
- [158] Sercombe TB. On the sintering of uncompacted, pre-alloyed Al powder alloys. *Mater Sci Eng A* 2003;341(1-2):163-68.

- [159] Sercombe TB, Schaffer GB. On the role of magnesium and nitrogen in the infiltration of aluminium by aluminium for rapid prototyping applications. *Acta Mater* 2004;52(10):3019-25.
- [160] Sercombe TB, Schaefer GB. On the role of tin in the infiltration of aluminium by aluminium for rapid prototyping applications. *Scripta Mater* 2004;51(9):905-08.
- [161] Sercombe TB, Hopkinson N. Process shrinkage and accuracy during indirect laser sintering of aluminium. *Adv Eng Mater* 2006;8(4):260-64.
- [162] Kobryn PA, Moore EH, Semiatin SL. The effect of laser power and traverse speed on Microstructure, porosity, and build height in Laser-deposited Ti-6Al-4V. *Scripta Mater.* 2000; 43:299–305.
- [163] Monroy K, Delgado J, Ciurana J. Study of the pore formation on CoCrMo alloys by selective laser melting manufacturing process. In: *Procedia Engineering* (Volume 63) of The Manufacturing Engineering Society International Conference (MESIC), Zaragoza, Spain; 2013 p 361–69.
- [164] Fischer P, Roman V, Weber HP, Karapatis NP, Boillat E, Glardon R. Sintering of commercially pure titanium powder with a Nd:YAG laser source. *Acta Mater* 2003;51:1651-62.
- [165] Pastor M, Zhao H, DebRoy T. Pore formation during continuous wave Nd:YAG laser welding of aluminium for automotive applications. *Rev Metal* 2000;36:108-17.
- [166] King WE, Barth HD, Castillo VM, Gallegos GF, Gibbs JW, Hahn DE, et al. Observation of key hole-mode laser melting in laser powder-bedfusion additive manufacturing. *J Mater Process Technol* 2014;214:2915–25.

- [167] Campbell J. Casting. Oxford: Butterworth-Heinemann; 1991.
- [168] Cao X, Wallace W, Immarigeon J\_P, Poon C. Research and progress in laser welding of wrought aluminium alloys. II. Metallurgical microstructures, defects, and mechanical properties. Mater Manuf Process 2003; 18:23–49.
- [169] Thijs L, Verhaeghe F, Craeghs T, Van Humbeeck J, Kruth JP. A study of the microstructural evolution during selective laser melting of Ti-6Al-4V. Acta Mater 2010;58:3303–3312.
- [170] Cieslak MJ, Fuerschbach PW. On the weldability, composition, and hardness of pulsed and continuous Nd:YAG laser welds in aluminium alloys 6061, 5456, and 5086. Metall Trans B 1988;19B:319-33.
- [171] Jones IA, Riches ST, Yoon JW, Wallach ER. Laser welding of aluminium alloys. TWI J 1998;7:421-81.
- [172] Liu R, Dong Z, Pan Y. Solidification crack susceptibility of aluminum alloy weld metals. Trans. Nonferrous Met Soc China 2006;16:110-16.
- [173] Dudas JH, Collins FR. Preventing weld cracks in high-strength aluminium alloys. Weld J 1966;45:241S-249S.
- [174] Sreeja Kumari SS, Pillai RM, Rajan TPD, Pai BC. Effects of individual and combined additions of Be, Mn, Ca and Sr on the solidification behaviour, structure and mechanical properties of Al-7Si-0.3Mg-0.8Fe alloy. Mater Sci Eng A 2007;460–461:561–573.

- [175] Zhao H, White DR, DebRoy T. Current issues problems in laser welding of automotive aluminium alloys. *Int Mater Rev* 1999;44:238-266.
- [176] Gu D, Hagedorn Y-C, Meiners W, Meng G, João R, Batista S, et al. Densification behaviour, microstructure evolution, and wear performance of selective laser melting processed commercially pure titanium. *Acta Mater* 2012;60:3849–3860.
- [177] Milewski JO, Lewis GK, Wittig JE. Microstructural evaluation of low and high duty cycle Nd:YAG laser beam welds in 2024-T3 aluminium. *Weld J* 1993;72:341S-346S.
- [178] Dunkley JJ. Atomisation. In: Davis RJ, editor. Powder metal technologies and applications. Materials Park (OH): ASM international handbook committee, ASM International; 1998. p 35-52.
- [179] Mills KC, Keene BJ, Brooks RF, Shirali A. Marangoni effects in welding. In Marangoni and interfacial phenomena in materials processing. In: Hondros ED, McLean M, Mills KC, editors. The Royal Society London: Institute of Materials, Minerals and Mining; 1998. p 97-111.
- [180] Cao X, Campbell J. Effects of precipitation of primary intermetallic compound on the mechanical properties of cast Al11.5Si0.4Mg alloy. *AFS Trans* 2000;108:391-400.
- [181] Nyahumwa C, Green NR, Campbell J. The concept of the fatigue potential of cast alloys. *J Mech Behav* 1998;9:227-235.
- [182] Cao X, Campbell J. Convection-free precipitation of primary iron-rich phase in liquid Al11.5Si0.4Mg alloy. *AFS Trans* 2001;109:501-15.
- [183] Zhao H, DebRoy T. Welding metal composition change during conduction

mode laser welding of aluminium alloy 5182. Metall Mater Trans B 2001;32B:163-172.

[184] Collur MM, Paul A, DebRoy T. Mechanism of alloying element vapourisation during laser welding. Metall Trans B 1987;18B:733-740.

[185] Ramasamy S, Albright CE. CO<sub>2</sub> and Nd:YAG laser beam welding of 6111-T4 aluminium alloy for automotive applications. J Laser Appl 2000;12:101-115.

[186] Pastor M, Zhao H, Martukanitz RP, DebRoy T. Porosity, underfill and magnesium loss during continuous wave Nd:YAG laser welding of thin plates of aluminium alloys 5182 and 5754. Weld J 1999;207S-216S.

[187] Furumoto T, Koizumi A, Alkahari MR, Anayama R, Hosokawa A, Tanaka R, et al. Permeability and Strength of a Porous Metal Structure Fabricated by Additive Manufacturing. J. Mater Process Technol 2015;219:10-16.

[188] Schaffer GB, Apelian D. Aluminium powder metallurgy: process, properties, and design solutions. Washington DC: The Aluminium Association Inc; 2000.

[189] Kalpakjian S, Schmid SR. Manufacturing Engineering and Technology. Upper Saddle River NJ: Prentice Hall; 2001.

[190] Grayson GN, Schaffer GB, Griffiths JR. On the fatigue of sintered aluminium alloys. Mater Forum 2004;28:981-85.

[191] Upadhyaya GS. Sintered metallic and ceramic materials: preparations, properties and applications. Chichester: John Wiley & Sons, Limited; 2000.

[192] Callister WD. Materials science and engineering: an introduction. New York: John Willey

& Sons, Inc; 2007.

[193] Buchbinder D, Meiners W, Wissenbach K, Müller-Lohmeier K, Brandl E. Rapid Manufacturing of Aluminum Parts for Serial Production via Selective Laser Melting (SLM). In: Hirsch J, editor. Aluminum Alloys (Vol. 2). Wiley; 2008. p. 2394-400.

[194] Mercelis P, Kruth JP. Residual stresses in selective laser sintering and selective laser melting. Rapid Prototyping J 2006;12(5):254–65.

[195] Gu DD, Meiners W. Microstructure characteristics and formation mechanisms of in situ WC cemented carbide based hard metals prepared by Selective Laser Melting. Mater Sci Eng A 2010;527:7585–92.

[196] Jain A, Basu B, Kumar BVM, Harshavardhan, Sarkar J. Grain size–wear rate relationship for titanium in liquid nitrogen environment. Acta Mater 2010;58:2313–23.

[197] Chlebus E, Kuźnicka B, Kurzynowski T, Dybała B. Microstructure and mechanical behaviour of Ti—6Al—7Nb alloy produced by selective laser melting. Mater Charact 2011;62:488–495.

[198] Boyer R, Welsch G, Collings EE. Materials properties handbook: titanium alloys. Materials Park (OH): ASM international handbook committee, ASM International; 1998. p. 3-31.

[199] Niinomi M. Mechanical biocompatibilities of titanium alloys for biomedical application. J Mech Behav Biomed Mater 2008;1:30–42.

[200] Vandenbroucke B, Kruth J-P. Selective laser melting of biocompatible metals for rapid manufacturing of medical parts. Rapid Prototyp J 2007;13:196–203.

- [201] Murr L-E, Quinones S-A, Gayatan S-M, Lopez M-I, Rodela A, Martinez E-Y, et al. Microstructure and mechanical behaviour of Ti—6Al—4V produced by rapid-layer manufacturing, for biomedical applications. *J Mech Behav Biomed Mater* 2009;2:20–32.
- [202] Spierings AB, Herres N, Levy G. Influence of the particle size distribution on surface quality and mechanical properties in AM steel parts. *Rapid Prototyp J* 2011;17(3 ): 195-202.
- [203] Spierings AB, Levy G. Comparison of density of stainless steel 316L parts produced with selective laser melting using different powder grades. In: *Proceedings of the 20th solid freeform fabrication symposium, Austin, Texas; 2009. p. 324-53.*
- [204] Kobryn PA, Semiatin SL. Mechanical properties of laser-deposited Ti-6Al-4V. *JOM*;2006:179-186
- [205] Wang Y, Bergstrom J, Burman C. Characterisation of an iron-based laser sintered material. *J Mater Process Technol* 2006;172:77-87.
- [206] Wang Y, Bergstrom J, Burman C. Four-point bending fatigue behaviour of an iron-based laser sintered material. *Inter J Fatigue* 2006;28(12):1705-15.
- [207] Bassoli E, Sewell N, Denti L, Gatto A. Investigation into the failure of inconel exhaust collector produced by laser consolidation. *Eng Fail Anal* 2013;35:397–404.
- [208] Leuders S, Thöne M, Riemer A, Niendorf T, Tröster T, Richard HA, et al. On the mechanical behaviour of titanium alloy TiAl6V4 manufactured by selective laser melting: Fatigue resistance and crack growth performance. *Inter J Fatigue* 2013;48:300–07.
- [209] Ammar HR, Samuel AM, Samuel FH. Porosity and the fatigue behaviour of hypoeutectic and hypereutectic aluminum–silicon casting alloys. *Int J Fatigue* 2008;30:1024–35.
- [210] Qian G, Hong Y, Zhou C. Investigation of high cycle and very-high-cycle fatigue

behaviours for a structural steel with smooth and notched specimens. Eng Fail Anal  
2011;17:1517–25.

## Vitae

**Dr Eyitayo Olatunde Olakanmi** completed a Ph.D at the Institute for Materials Research (IMR), University of Leeds in the UK in 2009. He was formerly a Post-Doctoral Research Fellow at the Department of Mechanical Engineering Science, University of Johannesburg, South Africa. Eyitayo Olatunde Olakanmi is the corresponding author and can be contacted at [e.o.olakanmi@gmail.com](mailto:e.o.olakanmi@gmail.com)

**Dr. Robert F. Cochrane** is a Senior Lecturer within the Institute for Materials Research (IMR), University of Leeds in the UK.

**Kenneth W. Dalgarno** is the Sir James Woodeson Professor of Manufacturing Engineering at Newcastle University in the UK.

## Figure Captions

**Fig. 1.** (A) A layered manufacturing (LM) paradigm (B) Generic fixturing [9].

**Fig. 2.** Results from (A) porosity and (B) Charpy impact measurements performed over manufactured samples. Each point represents the average % porosity or impact energy determined for six samples fabricated in five particular iterations. Red bars indicate standard deviation from the average values of porosity and impact energy. The dashed line represents an average porosity or impact energy obtained from these five values [22].

**Fig. 3.** The microstructural development in *indirect* SLS of aluminium alloys. (A) green part (nylon binder in black, not visible); (B) aluminium nitride skeleton surrounding the aluminium grains; (C) infiltrated part [53].

**Fig. 4.** Variants of *binary* liquid phase SLS or *direct* SLS (A) coated grains, (B) composites grains, and (C) separate grains [54].

**Fig. 5.** LPS of WC-Co powder mixture; (A) before infiltration (grey portion: non-molten WC particle, white portion: molten Co, dark portion: porosity); (B) after infiltration with low melting point material (copper) [55].

**Fig. 6.** Phase diagram of an ideal system for LPS [60].

**Fig 7.** A schematic diagram contrasting the effects of solubility on densification or swelling during LPS [60].

**Fig. 8.** Typical microstructure of a LPS system with the phase diagram characteristics shown in Fig. 6 [60].

**Fig. 9.** Optical images of the polished sections of the laser sintered multi-component Cu-based metal powder with varying contents (wt%) of binder CuSn in the samples (a) 20 (b) 35 (c) 50 and (d) 65 [63].

**Fig. 10.** Processing window for single layer parts made in (A) air atomised pure aluminium (AL-1) (B) gas atomised pure aluminium (AL-2) (C) water atomised Al-5.6Mg (AL-3) (D) water atomised Al- 6Mg (AL-4) and (E) gas atomised Al-12Si AL-5 powders (AL-5) (Note: Reciprocals of slopes f-a, f-b, and f-c, were computed and multiplied by the reciprocal of scan spacing (0.1 mm) in order to obtain the applied energy density). Processing conditions are laser powers (20-240W), scan rates (20-250mms<sup>-1</sup>), and scan spacing 0.1mm [40].

**Fig. 11.** Relationship between the various regions of processing map and the surface morphology of SLS/SLM processed aluminium powder at a laser power of 150 W, scan spacing of 0.1 mm, and varying scanning rates [40].

**Fig. 12.** Apparent, Tapping, and Bed densities of the aluminium powders [40].

**Fig. 13.** SLM processing windows for the SLM parts fabricated from (A) Al/5wt.% Fe<sub>2</sub>O<sub>3</sub>, (B) Al/10wt.% Fe<sub>2</sub>O<sub>3</sub> and (C) Al/15wt.% Fe<sub>2</sub>O<sub>3</sub> powder mixture [33].

**Fig. 14.** Effect of SLS processing conditions on the density of an in-situ multi-component reinforced aluminum based metal matrix composite: (A) Main plots for density and (B) Main plots for porosity [43].

**Fig. 15.** (A) Variation of the density of SLS processed AlSi12 powder with scan spacing at fixed laser power (240 W); (B) Variation of the density of SLS processed AlSi12 powder with scanning rates at different laser powers. and layer thickness (0.25 mm); and (C) Variation of the

density of SLS processed AlSi12 powder with layer thickness at fixed laser power (240 W), scanning rate (120 mm/s); scan spacing (0.1 mm) [28].

**Fig. 16:** (A) Procedure for a target dependent database. (B) Correlation and prioritisation matrix [90]

**Fig. 17.** A schematic illustration of Marangoni flow as applied to the direct SLS of W-Cu 2-phase direct SLS [93].

**Fig 18.** Variation of the density of SLS processed AlSi12 powder with the applied energy density. Processing conditions: laser power (100–200 W), scan rate (80–200mm/s), scan spacing 0.1–0.3mm, and layer thickness 0.25–1.00mm [28].

**Fig. 19.** Effect of variation in layer thickness on the microstructure of laser sintered AlSi12 powder at laser power of 200 W, scan rates of 120 mm/s; and scan spacing of 0.1mm: (A) 1.0mm, (B) 0.5mm and (C) 0.25mm [28].

**Fig. 20.** Fractional density vs. the specific energy input ( $\psi$ ) for sintered iron using different processing parameters [94].

**Fig. 21.** SEM image of SLS/SLM processed iron powder at the excessive delivery of specific laser energy input of  $0.8 \text{ kJ/mm}^3$  showing the occurrence of layer delamination as a result of increased life time of the generated liquid phase [94].

**Fig. 22.** SLS/SLM scanning strategies (a) Standard (b) Diagonal and (c) Perimeter [56].

**Fig. 23.** Four different scanning strategies adopted in the direct laser sintering of tool steels using a Nd: YAG laser machine. The numbers indicate the scanning sequence while the arrows represent the scanning directions [98].

**Fig. 24.** Three types of overlapping regime under inter-layer stagger scanning strategy. (A) Intra-layer overlapping regime. (B) Inter-layer overlapping regime. (C) Mixed overlapping regime [101].

**Fig. 25.** (A) Porosity evolution in AlSi10Mg samples processed using different combinations of scan speeds and scan strategies, (B) Influence of scanning strategy on relative density [102].

**Fig. 26.** Relative density of the SLM-produced Al–12Si samples in various atmospheres as a function of incident laser energy [38].

**Fig. 27.** The effect of the sintering gas on sintered density for Al–3.8Cu–1Mg–0.7Si (wt%) samples were sintered for 1 h and air cooled [106].

**Fig. 28.** The variation of (A) fractional density with specific energy input ( $\psi$ ) for iron powders of varying particle sizes; (B) saturation density with the mean particle sizes of iron powders [117].

**Fig. 29.** The variation of (A) the densification (D) with the specific energy input ( $\psi$ ) for iron powders of different particle sizes; (B) the densification co-efficient (K) with the mean particle size of iron powders at different oxygen concentrations [117].

**Fig. 30.** Comparison of the apparent, tapping, and sintered densities (laser power of 200W, scan speed of 65 mm/s, layer thickness of 0.25 mm, and a scan spacing of 0.1 mm) of bimodal with trimodal powders [29].

**Fig. 31.** The variation of the densification (D) with the specific energy input ( $\psi$ ) for iron-based powders of varying chemical composition under the same processing conditions [119].

**Fig. 32.** Density and relative density of the SLM parts. The density was measured by dimensional method while relative density was achieved according to CT scanning experiments [31].

**Fig. 33.** (A) Effect of the main SLM parameters (laser scanning speed, hatch distance) on the resulting relative density of AlSi12 at 100 W [27]. (B) Relationship between Relative density in % and volumetric energy density in  $\text{J mm}^{-3}$  for AW-2618 processed with LBM machine system, Realizer SLM 50 [35].

**Fig. 34.** Three-phase equilibrium for wetting and non-wetting systems [46].

**Fig. 35.** (A) Illustration showing the epitaxial nucleation and competitive growth in the weld fusion zone [141], (B) Schematic of free energy change associated with heterogeneous nucleation in casting and welding juxtaposed with free energy change in homogeneous nucleation [143].

**Fig. 36.** (A) Microstructure of SLM processed Ti-6Al-4V exhibiting porosity and insufficient substrate remelts and (B) Etched microstructure of fully dense Ti-6Al-4V specimen [46].

**Fig. 37.** Optical micrographs of etched, polished sections parallel to the build directions at different energy density: (A)  $100 \text{ J/mm}^3$  (B)  $75 \text{ J/mm}^3$  (C)  $67 \text{ J/mm}^3$  (D)  $40 \text{ J/mm}^3$  (E)  $13 \text{ J/mm}^3$  [28].

**Fig. 38.** Relationship between the energy density and the average dendritic arm spacing of the SLS processed AlSi12 powders across the depth of the laser sintered AlSi12 samples [28].

**Fig. 39.** Effect of energy density on the fraction of primary phase in SLS processed AlSi12 powder [28].

**Fig. 40.** Characteristic microstructures of SLS processed AlSi12 powder with varying processing conditions: (A, B) 100 J/mm<sup>3</sup>; (C, D) 67 J/mm<sup>3</sup>; (E, F) 50 J/mm<sup>3</sup> [28].

**Fig. 41.** Sections through the micrograph of AlSi12 (200W-120mm/s) generated by 67 J/mm<sup>3</sup> [28].

**Fig. 42.** Optical micrographs showing the variation of microstructure of Ti-48Al-2Mn-2Nb (wt.%) alloy consisting of lamellar ( $\alpha_2 + \gamma$ ), featureless ( $\gamma$ ) and partially lamellar [ $\gamma + (\alpha_2 + \gamma)$ ] and fabricated with laser power (A) 300W, (B) 360W, (C) 400W. (Scanning speed 8mm/s; powder feed rate 3g/min; z-increment 0.2mm; number of layers 20) [150].

**Fig. 43.** Typical microstructure of SLM processed AlSi10Mg parts at powder bed temperature of 300 °C, and build orientation of 0°: (A) As built (B) Peak-hardened [30].

**Fig. 44.** Micrographs of aluminium alloy 2xxx on Al 6082 substrate after SLM processing (B) Optical micrograph of formation of single track; (B) SEM micrograph of microstructure of melted middle zone [153].

**Fig. 45:** (A) Diagram of basic SLM experimental platform with dual-magnetic-pole AC electromagnet (SD: scanning direction of laser; MD: movement direction of electromagnet). (B) optical metallographic images for Ti-6Al-4V SLM part. (C) Variations of electromagnetic flux density with the average grain size [154].

**Fig. 46.** SEM images of laser sintered high speed steel powders using laser power of 50 W and a scan rate of 5.0 mm/s and a scan line spacing of 0.15 mm. Particle sizes were: (A) as supplied from atomiser (full range), (B) 53  $\mu\text{m}$  – 150  $\mu\text{m}$ , (C) >150  $\mu\text{m}$  and (D) <38  $\mu\text{m}$  [5].

**Fig. 47.** Polished section of laser sintered parts shows the effect of graphite addition on the pore structures on a section cut parallel to the building direction; laser power is 215 W, scan rate is 75 mm/s, scan line spacing is 0.3 mm, and layer thickness is 0.1 mm (A) 0% C (B) 0.4% C (C) 0.8% C (D) 1.2% C [156].

**Fig. 48.** Characteristic microstructure of laser sintered iron-1.2 wt.% graphite powder mixture on a section cut parallel to the building direction shows heterogeneous carbon dissolution in the iron matrix resulting in the varying local hardness values (Table 2.4). Laser power is 215 W, scan rate is 75 mm/s, scan line spacing is 0.3 mm, and layer thickness is 0.1 mm [156].

**Fig. 49.** AFM results presenting ultrafine/nanoscale particles in the cross section of the SLM parts made from (A) Al/15wt%Fe<sub>2</sub>O<sub>3</sub>, (B) AlMg1SiCu/15wt%Fe<sub>2</sub>O<sub>3</sub>, and (C) AlSi10Mg/15wt%Fe<sub>2</sub>O<sub>3</sub> [31].

**Fig. 50.** SEM secondary electron image taken from the two opposing fracture surface of sand cast Al-Si11.5-Mg0.4 showing an extensive double oxide film [180].

**Fig. 51.** (A) Marangoni convection in the melt pool. (B) Oxide disruption and solidification of the melt pool [27].

**Fig. 52.** Impact energy as a function of the oxide inclusion content in a hot-repressed 4340 steel, showing the detrimental effect of a small level contamination [113].

**Fig. 53.** The pores (dark spots) in these two sintered steels vary in shape and size, largely due to differences in sintering cycles. The arrangement of pores outlining the particles in (A) is detrimental to final properties, while the smooth pore structure evident in (B) is more desirable [113].

**Fig. 54.** Hardness of SLM processed AlSi10Mg samples depending on (A) scan rate (B) scan spacing [24].

**Fig. 55.** SEM images showing characteristic morphologies of worn surfaces of SLM-processed Ti parts at: (A)  $900 \text{ J m}^{-1}$ ,  $100 \text{ mm s}^{-1}$ ; (B)  $450 \text{ J m}^{-1}$ ,  $\text{mm s}^{-1}$ ; (C)  $300 \text{ J m}^{-1}$ ,  $300 \text{ mm s}^{-1}$ ; (D)  $225 \text{ J m}^{-1}$ ,  $400 \text{ mm s}^{-1}$  [176].

**Fig. 56.** Ultimate tensile strength of SLS-processed bronze-nickel parts as a function of scan speed and laser power [50].

**Fig. 57.** Tensile strength depending on build up direction for SLM processed AlSi10Mg part [24].

**Fig. 58.** Ultimate tensile strength  $R_m$  and yield strength at 0.2 per cent offset  $R_{p0.2}$  for  $0^\circ$ ,  $45^\circ$  and  $90^\circ$  orientations for finer powder type 1 and coarsest powder type 3 [202].

**Fig. 59.** Pore sizes of test cubes for finer powder type 1 (left) and coarse powder type 3 (right) for 30mm layers in  $0^\circ$  orientation [202].

**Fig. 60.** Elongation at fracture  $A_t$  for finest powder type 1, fine powder type 2, and coarse powder type 3 [202].

**Fig. 61.** Typical fracture surfaces of SLM processed AlSi10Mg parts (powder bed temperature of 300 °C / build direction of 0° / as-built): (A) crack initiation site and (B) area of forced fracture. [30].

**Fig. 62.** Typical fracture surfaces of SLM processed AlSi10Mg parts (powder bed temperature of 300 °C / build direction of 0° / peak hardened): (A) crack initiation site and (B) area of forced fracture [30].

### **Table Captions**

**Table 1:** Properties of pure and alloyed aluminium at its melting point [44]

**Table 2:** SLS/SLM process parameters and material variables influencing the processing and densification mechanism of fabricated parts [50].

**Table 3:** Solubility effects on densification in LPS [60].

**Table 4:** Fractional amount of liquid phase generated in various SLS processed metal systems.

**Table 5:** Elemental Composition of the Powdered Samples by Semi-quantitative EDS Analysis (weight %) [40].

**Table 6:** Summary of application of SLS/SLM to metal systems.

**Table 7:** Commercial Machines and Lasers for SLS/SLM of Metal Powders [128].

**Table 8:** Comparison of absorptance of single-component and two-component metallic powders using Nd:YAG and CO<sub>2</sub> lasers [126].

**Table 9:** The local carbon concentration measured by X-ray photoelectron spectroscopy (XPS) method and microhardness values of marked areas in Fig. 48 [156].

**Table 10:** Comparative analysis of parts fabricated by SLS/SLM and other traditional production processes [188, 189].